Plasticity Modelling of Post consumer recycled Polypropylene and Polyethylene

TU Delft

PLASTICITY MODELLING OF POST CONSUMER RECYCLED POLYPROPYLENE AND POLYEHTYLENE

by

Manoj Reddy Gongati

to obtain the degree of Master of Science
at the Delft University of Technology,
to be defended publicly on Wednesday, August 24th, 2022 at 3:00 PM.

Student number:	5131995	
Project duration:	April 2021 – August 2022	
Thesis committee:	Dr. Miguel A. Bessa,	TU Delft, Associate Professor & supervisor
	Prof. dr. ir. Jilt Sietsma,	TU Delft, Professor
	Dr. I. B. C. M. Rocha,	TU Delft, Assistant Professor
	Jiaxiang Yi,	TU Delft, PhD candidate & daily supervisor

SUMMARY

The two most common Post Consumer Recycled (PCR) plastics, isotactic polypropylene (iPP) and high density polyethylene (HDPE), differ in composition and mechanical behavior when compared to their virgin counterparts. This thesis focuses on understanding and modeling the mechanical performance of these two PCR plastics separately. Within this context, the present work implements three finite strain thermo-elasto-viscoplastic constitutive models developed by Johnsen et al. [1], Mirkhalaf et al. [2] and Anand et al. [3] proposed in the literature to predict the behavior of PCR-iPP and PCR-HDPE. The models are compared and further developed to take into account the effects of recycling. All the models depend on the fully implicit return mapping algorithm and associated state update procedures.

Given the complexity of the models, this thesis proposes the use of Bayesian optimization to facilitate the material parameter calibration when provided with the experimental data. A two-step procedure is proposed where first the models are calibrated for yielding, and then for post yielding behavior (strain softening and orientational hardening).

The models are assessed considering different experimental tests, including standardized specimens with different radius of curvature. A simple modification is suggested to capture the strain hardening response at large deformations accurately. This work concludes that the model developed by Mikhalaf et al. [2] is capable of accurately reproducing the experimental results obtained in the validation experiments of PCR-PP where as the modified Anand model is capable of accurately reproducing the experimental results of PCR-PE.

Acknowledgements

I would like to acknowledge the people who have given me their time and support over the duration of my thesis:

First and foremost I would also like to thank my advisor, Dr. Miguel Bessa for introducing me to the field of computational mechanics and giving me the opportunity to work on such an interesting topic and thank you for always being available to discuss my project and for infinite patience.

I would like to express my gratitude to: Jiaxiang Yi for helping me and the continuous support during my thesis; Bernardo Ferreira for helping me in the implementation of computational models; Dr. Dongil shin for helping me in implementing Bayesian optimization for the calibration of material properties; Satya Nanditha Raj Mudunuru and Tiancheng Guo for the useful discussions and valuable suggestions.

Contents

1

INTRODUCTION

Thermoplastics are the important engineering materials used widely in many applications over the past few decades. Some examples are dampers, food packaging, thermal insulation of pipelines, and electrical insulation of high-voltage cables. Among the thermoplastics, polyethylene (PE) and polypropylene (PP) are the two most abundantly produced plastics worldwide. More than 70 million and 50 million metric tons of PE and PP are produced annually [4]. The two plastics (PP and PE) do not mix, limiting the options for dealing with mixed waste and decreasing the value of recycled products. Eagan et al. [4] reported the synthesis of multiblock copolymers of iPP and PE by using a selective polymer initiator. The high-molecular-weight blocks could be used to reinforce the interface between iPP and PE and allow the blending of the two polymers [4]. Interfacial compatibilization of phase-separated PE and iPP tetra block copolymers enable morphological control, transforming brittle materials into mechanically tough blends. Individually, pure iPP and PE display ductility and strain hardening when pulled in tension at room temperature, as shown in figure 1.1. Blending the two components leads to a phase-separated material and a marked reduction in the strain at the breaking point.

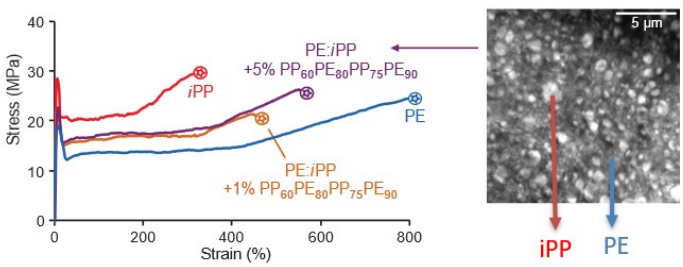

Figure 1.1: Uniaxial tensile elongation of PE/iPP materials and blends [4]

The formation of iPP/HDPE composites opens up new design spaces previously unattainable with homogeneous polymers. To create the iPP/PE blend, it is important to individually understand the bulk material's mechanical performance. The mechanical behavior of iPP and HDPE is complicated because strain rate, temperature, and stress-triaxiality have a significant impact. The stress-strain behavior of polymers is mainly highly nonlinear and related to the underlying microstructural deformation mechanisms. Hence, it is challenging to create accurate constitutive models that can predict the mechanical response of polymeric materials under different loading conditions.

The main objective of the present thesis is to implement state of the art plasticity constitutive models, assess their predictive quality when modelling the post consumer recycled polypropylene (PCR-PP) and post consumer recycled polyethylene (PCR-PE) and improve them if needed. In addition, the work also aims at facilitating the calibration of material properties for the constitutive models.

In chapter 2 the fundamental concepts of polymer science and the underlying deformation mechanisms are explained. The numerical implementation of the Johnsen model [1], Mirkhalaf Model [2] and Anand model [3] are discussed briefly. The methods to calibrate the material properties are also reviewed in chapter 2. Description of material parameter calibration procedure is discussed briefly in chapter 3. From the obtained optimized parameters, The mechanical response of PCR-PP was examined under tensile tests. In chapter 4 the simulations of PCR-PE are performed and compared with the experimental results. Conclusions regarding the outcomes and recommendations for development of the work are discussed briefly in chapter 5.

2

LITERATURE REVIEW

POLYMERS are large molecules or macromolecules composed of repeating units. They often have long chain, branched, and sometimes cross-linked. They are abundantly found in nature, mainly in plants (cellulose) and tissues (proteins) and are primarily composed of hydrocarbons with covalent carbon bonds. They are either single chains or networks. Though single chains can be branched, the polymers are diluted into coils called entanglements, and weak or Van der Waals forces exist between the chains. Polymer chains slide over one another under external force, breaking the weak bonds. An increase in the number of entanglements leads to an increase in the stiffness of the polymers. Polymer flow is strongly hindered by the entanglements leading to high viscosity. In the thermoset polymer networks, molecular chains are strongly connected by chemical cross-links. The polymer networks are formed as bridges between the single chains, as in the case of vulcanization of rubber where sulfur bridges are formed [5].

2.1. THERMOPLASTICS AND THERMOSETTING POLYMERS

2.1.1. THERMOPLASTICS

Thermoplastics are long-chained and non-cross-linked polymers that flow at elevated temperatures and harden when cooled. At high temperatures, the secondary bonds between the chains diminish, facilitating the relative motion of chains. These polymers are often manufactured by the application of pressure and temperature simultaneously. The two most common examples are shown in figure 2.1 and 2.2.

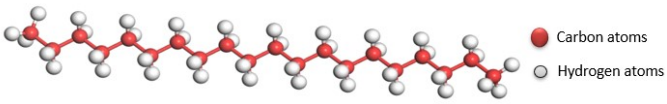

Figure 2.1: Polyethylene ($(C_2H_4)_n$)

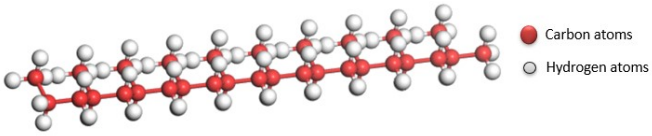

Figure 2.2: Polypropylene ($(C_3H_6)_n$)

2.1.2. THERMOSETTING POLYMERS

Thermosets are cross-linked polymers and cannot be remolded. These bonds anchor the chains together during heat treatments to resist the vibrational and rotational chain motions at high temperatures. Thus, the materials do not soften when heated. Thermoset polymers are generally stronger than thermoplastics and have better dimensional stability. One of the examples is shown in figure 2.3.

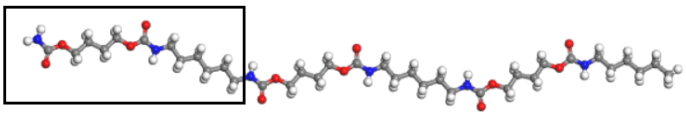

Figure 2.3: Polyurethane

2.2. PHYSICAL STRUCTURE

After determining the chemical composition of polymers, there remains the question on how molecular chains of the polymer are arranged in space. This has two different aspects.

1. Rotational Isomerism

2. Orientation and crystallinity

2.2.1. ROTATIONAL ISOMERISM

The Rotational Isomerism explains the arrangement of a single chain without considering the effect of its neighbors. The arrangement of the single chain relates to that there are possible conformations for the molecule because of the hindered rotation about single bonds in the structure. The main reason for the flexibility in the polymers is due to the torsion angles. To explain the rotational isomerism, consider the example of polyethylene with neighboring three atoms C_{i-2}, C_{i-1}, C_i.

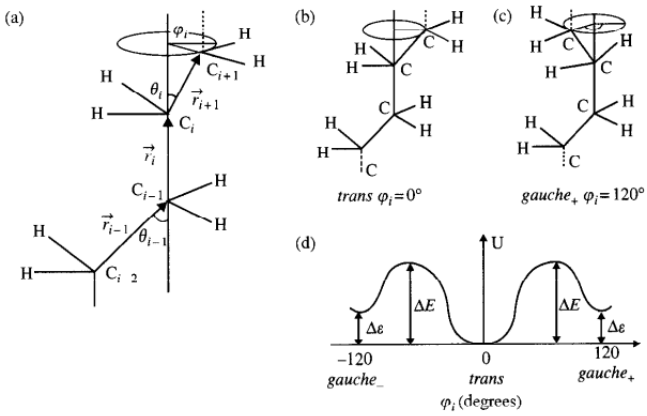

Figure 2.4: a) Torsional angle for the sequence of three bonds b)Trans state c) Gauche state d)Torsional angle dependence of energy [6]

The bond vector $\vec{r}_i$, between the atoms C_{i-1} and C_i defines the axis of rotation for the bond vector $\vec{r}_{i+1}$ at a constant bond angle θ_i. The zeroth value of the torsion angle φ_i corresponds to the bond vector $\vec{r}_{i-1}$ collinear with the bond vector $\vec{r}_{i+1}$. This refers to the trans-state of the torsion angle, which is the state of lowest energy conformation. The change of the torsional angle leads to a change of energy conformations as variations occur in the distance leading to the change in interactions between the carbon and hydrogen atoms. The secondary minima occur at the torsion angle of $\pm 120^0$. This refers to the gauche state. The energy difference between the trans and gauche state $\Delta\varepsilon$ determines the relative probability of the torsion angle in the gauche state being in the thermal equilibrium [6].

2.2.2. ORIENTATION AND CRYSTALLINITY

When cooled down from the polymer melt to become a solid, many polymers form a disordered structure called an amorphous state. The amorphous state is considered the random entanglement of polymers. Amorphous polymers have high stiffness and yield strength at room temperature. Polymethyl methacrylate (PMMA), Polystyrene, and quenched polyethylene terephthalate (PET) are examples of amorphous polymers. If the amorphous polymers are stretched, the chains preferentially align along the direction of the applied load, reducing the system's entropy. The molecular orientations due to stretching can lead to the small region of three-dimensional order called crystallites. The simple explanation of this behavior is that the orientation process has brought the polymer chains into adequate juxtaposition to create the three-dimensional order. Many polymers crystallize if they are cooled slowly from the melt. The degree of crystallinity may vary from the completely amorphous state to 95%. Contrary to metals, which are completely crystalline, and ceramics which are either wholly crystalline or amorphous, polymers exist as semi-crystalline. Though they are not homogeneous in the microscopic sense and often show spherulitic structure, such specimens are unoriented from

the macroscopic point of view, possessing isotropic material properties [7].

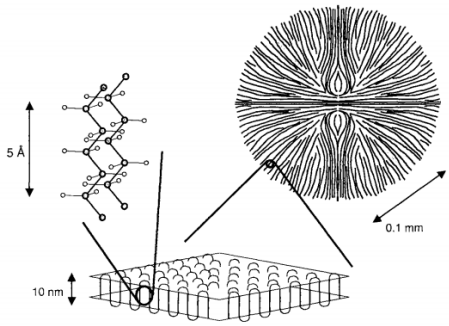

Figure 2.5: Ordered structure [8]

2.3. TENSILE STRESS-STRAIN CURVES

The mechanical properties of polymers are generally analyzed using standardized tests such as uniaxial tensile and compressive tests. These tests allow us to determine several mechanical properties of polymers to characterize the elastic, plastic, and damage behavior. Three generally observed tensile test curves [9] are shown in figure 2.6.

2.3.1. THERMOSET POLYMER

Thermosetting polymers are generally brittle due to cross-linking (interchain covalent bonds). The tensile response is mostly linear elastic and negligible plastic deformation, as cross-linking restricts the chain sliding. Thermoset polymers have high stiffness and yield strength.

2.3.2. THERMOPLASTICS

Thermoplastic polymers tensile curves are analogous to the tensile stress-strain curves of metals. Thermoplastics undergo elastic deformation followed by plastic deformation and geometrical softening.

2.3.3. ELASTOMERS

An elastomeric polymer stress-strain behaviour is totally elastic, generally exhibiting very low tensile modulus (low stiffness) and high elongation up to fracture.

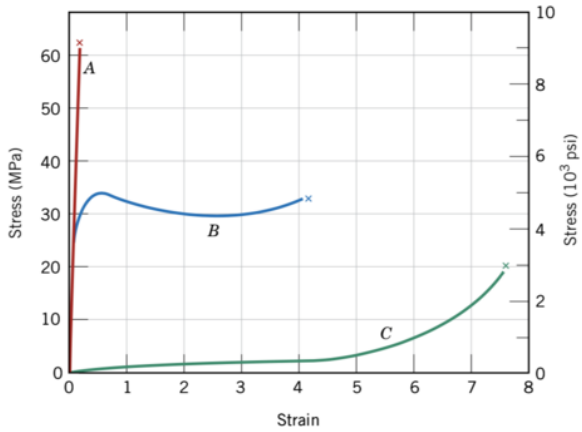

Figure 2.6: Stress-Strain behaviour of polymers: A) Thermoset B) Thermoplastic C) Elastomers [9]

2.4. MECHANICAL BEHAVIOUR OF THERMOPLASTICS

The stress-strain curve of the thermoplastics clearly exhibits three regions.1) elastic region 2) strain softening 3) strain hardening

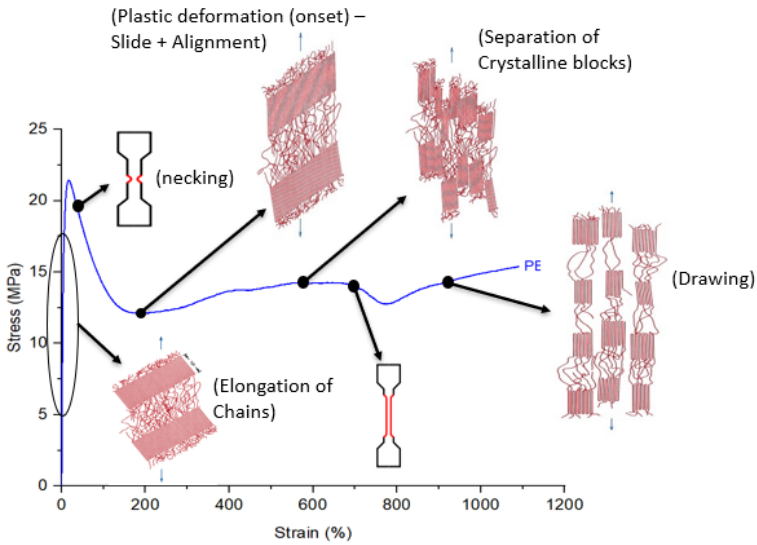

Figure 2.7: Stress-Strain behaviour of polymers [9]

The mechanisms of elastic, strain softening, and strain hardening of semi-crystalline polymers are clearly shown in the figure 2.7 when the material is subjected to tensile loading. The onset and the first stage of elastic deformation results in the elongation of molecular chains present in the amorphous regions between adjacent spherulitic platelets in the direction of the applied load. The nonlinear elastic response is controlled by intermolecular interactions combined with entropic contribution. Later the elastic deformation results in a slight increase in the thickness of the crystalline platelets due to the stretching of chain covalent bonds.

It is often the case that the macroscopic sample under tension displays a shape transformation just after yielding, known as strain softening (necking). Thereby, it becomes visibly thinner at some point along its length. The consequence is that once necking occurs in one location, the size of that region tends to grow while the original neck thickness is more or less preserved. During this region, the engineering stress is roughly constant. Eventually, this encompasses the entire specimen, and further extension leads to a more uniform deformation along with the sample, accompanied by strain hardening. The intrinsic softening, observed during plastic flow in polymers, is closely related to physical aging and rejuvenation. The key microstrctural feature controlling strain softening or the yield peak is the change in free volume or deformation induced disordering of polymers. The lower the free volume, the higher the yield peak. Annealed specimens have lower free volume than quenched specimens, so annealed specimens show large stress drop after yielding [10].

The onset of plastic deformation occurs when adjacent chains in crystalline platelets slide past one another, which is resisted by relatively weak van der Waals bonds and leads to tilting the platelets in the loading direction. As deformation continues, crystalline block segments separate from the platelet while keeping attached by tying molecular chains, which become highly aligned with the tensile direction. For further deformation, the spherulitic structure is virtually destroyed. Because in crystalline regions, the molecular chains are closely packed in an ordered and parallel arrangement, significant intermolecular forces result from forming large numbers of van der Waals interchain bonds. Although such forces are much weaker than the primary covalent ones, it is nonetheless comprehensible that the tensile modulus increases significantly with the degree of crystallinity. Moreover, the strength is generally enhanced, and the polymers tend to become more brittle as they stiffen. The material strength, i.e., the resistance to plastic deformation, increases due to contributions that restrain molecular chains from stretching and sliding between platelets and adjacent chains. Such restrain mainly depends on the degree of chain entanglements and intermolecular bonding. It has also been observed that tensile strength increases with molecular weight due to a corresponding increase in chain entanglements. Based on the previous mechanisms, some standard techniques are used to improve the mechanical properties of semi-crystalline polymers.

One of the most necessary stiffening and strengthening techniques is termed drawing. It improves the tensile modulus and mechanical strength by permanently deforming the polymer in tension until its structure becomes highly aligned, as described for the last stage of plastic deformation. The degree of stiffening and strengthening depends on the extent of deformation, and the properties of the resulting drawn polymers are highly

anisotropic. When applied to undraw polymers, heat-treating or annealing of semi-crystalline polymers can lead to an increase in the degree of crystallinity, and a consequent increase in tensile modulus and yield strength and decrease of ductility [11].

2.4.1. YIELDING THEORIES

The simple definition of yield stress is the minimum stress required at which the material undergoes permanent deformation. This definition is satisfactory for metals, where a clear difference can be made between the elastic and plastic deformations, but it is not straightforward in polymers. In many cases, such as the tensile tests, yield coincides with observing a maximum load in the load–elongation curve. The yield stress can be defined as the true stress at the maximum observed load. Because this stress is achieved at a comparatively low elongation of the sample, it is often adequate to use the engineering definition of yield stress as the maximum observed load divided by the initial cross-sectional area. In some cases, there is no observed load drop, and another definition of yield stress is required. One approach is determining the stress where the two tangents to the initial and final parts of the load–elongation curve intersect. An alternative is to define an initial linear slope on the stress-strain curve and then draw a line parallel to this, offset by a specified strain, say 15% [12]. The intersection of this line with the stress-strain curve then defines the offset or proof stress, which is the yield stress. Yielding can be produced by a wide range of stress states, not just simple tension. In general, it must therefore be assumed that the yield condition depends on a function of the three-dimensional stress field. The components of the stresses are σ_{11}, σ_{22}, σ_{33}, σ_{12}, σ_{13} and σ_{23}. It is often convenient to use the principal stresses. The generally used yield criteria are discussed below [12].

$$f(\sigma_I, \sigma_{II}, \sigma_{III}) = \text{constant} \tag{2.1}$$

The yield criterion established indicates that plastic flow may occur when the uniaxial stress attains a critical value. This principle could be expressed by means of a yield function that is negative when only elastic deformations are possible and reaches zero when the plastic flow is imminent.

$$\Phi(\sigma, A) = |\sigma| - \sigma_y \leq 0 \tag{2.2}$$

where Φ is the scalar yield function. The yield locus, means the set of stresses for which plastic yielding may occur, is the boundary of the elastic domain, where $\Phi(\sigma, A) = 0$.

TRESCA YIELD CRITERIA

The earliest yield criterion to be suggested for metals was Tresca's criteria that yield occurs when the maximum shear stress reaches a critical value

$$\frac{1}{2}(\sigma_I - \sigma_{III}) = \frac{Y}{2} \tag{2.3}$$

where $\sigma_I > \sigma_{II} > \sigma_{III}$.

VON MISES YIELD CRITERIA

The Von Mises yield criterion assumes that the yield behaviour is independent of hydrostatic pressure and that the yield stresses in simple tension and compression are equal.

It is expressed most simply in terms of the principal components

$$\frac{1}{2}((\sigma_I - \sigma_{II})^2 + (\sigma_I - \sigma_{II})^2 + (\sigma_I - \sigma_{II})^2) = Y^2 \tag{2.4}$$

Since the yield behaviour of polymers is temperature and strain rate dependent, phenomenological models such as Eyring's theory of polymers, which provide the information of the yield behaviour at molecular level. The approach is temperature and strain rate sensitive and also considers the molecular reorientation associated with plastic deformation.

EYRING'S THEORY

Molecular approaches exist to gain a molecular understanding of the polymer's viscosity based on the thermally activated rate process theory. In the random thermal motion of polymer chains, any energy will vary with time, occasionally it may be sufficient for the chain to reach the activated state. This process is known as thermal activation. According to kinetic theory, the probability of the chain reaching the activated state is given by $e^{-(\Delta G/kT)}$ where k is Boltzmann's constant and ΔG is known as the activation free energy barrier. The rate at which the transformation occurs will depend on the frequency with which atoms reach the activated state [13].

$$\nu = \nu_0 e^{-\frac{\Delta H}{RT}} \tag{2.5}$$

where ΔH is the activation energy and ν_0 considers both the fundamental vibration frequency and entropy contribution to the Gibbs free energy. The basic molecular process can be either intermolecular or intramolecular. Considering the case when no stress is applied, there exists a dynamic equilibrium. When the stress is applied the chain segments moves with a frequency ν over the potential barrier in each direction where it is assumed that the applied stress σ produces the linear shifts of the energy barriers by σV, where V is the activation volume. The frequency in the flow direction is

$$\nu_1 = \nu_0 \exp\left[-\frac{(\Delta H - \sigma V)}{RT}\right] \tag{2.6}$$

The frequency of flow in the backward direction is

$$\nu_2 = \nu_0 \exp\left[-\frac{(\Delta H + \sigma V)}{RT}\right] \tag{2.7}$$

The net flow is

$$\nu = \nu_1 - \nu_2 = \nu_0 e^{-\frac{\Delta H}{RT}} \left[e^{\frac{\sigma V}{RT}} - e^{-\frac{\sigma V}{RT}}\right] \tag{2.8}$$

If we assume that the net flow in the forward direction is related to the strain rate ($\dot{\epsilon}$), then

$$\dot{e} = \dot{e}_0 e^{-\frac{\Delta H}{RT}} \sinh\left[\frac{\sigma V}{RT}\right] \tag{2.9}$$

Therefore the shear yield stress in terms of strain rate is written as

$$\sigma = \frac{K_B T}{V} \operatorname{arcsinh}\left(\frac{\dot{e}}{\dot{e}_0} \exp\left[\frac{\Delta H}{RT}\right]\right) \tag{2.10}$$

2.5. RECYCLABILITY

The growth in plastic production and replacement of other materials in many industry sectors is leading to an increasing amount of plastic waste. Traditionally, many polymers were disposed of in landfill sites, but the negative environmental impact has motivated more environmentally friendly options like recycling [14]. There are four main approaches to plastics recycling: primary, secondary, tertiary, and quaternary. Primary recycling focuses on clean, uncontaminated, single-type scrap from processing operations. Secondary recycling aims at the management of mixtures of plastic wastes. Tertiary or chemical recycling has been defined as the cleavage of polymer chains to make chemical products of lower molecular weight distribution or even to recover the original monomer, which can be used for another complete cycle of polymerization. Finally, quaternary recycling comprises the utilization of plastic wastes as energy sources [15].

Understanding the effect recycling has on properties, or the conditions under which no degradation occurs can enable a larger percentage of plastics to be recycled. For example, Aurrekoetxea et al. [15] showed that blends of recycled and virgin PP could demonstrate higher strength and stiffness after multiple recycling cycles at the expense of elongation at fracture and fracture toughness. This is partially due to the increasingly crystalline structure of the recycled polymers. Polymer flexibility depends on its segments' ability to rotate. Crystalline structures hinder such rotations. Therefore, a crystalline material is significantly stiffer than the equivalent plastic in its amorphous condition. Costa et al. [16] showed that the rheological and physical properties of iPP were degraded after reprocessing. In addition, they observed an increase in the melt flow index (MFI) and the crystallinity rate, with a continuous reduction of the molar weight and the melting temperature (T_m) when the number of extrusion runs augments.

The true stress-strain curves for pure and talc-filled polypropylene and their recycled derivatives are shown in figure 2.9. Both materials exhibit a classical mechanical behavior under tensile loading after a linear elastic response, a small visco-elastic response appears before the yielding point. After the yield point, softening is observed, followed by strain hardening. It can be observed that the recycling process decreases the yield stress for both materials. However, it is seen that the failure stress and strain are quite affected by several cycles. It seems that this property decreases linearly with recycling [17].

2.6. GENERAL ELASTOPLASTIC MODEL

The general Elastoplastic constitutive model consists of the following components [18].

1. The Elastic and plastic strain decomposition
2. Elastic law
3. Yield criteria
4. Plastic flow rule to calculate the plastic strain
5. Hardening law

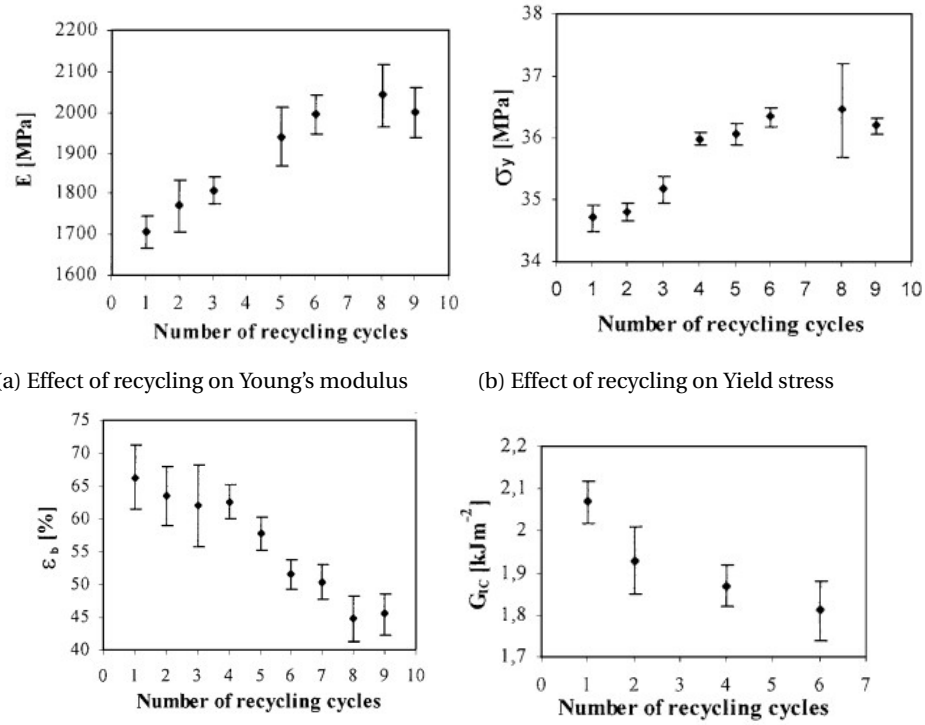

(a) Effect of recycling on Young's modulus

(b) Effect of recycling on Yield stress

(c) Effect of recycling on failure strain

(d) Effect of recycling on fracture toughness

Figure 2.8: The effect of recycling on key material parameters over a range of cycles [15]

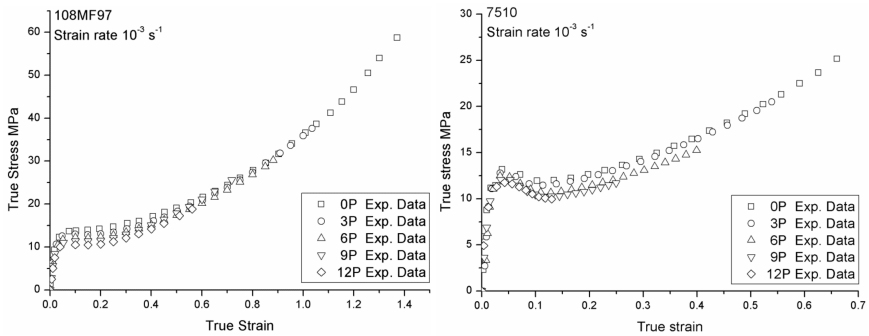

(a)

(b)

Figure 2.9: True stress-true strain curves for (a) pure (b) talc-filled polypropylene and recycled derivatives [17].

2.6.1. ADDITIVE DECOMPOSITION OF STRAIN

The additive decomposition of strain is generally obtained by splitting the total strain into the elastic and plastic components.

$$\varepsilon = \varepsilon^e + \varepsilon^p \tag{2.11}$$

The strain is calculated as the logarithm of stretch tensor (U)

$$\varepsilon = \ln(U) \tag{2.12}$$

The decomposition of strain rates

$$\dot{\varepsilon} = \dot{\varepsilon}^e + \dot{\varepsilon}^p \tag{2.13}$$

MULTIPLICATIVE SPLIT OF DEFORMATION GRADIENT TENSOR

The main assumption of the large strain constitutive models is the hypothesis that the deformation gradient tensor F can be multiplicatively split into elastic and plastic deformation gradient tensors.

$$F = \frac{\partial x^3}{\partial x^1} = \frac{\partial x^3}{\partial x^2}\frac{\partial x^2}{\partial x^1} \tag{2.14}$$

$$F^e = \frac{\partial x^3}{\partial x^2}, F^p = \frac{\partial x^2}{\partial x^1} \tag{2.15}$$

$$F = F^e F^p \tag{2.16}$$

The finite deformation plasticity models considers the both the contributions of the

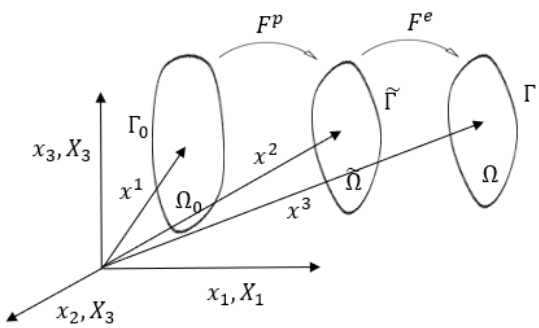

Figure 2.10: Multiplicative Split of Deformation tensor

intermolecular(part A) describing the hyperelastic and viscoplastic behaviour and orientational hardening due to the polymer network alignment. The deformation gradient tensor is equal in both the parts.

$$F = F_A = F^e F^p \tag{2.17}$$

ELASTIC AND PLASTIC POLAR DECOMPOSITION

Both the elastic and plastic gradient tensors are again can be decomposed as

$$F^e = R^e U^e = V^e R^e \tag{2.18}$$

$$F^p = R^p U^p = V^p R^p \tag{2.19}$$

where R^e is the elastic rotation tensor, U^e is the right elastic stretch tensor, V^e is the left elastic stretch tensor, R^p is the plastic rotation tensor, U^p is the right plastic stretch tensor and V^p is the left plastic stretch tensor.

DECOMPOSITION OF VELOCITY GRADIENT

The velocity gradient L can also be decomposed as

$$L = \frac{\partial v}{\partial \chi} = \dot{F} F^{-1} \tag{2.20}$$

$$L = [\dot{F}^e_A F^p_A + F^e_A \dot{F}^p_A](F^p_A)^{-1}(F^e_A)^{-1} \tag{2.21}$$

$$L_A = \dot{F}^e_A (F^e_A)^{-1} + F^e_A \dot{F}^p_A F^{-1}_A = L^e_A + L^p_A \tag{2.22}$$

where

$$L^e_A = \dot{F}^e_A (F^e_A)^{-1}, L^p_A = F^e_A \dot{F}^p_A F^{-1}_A \tag{2.23}$$

L^e_A is the elastic velocity gradient and L^p_A is the plastic velocity gradient.

2.6.2. ELASTIC LAW

The dissipative models are generally developed in the framework of thermodynamics. It is assumed that the free energy is function of total strain, plastic strain and internal variables related to the hardening. The free energy can be split as

$$\psi(\varepsilon, \varepsilon^p, \alpha) = \psi(\varepsilon^e) + \psi(\alpha) \tag{2.24}$$

$$\psi(\varepsilon, \varepsilon^p, \alpha) = \psi(\varepsilon - \varepsilon^p) + \psi(\alpha) \tag{2.25}$$

The generalized elastic law is in the form of

$$\sigma^e = \rho \frac{\partial \psi(\varepsilon^e)}{\partial \varepsilon^e} \tag{2.26}$$

Assuming the elastic behaviour is isotropic and linear, the free energy can be defined as

$$\rho\psi(\varepsilon^e) = \frac{1}{2}\varepsilon^e : D^e : \varepsilon^e \tag{2.27}$$

$$\rho\psi(\varepsilon^e) = G\varepsilon^e_d : \varepsilon^e_d + \frac{1}{2}K(\varepsilon^e_v)^2 \tag{2.28}$$

where G and K are shear modulus and bulk modulus respectively. The ε^e_d represents deviotoric component of elastic tensor and ε^e_v represents the volumetric strain. Thus the elastic law is

$$\sigma^e = D^e : \varepsilon^e \tag{2.29}$$

$$\sigma^e = 2G\varepsilon^e_d + K\varepsilon^e_v I \tag{2.30}$$

2.6.3. YIELD CRITERIA

The yield criterion established indicates that plastic flow may occur when the uniaxial stress attains a critical value. This principle could be expressed by means of a yield function which is negative when only elastic deformations are possible and reaches zero when plastic flow is imminent.

$$\Phi(\sigma, A) = |\sigma| - \sigma_y \leq 0 \tag{2.31}$$

where Φ is the scalar yield function. The yield locus, means the set of stresses for which plastic yielding may occur, is the boundary of the elastic domain, where $\Phi(\sigma, A) = 0$.

2.6.4. PLASTIC FLOW RULE

To characterize the plasticity of the material, the plastic strain needs to be calculated. The plastic strain is generally computed using the plastic flow rule. It is defined as follows.

$$\dot{\varepsilon}^p = \dot{\gamma} N \tag{2.32}$$

where γ is the plastic multiplier and N is termed as the flow vector and defined as

$$N = \frac{\partial \Psi}{\partial \sigma} \tag{2.33}$$

where Ψ is the plastic potential. For the case when $\Psi = \Phi$, then it is called as the associative flow rule.

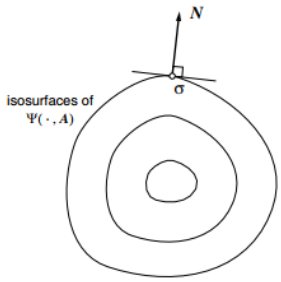

Figure 2.11: Flow vector [19]

2.6.5. HARDENING LAW

The hardening law is defined as

$$H(\sigma, A) = -\frac{\partial \Psi}{\partial A} \tag{2.34}$$

where H is the hardening modulus and A is the set of hardening thermodyamical forces.

ISOTROPIC HARDENING

A plasticity model is said to have isotropic hardening if the evolution of the yield surface is such that, at any state of hardening, it corresponds to a uniform (isotropic) expansion

of the initial yield surface, without translation as shown in figure 2.12. For a multiaxial plasticity model with a von Mises yield surface, isotropic hardening corresponds to the increase in radius of the von Mises cylinder in principal stress space. In the constitutive description of isotropic hardening, the set α normally contains a single scalar variable, which determines the size of the yield surface. The hardening internal state variable is a suitably chosen scalar measure of strain. A typical example is the von Mises effective plastic strain, also referred to as the von Mises equivalent or accumulated plastic strain, defined as

$$\bar{\varepsilon}^p = \int_0^t \sqrt{\frac{2}{3}\varepsilon^p : \varepsilon^p}\, dt \tag{2.35}$$

The von Mises isotropic strain-hardening model is obtained by letting the uniaxial yield stress be a function of the accumulated plastic strain

$$\sigma_y = \sigma_y(\bar{\varepsilon}^p) \tag{2.36}$$

The model is said to have linear hardening if and only if the strain-hardening function is linear such as

$$\sigma_y(\bar{\varepsilon}^p) = \sigma_{y0} + H\bar{\varepsilon}^p \tag{2.37}$$

The yield condition is written as

$$\Phi(\sigma, \bar{\varepsilon}^p) = |\sigma| - (\sigma_{y0} + H\bar{\varepsilon}^p) \tag{2.38}$$

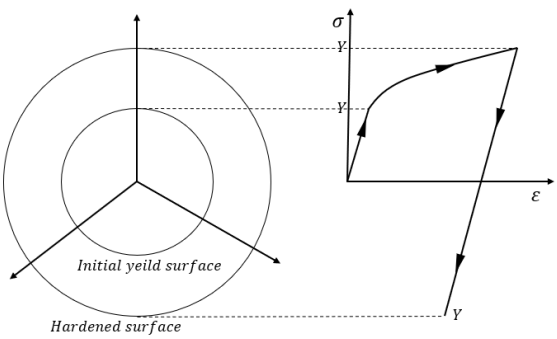

Figure 2.12: Isotropic Hardening illustration[18]

KINEMATIC HARDENING

When the yield surfaces preserve their shape and size but translate in the stress space as a rigid body, then the material undergoes kinematic hardening 2.13. It is frequently observed in experiments that, after being loaded (and hardened) in one direction, many materials show a decreased resistance to plastic yielding in the opposite direction. This phenomenon is known as the Bauschinger effect and can be modelled with the introduction of kinematic hardening. A simple phenomenological model that can capture

this effect is by introducing another variable q called as back stress, which defines the location of the center of the yield surface. The yield condition can be modified as

$$\Phi(\sigma, \overline{\varepsilon}^p) = |\sigma - q| - (\sigma_{y0} + H\overline{\varepsilon}^p) \tag{2.39}$$

The evolution of the back stress is defined as

$$\dot{q} = H\dot{\overline{\varepsilon}}^p \tag{2.40}$$

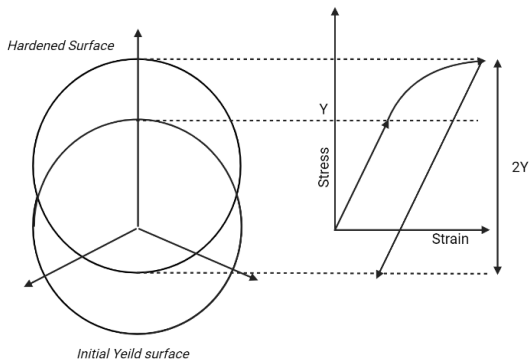

Figure 2.13: Kinematic Hardening [18]

2.6.6. NUMERICAL INTEGRATION ALGORITHM FOR ELASTOPLASTIC ANALYSIS

In the case of path-dependent materials, such as elastoplastic materials, the update scheme usually requires the formulation of a numerical algorithm for integration of the corresponding rate constitutive equations. This requirement stems from the fact that analytical solutions to the initial value problem defined by the elastoplastic equations are generally not known for complex strain paths.

ELASTIC TRIAL STEP

Initially, we assume that plastic strain does not occur; that is, we assume that the step $[t_n, t_{n+1}]$ is elastic. This is called as the elastic trial solution and will be denoted as

$$\varepsilon^{e,trial}_{n+1} = \varepsilon^e_n + \Delta\varepsilon \tag{2.41}$$

$$\alpha^{trial}_{n+1} = \varepsilon_n \tag{2.42}$$

The corresponding stress and hardening force will be called the elastic trial stress and elastic trial hardening force, given by

$$\sigma^{trial}_{n+1} = \overline{\rho}\frac{\partial\Psi}{\partial\varepsilon^e}\Big|^{trial}_{n+1} \tag{2.43}$$

$$A_{n+1}^{trial} = \overline{\rho}\frac{\partial \Psi}{\partial \alpha}\Big|_{n+1}^{trial} \tag{2.44}$$

The above variables are collectively called the elastic trial state. If

$$\Phi(\sigma_{n+1}^{trial}, A_{n+1}^{trial}) \leq 0 \tag{2.45}$$

that is, if the elastic trial state lies within the elastic domain or on the yield surface, we update the total strain and total stress as

$$\varepsilon_{n+1} = \varepsilon_{n+1}^{trial} \tag{2.46}$$

$$\sigma_{n+1} = \sigma_{n+1}^{trial} \tag{2.47}$$

PLASTIC CORRECTOR ALGORITHM

When the material is deforming plastically, then $\Delta\gamma > 0$, so the elastic strain is calculated as

$$\varepsilon_{n+1}^{e} = \varepsilon_{n+1}^{trial} - \Delta\gamma N \tag{2.48}$$

$$\alpha_{n+1} = \alpha_{n+1}^{trial} - \Delta\gamma H \tag{2.49}$$

The $\Delta\gamma$ is calculated by solving the residual function using numerical methods.

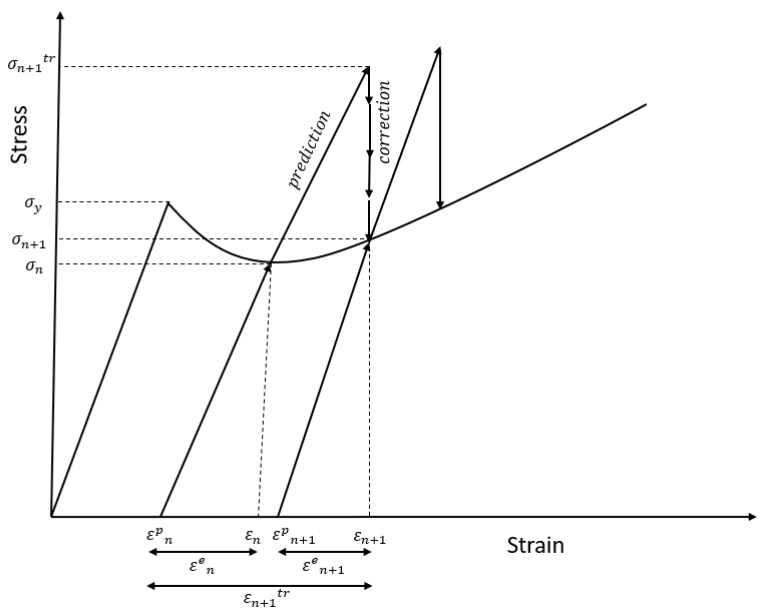

Figure 2.14: Return Mapping Algorithm [18]

2.7. CONSTITUTIVE MODELLING OF POLYMERS

Several constitutive models are developed to capture the nonlinear stress-strain behavior of polymers. Eyring's theory was initially developed to understand polymers' viscoplastic flow [20]. The Eyring's viscoplasticity rule is shown in equation 2.10. Later Howard et al. [21] was the first to decouple the stress, one part where the elastic response is modeled by Hookean elasticity and a single Eyring's dashpot represents the inelastic flow, and a second part concerning entropic strain hardening using a Langevin spring derived from the non- Gaussian statistics as shown in figure 2.17. Argon [22] proposed a theory of yielding for glassy polymers based on the concept that deformation at a molecular level consists of forming a pair of molecular kinks. The shear yield stress (τ) is defined as

$$\tau = \frac{0.102G}{1-\nu}\left[1 - \frac{16(1-\nu)}{3\pi G\omega^2 a^3} KT \ln\left(\frac{\dot{\gamma}_0}{\dot{\gamma}}\right)\right]^{\frac{6}{5}} \tag{2.50}$$

where G, ν are the shear modulus and Poisson's ratio, a is the molecular radius, and ω is the angle of rotation of the molecular segment.

Boyce et al. [23] observed a drop in yield stress upon initiation of plastic deformation, a characteristic of both amorphous and semicrystalline polymers. Softening is accompanied by inhomogeneous deformation on a small scale in the form of shear bands. It was also observed that softening curve is different for quenched and annealed samples. The phenomenological evolution equation for the rate of drop accounting for the dependence of strain rate, structure, and temperature is defined as

$$\dot{s} = h\left(1 - \frac{s}{S_{ss}(T, \dot{\gamma}^p)}\right)\dot{\gamma}^p \tag{2.51}$$

Boyce et al. [23] developed the constitutive model considering the Argon viscoplastic flow rule, incorporating polymers' strain-softening behavior and pressure sensitivity. Boyce et al. [24], assumed that to model the stress rise due to locking and stretching of polymers at high strains, polymers behave like rubber and used entropic-network models. Further, Arruda and Boyce [25] developed the entropic strain hardening, well-known as the eight chain model to capture the stress rise shown in equation 2.64. Another major constitutive approach was proposed by Leonov [26], from which a compressible version was developed by Baaijens [27] that, in turn, was later derived within a thermodynamically consistent framework by Tervoort et al. [28]. To capture the typical characteristics of the post-yield behaviour of glassy polymers, namely the phenomenon of strain softening and hardening, Timmermans [29] and Govaert et al. [30] extended Tervoort et al. [28] model, leading to the generalized compressible Leonov model, currently known as the Eindhoven Glassy Polymer (EGP) model. Inspired by this EGP model, Mirkhalaf et al. [2] recently proposed a finite strain, elasto-viscoplastic constitutive model assuming the isothermal deformation. The common factors in these models are stress-dependent viscosity to capture deformation kinetics and rubber elasticity to model strain hardening.

Many studies observed that viscous behavior contributes to self-heating in a material, where deformation is adiabatic. In the studies performed by Adams and Farris [31] and

Boyce et al. [32], it was found that about 50 to 80% of the total mechanical work was converted into heat in glassy polymers. On the other hand, studying a semicrystalline high-density polyethylene (HDPE), Hillmansen et al. [33] and Hillmansen and Haward [34] observed that almost the entire mechanical work was converted into heat. A similar observation was also done by Johnsen et al. [35] on a crosslinked low-density polyethylene (XLPE). Since heating of the polymer material will introduce thermal softening, it is evident that a correct prediction of heat generation during deformation is crucial for the constitutive model to capture the material behavior over a range of strain rates.

Consequently, taking thermomechanical coupling into account is essential in this situation, mainly accounting for heat conduction within the material and heat convection to the surroundings. Arruda et al. [36] and Boyce et al. [37] combined an elasto-viscoplastic and kinematic hardening based on the alignment of the polymer chains, including self-heating of polymers. Adopting a similar approach, Richeton et al. [38] presented a model able to span the glass transition temperature. Anand et al. [39] and Ames et al. [3] presented a thermomechanically coupled constitutive model describing the finite deformation behavior of amorphous polymers considering the self-heating of the polymers. Back stress evolution law is also considered to capture the effect of the nonlinear kinematic-hardening. In the study by Srivastava et al. [40] the model presented by Ames [3] was extended to span the glass transition temperature. However, the model introduces many material parameters, making the calibration process complex. More recent developments were made by Gonzalez et al. [41], who extended the isothermal model proposed by Loria et al. [42] to include thermomechanical coupling. This model combines an elastic Neo-Hookean response with rate-dependent yielding and plastic flow governed by the Raghava yield function and kinematic hardening modeled by an eight-chain spring.

Hachour et al. [43] examined the mechanical behavior of HDPE on round notch specimens with different stress triaxiality ratios and verified the classical yield criteria such as von-Mises, Tresca, and Raghava yield functions through the measurement of a biaxial yield envelope. Timmermans [29] implemented the EGP model for polypropylene. Popa et al. [44] proposed a homogenization approach for the numerical implementation of the visco-elastic visco-plastic behavior of semicrystalline polymers at large deformations. The approach describes the two material phases of a semicrystalline polymer, amorphous and crystalline, and provides the means of relating them to the macroscopic scale of the material by describing a representative mesostructure (RMS) and by defining the set of variables that influence the model. Manaia et al. [45] analyzed the yielding response of high-density polyethylene (HDPE) under different stress states and strain rates and examined the ability of Von Mises and Drucker-Prager yield criteria to capture their deformation. Bergstorm et al. [46] developed a hybrid model inspired from Arruda et al. [47] and Hasan et al. [48] to predict the behaviour of ultra-high molecular weight polyethylene (UHMWPE) under tensile and cyclic loading. Seden et al. [49] concluded that the tensile yield stress at a single strain rate and across a wide range of temperatures contributes to the β relaxation process. Later the constitutive model developed by Johnsen et al. [1] extended this considering the two Eyring's dashpots representing both α and β relaxations to analyze the tensile behavior of LDPE and polypropylene. Ries

et al. [50] studied the tensile behavior of PCR-HDPE, concluding that temperature and strain rate greatly influence the mechanical response of the recycled HDPE. The stress-strain behavior of PCR-HDPE is captured using a viscoelastic model. Wang et al. [51] experimentally investigated and modeled the effect of reprocessing on the quasi-static uniaxial tensile behavior of two commercial unfilled and talc-filled polypropylene-based composites. From the experimental results, they observed that Young's modulus (E) and failure strain (ϵ_b) continuously decrease with the reprocessing number N_p. The effect of E and ϵ_b on reprocessing number developed to model the behavior of PCR-PP is given as

$$E(N_p,\dot{\epsilon}) = (K_1 N_p + E_0)\left(1 + (\zeta_1 N_p + \lambda_E)\ln\left(\frac{\dot{\epsilon}}{\dot{\epsilon}_0}\right)\right) \tag{2.52}$$

$$\epsilon_b(N_p,\dot{\epsilon}) = (K_2 N_p + \epsilon_{b0})\left(1 + (\zeta_2 N_p + \lambda_{\epsilon_b})\ln\left(\frac{\dot{\epsilon}}{\dot{\epsilon}_0}\right)\right) \tag{2.53}$$

where N_p is the number of reprocessing and K_1 and K_2 are the reprocessing strengthening coefficient of Young's modulus and failure strain, respectively. ζ_1 and ζ_2 are the recycling strengthening coefficient of the strain rate.

The experimental results of PCR-PP and PCR-PE shown in the figure 3.1 and 4.1 provided by a research patner Lyondell Basel demonstrates the need for a robust constitutive model that can be tuned for a wide range of applications. The selection of the bulk phase constitutive models requires a model with the following qualities: 1) finite strain 2) strain rate and temperature-dependent yield strength 3) strain-softening, which occurs due to deformation-induced disordering or change in free volume 4) strain-hardening due to alignment of the polymer chains at large strains 5) temperature rise due to plastic dissipation at high strain rates. 6) able to capture deformation behavior at different stress tri-axialities.

After reviewing state-of-the-art polymer constitutive models, the models developed by Johnsen et al. [1], Mirkhalaf et al. [2], and Anand et al. [3] were selected to model the tensile behavior of PCR-PP and PCR-PE. The constitutive model developed by Johnsen et al. [1] is considered because of its ability to accurately predict the behavior of low-density crosslinked polyethylene (XLPE) [1] and polypropylene [35]. The model considers Eyring's viscoplastic flow rule to capture temperature and strain rate-dependent yield stress. In addition the model considers Arruda and Boyce's eight chain model to capture the strain hardening behavior. The model also incorporates the effect of thermal softening. Mirkhalaf model [2] is a finite strain elasto-viscoplastic constitutive model developed to predict the non-linear behavior of polymeric-based materials incorporating pressure and softening effects to characterize the post-yield response properly, which is not implemented in the Johnsen model. However, the model assumes isothermal deformation ignoring the thermal softening. Another model developed by Anand et al. [3] that was developed to predict the behavior of PC, PMMA, and Zenox material. Similar to the Mirkhalaf model, the model considers pressure dependence and strain softening effect. In addition, the model also considered the effect of self-heating due to plastic dissipation. Since it considers many fitting parameters, the model accurately captures

the yield and post-yield response. Note that all models were manually optimized by the authors to obtain a correct description of the post-yield response.

In the current thesis, the suitability of the three models predicting the mechanical behaviour of PCR-PE, and PCR-PP is assessed. The models also should account for multi-axial loading conditions. However, the applicability of these models to non-trivial loading conditions has not been explored. To achieve this, simulations will be generated and compared with the standardized three-dimensional tensile test results and different stress triaxiality ratios. Finally, given the complexity of the models, material parameter calibration is performed using Bayesian optimization coupled with ABAQUS when provided with the experimental data. In the next sections 2.7.1, 2.7.2 and 2.7.3, the major aspects of the general constitutive theories of models are outlined and implementation details of the models are described in appendix A. In section 2.8 the calibration methods are reviewed briefly.

2.7.1. JOHNSEN MODEL

The Thermo-elasto-viscoplastic constitutive model of polymers proposed by Johnsen et al. [1] is developed to study the non-linear mechanical behavior of low-density cross-linked polymers. The constitutive model also describes the effect of self-heating of the polymers at higher strain rates. The proposed model is schematically represented in figure 2.15 and consists of two parts. Part A of the model captures the thermo-elastic and thermo-viscoplastic responses of the polymers. The two Ree-Eyring dashpots represent the effects of both α relaxation and β relaxation on the plastic response. The α and β relaxation of the polymers represents the relaxation of the carbon atoms in the main chain and relaxation of the side group atoms, respectively. Finally, part B of the model captures the orientational hardening of the polymers due to the alignment of the chains during deformation.

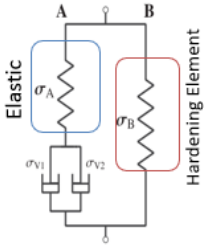

Figure 2.15: Rheological model of Johnsen Model [1]

HYPERELASTIC CONSTITUTIVE LAW

The specific free energy of the material is a isotropic scalar function generally. The different specific energy functions are considered based on the response of the material during the deformation. Later the Kirchoff stress tensor can be calculated from the free

energy function as shown in the equation below.

$$\tau_A = 2\rho \frac{\partial \Psi_A}{\partial B_A^e} B_A^e \tag{2.54}$$

where B_A^e is the left Cauchy-Green elastic deformation tensor. In the present model the elastic response is defined using the Hencky free energy function. The Hencky elastic theory captures the elastic response well for large deformations.

$$\rho \Psi_A = \mu_A(T) \mathrm{Tr}[(ln(V^e)^2] \tag{2.55}$$

Where ρ is the density T is the absolute temperature. The shear moduls of the elastic region is defines as

$$\mu_A(T) = \mu_{A,ref} \exp[-a_A(T - T_{ref})] \tag{2.56}$$

The Kirchoff stress tensor τ is calculated from the Hencky free energy function as

$$\tau_A = 2\mu_A(ln(V_A^e)) \tag{2.57}$$

From the above equation it can be observed that Kirchoff stress and logarithmic strain have the linear relationship. The Cauchy stress tensor is defined as

$$\sigma_A = \frac{1}{J}\tau_A \tag{2.58}$$

VISCOPLASTIC CONSTITUTIVE LAW

From the rheological model the contribution from each dashpot is additive to capture both α and β relaxation. Hence the viscous stress equation is shown below.

$$\sigma_V = \sum_{x=\alpha,\beta} \frac{K_B T}{V_x} \mathrm{arcsinh}\Big(\frac{\dot{p}}{\dot{p}_{0,x}^*} \exp\Big[\frac{\Delta H}{RT}\Big]\Big) \tag{2.59}$$

where $\dot{p}$ is the equivalent plastic strain rate, ΔH is the activation enthalpy, V_x is the activation volume and R is the gas constant. Further $p_{0,x}^*$ is the deformation dependent reference equivalent plastic strain rate given by

$$\dot{p}_{0,x}^* = \dot{p}_{0,x} \exp\Big[-\sqrt{\frac{2}{3}} b_x ||ln(V_A^p)||_2\Big] \tag{2.60}$$

To define the plastic flow rule, the plastic potential is defined assuming the yield stress is approximately equal in both tension and compression and using von Mises equivalent stress to get

$$g(\sigma_D) = \sqrt{\frac{3}{2}\sigma_D : \sigma_D} \tag{2.61}$$

The plastic rate deformation tensor is calculated from the associated flow rule as

$$D_A^p = L_A^p = \dot{\lambda} \frac{\partial g(\sigma_D)}{\partial \sigma_D} \tag{2.62}$$

The direction of the plastic flow N is calculated from the gradient of the plastic potential function

$$N = \frac{\partial g(\sigma_D)}{\partial \sigma_D} = \frac{3}{2} \frac{\sigma_D}{g(\sigma_D)} \tag{2.63}$$

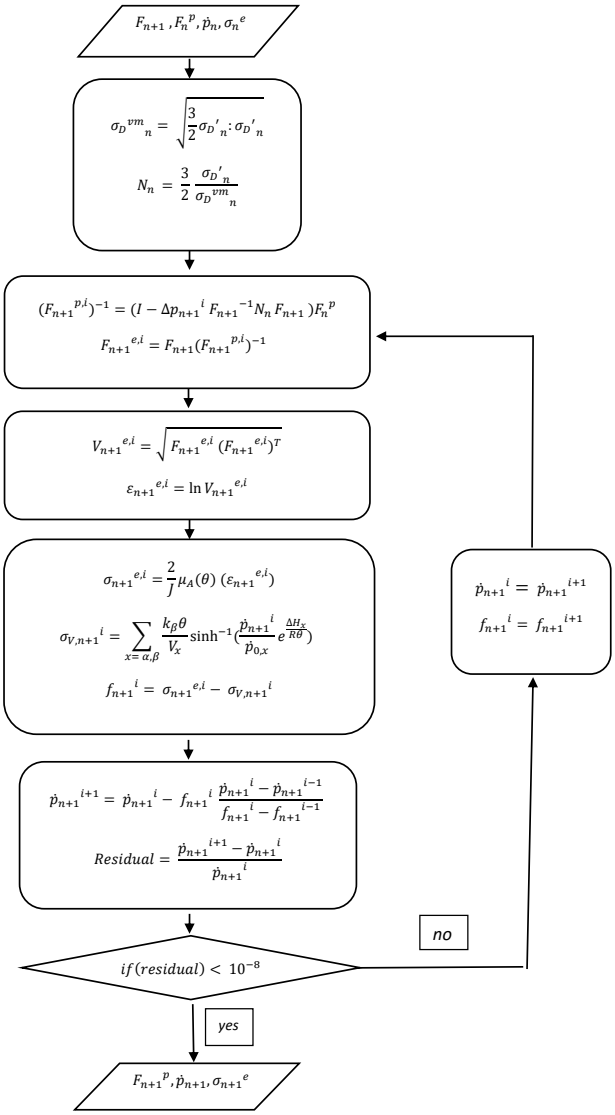

Figure 2.16: Numerical Implementation of Johnsen model

ORIENTATIONAL HARDENING

Orientational hardening of the polymers occurs due to the alignment of the polymer chains. The eight chain model is considered leading to the Kirchoff stress equation

$$\tau_{B,n+1} = \frac{\mu_B(T)\lambda_{lock}}{3\overline{\lambda}_{c,n+1}} L^{-1}\left(\frac{\overline{\lambda}_{c,n+1}}{\lambda_{lock}}\right) B_{D,n+1} - \kappa_B \ln(J_{n+1} I - 3\kappa_B \alpha (T_n - T_0) I \tag{2.64}$$

where λ_{lock} is the locking stretch, $\overline{\lambda}_c = \sqrt{tr(B)/3}$ is the average chain stretch, α is the thermal expansion and κ_B is the bulk modulus. The inverse Langevin function is defined as

$$L^{-1} = \chi \frac{3 - 2.6\chi + 0.7\chi^2}{(1-\chi)(1+0.1\chi)} \tag{2.65}$$

SELF HEATING

During the plastic deformation, the heat dissipation increases the temperature. The energy balance is expressed as

$$\rho_0 \dot{u} = \tau : D + r - div(q) \tag{2.66}$$

where r is the external heat sources and q is the heat flux. The heat equation gives the temperature rise

$$\rho_0 \overline{C}_v \dot{T} = \tau_D : D_A^p + \tau_B : D - T a_A \tau_A : D_A^e - \kappa_B [\ln J + 3\alpha T_0] tr(D) + r - div(q) \tag{2.67}$$

2.7.2. MIRKHALAF MODEL

The elasto-viscoplastic constitutive model of polymers proposed by Mirkhalaf et al. [2], [52] was developed for studying the non-linear mechanical behavior of glassy polymers. The constitutive model also describes and captures the strain-softening behavior of the polymers. The proposed model is schematically represented in figure 2.17. Part A of the model captures the elastic and viscoplastic responses of the polymers. Part B is represented by the Langevin spring and captures the hardening of the polymers during deformation. Finally, the polymer considers a single relaxation mode and assumes that deformation is isothermal, considering no temperature rise during plastic deformation.

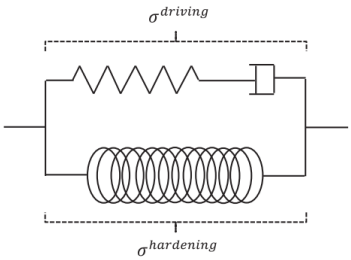

Figure 2.17: Rheological model of Mirkhalaf model [2]

HYPERELASTIC CONSTITUTIVE LAW

The specific free energy of the material is a isotropic scalar function generally. The different specific energy functions are considered based on the response of the material during the deformation. Later the Kirchoff stress tensor can be calculated from the free energy function as shown in the equation below.

$$\tau = \rho \frac{\partial \Psi}{\partial \varepsilon^e} \tag{2.68}$$

where ε^e is the logarithmic strain tensor. In the present model the elastic response is defined using the Hencky free energy function. The Hencky elastic theory captures the elastic response well for large deformations. The relation between the Kirchoff stress and Cauchy stress is as follows

$$\tau = J\sigma \tag{2.69}$$

where J is the determinant of the deformation gradient. The Hencky strain energy function in terms of the principal stretches is defined as

$$\rho\Psi(\lambda_1^e, \lambda_2^e, \lambda_3^e) = G[(\lambda_1^e)^2 + (\lambda_2^e)^2 + (\lambda_3^e)^2] + \frac{1}{2}\left(K - \frac{2}{3}G\right)[\ln(\lambda_1^e\lambda_2^e\lambda_3^e)]^2 \tag{2.70}$$

where $\lambda_1^e, \lambda_2^e, \lambda_3^e$ are the principal stretches and K is the bulk modulus and G is the shear modulus of the material. The Kirchoff stress and logarithmic strain relation is defined as

$$\tau = D^e : \varepsilon^e \tag{2.71}$$

where D^e represents the fourth order isotropic elastic tensor

$$D^e = 2GI_s + \left(K - \frac{2}{3}G\right) I \otimes I \tag{2.72}$$

The symbol I_s represents the fourth order Identity tensor and I represents the second order identity tensor.

VISCOPLASTIC FLOW RULE

The one dimensional flow rule described in Eyring's theory as

$$\dot{\gamma}^p = \frac{1}{A}\sinh\left(\frac{\tau}{\tau_0}\right) \tag{2.73}$$

where A and τ_0 are material constants depends on temperature, τ is the shear stress and $\dot{\gamma}_p$ is the rate of the plastic multiplier. The material constants are defined as a function of temperature

$$A = A_0 \exp\left(\frac{\Delta H}{RT}\right), \tau_0 = \frac{RT}{V} \tag{2.74}$$

where ΔH is the activation energy, V is the shear activation volume. The scalar A_0 is the constant related to the fundamental vibration and T is the absolute temperature. From the definition of Newton law of viscosity, the shear stress can be written as

$$\tau = \eta(\dot{\gamma}^p)\dot{\gamma}^p \tag{2.75}$$

From the trivial algebraic manipulations the equation (2.73) can be written as

$$\tau = \dot{\gamma}^p \tau_0 (\text{arcsinh}(A\dot{\gamma}^p)/\dot{\gamma}^p) \tag{2.76}$$

on comparing with the equation (2.75).

$$\eta(\dot{\gamma}^p) = \tau_0 (\text{arcsinh}(A\dot{\gamma}^p)/\dot{\gamma}^p) \tag{2.77}$$

where η is the viscosity function of the plastic multiplier rate. The Eyring's flow rule described in three dimensions can be written as the following relation.

$$\dot{\gamma}^{eq} = \frac{1}{A} \sinh\left(\frac{\tau^{eq}}{\tau_0}\right) \tag{2.78}$$

where τ_{eq} is the equivalent stress defined as

$$\tau^{eq} = \sqrt{\frac{1}{2}\tau_d : \tau_d} \tag{2.79}$$

where τ_d is the deviatoric part of the stress tensor. The associated flow rule to determine the rate of plastic deformation tensor

$$d^p = \dot{\gamma}^{eq} N \tag{2.80}$$

where N is the flow vector, represents the direction of plastic flow and defined as

$$N = \frac{\partial \Psi}{\partial \tau} \tag{2.81}$$

Ψ is the dissipation potential defined as the convex scalar function.

$$\Psi = \sqrt{\frac{1}{2}\tau_d : \tau_d} \tag{2.82}$$

So, the flow vector can be rewritten as

$$N = \sqrt{\frac{1}{2}} \frac{\tau_d}{||\tau_d||} \tag{2.83}$$

On substituting N in the associative flow rule, d^p can be rewritten as

$$d^p = \dot{\gamma}^{eq} \sqrt{\frac{1}{2}} \frac{\tau_d}{||\tau_d||} \tag{2.84}$$

On substituting the relations (2.78) and (2.79) in associative plastic flow rule and written as

$$d^p = \frac{\tau_d}{2A\left[\frac{\tau_{eq}}{\sinh\left(\frac{\tau^{eq}}{\tau_0}\right)}\right]} \tag{2.85}$$

which can be represented as

$$d^p = \frac{\tau_d}{2\eta(\tau_{eq})} \tag{2.86}$$

where the viscosity function is rewritten as

$$\eta(\tau_{eq}) = A\left[\frac{\tau_{eq}}{\sinh\left(\frac{\tau^{eq}}{\tau_0}\right)}\right] \tag{2.87}$$

EFFECT OF PRESSURE AND SOFTENING

The material parameter introduced above is purely deviatoric. Pressure and softening effects need to be considered in order to characterize the post-yield response properly. So the material parameter A is generalized as

$$A = A_0 \exp\left[\frac{\Delta H}{RT} + \frac{\mu P}{\tau_0} - D\right] \tag{2.88}$$

The material parameter μ represents the pressure coefficient and is defined as the ratio of the shear activation volume to the pressure activation volume.

$$\mu = \frac{\Omega}{V} \tag{2.89}$$

and P is the total hydrostatic pressure defined as the sum of atmospheric pressure (p_0) and hydrostatic pressure(p)

$$p = -\frac{1}{3}\mathrm{Tr}(\tau), \;\; P = p + p_0 \tag{2.90}$$

The phenomenological law proposed to consider the effects of softening is [53]

$$\dot{D} = h\left(1 - \frac{D}{D_\infty}\right)\dot{\gamma}^{eq} \tag{2.91}$$

where D_∞ is the saturation value of the softening parameter and h influences the softening slope. By algebraic manipulations and substituting the equations (2.88) and (2.91) in equation (2.87), the following viscosity function is obtained.

$$\eta = A_0 \exp\left[\frac{\Delta H}{RT} + \frac{\mu P}{\tau_0} - D_\infty + D_\infty \exp\left(\frac{-h\sqrt{3}\overline{\varepsilon}^p}{\sqrt{2D_\infty}}\right)\right]\left[\frac{\tau^{eq}}{\sinh\left(\frac{\tau^{eq}}{\tau_0}\right)}\right] \tag{2.92}$$

where $\overline{\varepsilon}^p$ is the equivalent accumulated strain.

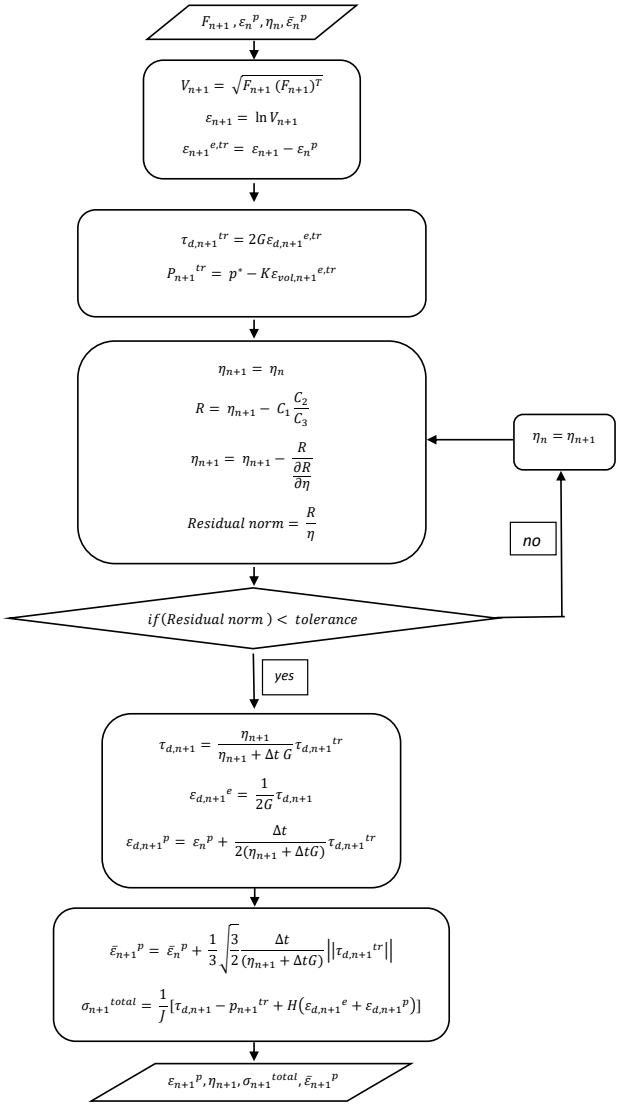

Figure 2.18: Numerical implementation of Mirkhalaf model

HARDENING LAW

In the final phase of the deformation behavior, which typically occurs at large strains, softening reaches its saturation value and the true stress increases with increasing strain. This phase is known as hardening. The hardening stress is evaluated using the equation

$$\tau^{hardening} = H\varepsilon_d \tag{2.93}$$

The total Kirchoff stress is the sum of the driving stress and hardening stress

$$\tau^{total} = \tau^{driving} + \tau^{hardening} \tag{2.94}$$

Total Cauchy stress can be written as

$$\sigma^{total} = \frac{1}{J}(\tau^{driving} + \tau^{hardening}) \tag{2.95}$$

2.7.3. ANAND MODEL

Another important constitutive model for polymers is proposed by Ames et al. [3] further developed in [54] to study the nonlinear mechanical behavior of polycarbonate, PMMA and zenox. The constitutive model also describes the effect of strain softening and self-heating of the polymers at higher strain rates. The derivation of the stiffness matrix is shown in appendix A.

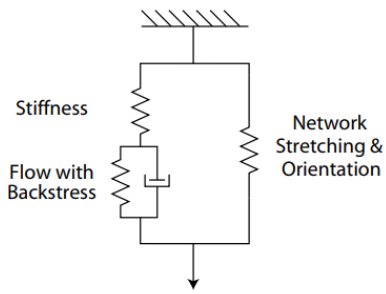

Figure 2.19: Rheological model of Anand model [3]

FREE ENERGY FUNCTIONS

We consider the free energy to have a separable form

$$\Psi = \Psi^{e(1)} + \Psi^{p(1)} + \Psi^{(2)} \tag{2.96}$$

With

$$U^e = \sum_{i=1}^{3} \lambda_i^e r_i^e \otimes r_i^e \tag{2.97}$$

denoting the spectral representation of U^e, and with

$$E^e = \sum_{i=1}^{3} E_i^e r_i^e \otimes r_i^e, E_i^e = \ln \lambda_i^e \tag{2.98}$$

where E^e denotes an elastic logarithmic strain measure, We adopt the following special form for the free energy.

$$\Psi^{e(1)} = G|E^e|^2 + \frac{1}{2}\left(K - \frac{2}{3}G\right)(tr(E^e))^2 - (T - T_0)(3K\alpha)(\mathrm{Tr}(E^e)) \tag{2.99}$$

The temperature-dependent parameters G, K and α are the shear modulus, bulk modulus, and coefficient of thermal expansion, respectively, and T_0 is a reference temperature. Furthermore, with

$$A = \sum_{i=1}^{3} a_i I_i \otimes I_i \tag{2.100}$$

denoting the spectral representation of A, we adopt a free energy $\Psi^{p(2)}$ of the form

$$\Psi^{p(1)} = \frac{1}{4}B[(\ln a_1)^2 + (\ln a_2)^2 + (\ln a_3)^2] \tag{2.101}$$

where the positive-valued temperature-dependent parameter B is a back-stress modulus. We adopt the following special form for free energy

$$\Psi^{(2)} = -\frac{1}{2}\mu I_m \ln\left(1 - \frac{I_1 - 3}{I_m}\right) \tag{2.102}$$

I_m and μ are two temperature-dependent material constants. In particular, μ represents the rubbery shear modulus of the material in the ground state, and I_m represents the upper limit of (I_1 - 3), associated with limited chain extensibility.

STRESS

Corresponding to the special free energy functions considered above, the Cauchy stress is given by

$$\sigma = \sigma^{(1)} + \sigma^{(2)} \tag{2.103}$$

with

$$\sigma^{(1)} = J^{-1} R^e M^e R^{eT} \tag{2.104}$$

where

$$M^e = 2GE_d^e + K(trE^e)I - 3K\alpha(T - T_0)I \tag{2.105}$$

M^e is the Mandel stress. The symmetric and deviatoric backstress is defined by

$$M_{back} = B \ln A \tag{2.106}$$

The driving stress for plastic flow is the effective stress given by

$$M_{eff}^e = M_d^e - M_{back} \tag{2.107}$$

The corresponding equivalent shear stress and mean normal pressure are given by

$$\overline{\tau} = \frac{1}{\sqrt{2}}|(M^e_{eff})_d \ , \overline{p} = -\frac{1}{3}tr(M^e) \tag{2.108}$$

respectively. Also,

$$\sigma^{(2)} = J^{-1}\mu\Big(1 - \frac{I_1 - 3}{I_m}\Big)^{-1}(B_{dis,d}) \tag{2.109}$$

The internal variables of the theory $\varphi > 0, S_a > 0, S_b > 0$, represent aspects of the intermolecular shear resistance to plastic flow. The parameter φ is a dimensionless order-parameter representing a local measure of disorder of the polymeric glass. S_a and S_b have dimensions of stress, respectively, and represent the aspects of a transient shear resistance accompanying microstructural disordering, and the aspects of increased shear resistance to plastic flow as the chains are pulled taut between entanglements at large strains.

FLOW RULE

The evolution equation for the plastic deformation gradient tensor (F^p) is

$$\dot{F}^p = D^p F^p \tag{2.110}$$

where D^p rate of plastic strain tensor

$$D^p = \nu\Big(\frac{(M^e_{eff})_d}{2\overline{\tau}}\Big) \tag{2.111}$$

The consistency equation is

$$\tau_e = \tau - S_a - S_b - \alpha_p\overline{p} \tag{2.112}$$

where τ_e denotes a net shear stress for thermally activated flow, α_p is a pressure sensitivity parameter.

$$\nu^p = \nu_0 \exp\Big[-\frac{Q}{K_B T}\Big]\Big[\sinh(\frac{\tau_e V}{2K_B T})\Big]^{\frac{1}{m}} \tag{2.113}$$

ν_0 is a preexponential factor with units of 1/time; Q is an activation energy, K_B is Boltzmann's constant, V is an activation volume, and m is a strain rate sensitivity parameter.

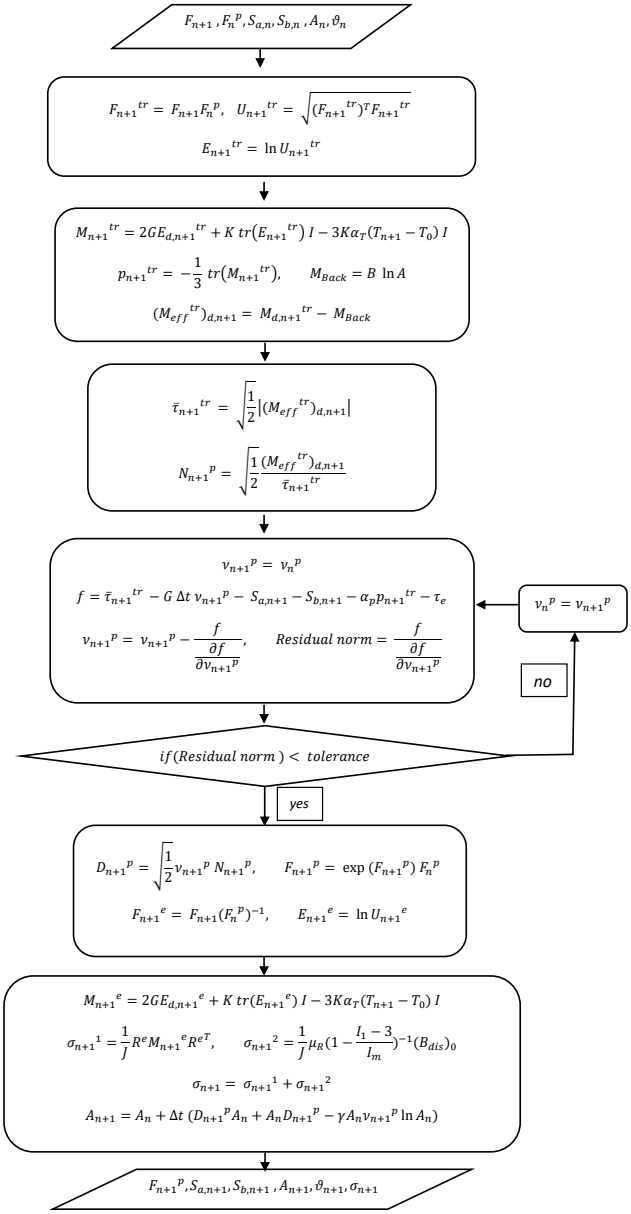

Figure 2.20: Numerical implementation of Anand Model

EVOLUTION EQUATIONS FOR THE INTERNAL VARIABLES

The internal variables S_a and φ are taken to obey the coupled evolution equations.

$$\dot{S}_a = h_a * (S_a^* - S_a)\nu^P \tag{2.114}$$

$$S_a^* = b * (\varphi^* - \varphi)\nu^P \tag{2.115}$$

$$\dot{\varphi} = g * (\varphi^* - \varphi)\nu^P \tag{2.116}$$

$$\varphi* = \varphi_r \left[1 + \left(\frac{T_c - T}{k}\right)^r\right]\left(\frac{\nu^p}{\nu^r}\right)^s \tag{2.117}$$

where

$$T_c = T_g + n \ln \frac{\nu^p}{\nu^r} \tag{2.118}$$

The evolution of s_b is assumed to be governed by

$$\dot{S}_b = h_b(\overline{\lambda} - 1)(S_b^* - S_b)\nu^p \tag{2.119}$$

Also, the evolution equation for A is taken as

$$\dot{A} = D^p A + AD^p - \gamma A \ln A \nu^p \tag{2.120}$$

where $\gamma \geq 0$ is a constitutive parameter which governs the dynamic recovery of A.

2.8. CALIBRATION OF MATERIAL PROPERTIES

The ability of a constitutive model to predict the deformation behavior of a specific material strongly depends on the values selected for the flexible material parameters. Therefore, an essential prerequisite for exploiting the full predictive capabilities of physics-based models lies in identifying the set of parameters within defined physical bounds. Identifying constitutive parameters requires solving an inverse problem, i.e., adjusting material parameters until the simulation results match the experimental data. It is often possible to calibrate simple constitutive models with a small number of material parameters using a trial-and-error or regression approach. However, it is impractical for complex constitutive models with many material parameters. Therefore, using an appropriate optimization methodology to determine the constitutive model parameters is crucial for both existing and developing new constitutive laws [55].

Gradient-based optimization methods, such as Newton's methods, have often been used for this calibration. Mahnken and Stein [56], Saleeb et al. [57] used a gradient-based method to identify the material parameters for viscoplastic material models. Yang and Elgamal [58] used a gradient-based method to determine material parameters for a multisurface plasticity sand model. However, one of the main drawbacks of gradient-based methods is their sensitivity to the choice of the initial guess. In other words, the converged solution and the convergence rate are highly dependent on the initial guess. This is particularly challenging for complex constitutive laws with nonlinear response.

For direct search methods such as genetic algorithms (GA), a substantial number of evaluations of the objective functions are needed to determine the quality of potential solutions. Therefore, the efficiency of these methods is directly dependent on the computational costs of the functions evaluated. Andrade-Campos et al. [59], ; Qu et al. [60],

Furukawa et al. [61] evaluated the material parameters of viscoplastic models using a genetic algorithm. To get convergence, GA requires large number of simulations to fit material parameters, extracting the outputs, and comparing them with the experimental data. The computational costs of plasticity simulations are generally too high [62].

To overcome this intrinsic difficulty, inverse optimization techniques which build up a surrogate model (Zhou et al. [63] Sedighiani et al. [55]) of the objective function turn out to be helpful. Such a surrogate model serves as an approximation of the true objective function. Bayesian optimization constructs regression model usually from Gaussian processes seeking the optimum solution in fewer iterations than competing algorithms. Kuhn et al. [62] proposed Bayesian optimization framework to calibrate the the material properties for crystal plasticity models and compared to the investigated evolutionary algorithm. The comparison proved that BO turned out to be consistently faster, and featured a smaller dispersion. In this work, we propose using Bayesian optimization with Gaussian processes for calibrating material parameters inversely based on tensile test experiments.

2.8.1. GAUSSIAN PROCESS REGRESSION

Gaussian process regression can serve as a valuable tool for performing inference both passively (for example, describing a given data set as best as possible, allowing one to also predict future data) as well as actively (for example, learning while choosing input points to produce the highest possible output [64].

In Gaussian process regression, we assume the output y of a function f at input x can be written as

$$y = f(x) + \epsilon \tag{2.121}$$

In the Gaussian process regression, we assume that *f(x)* is distributed as the Gaussian process.

$$f(x) \approx \mathscr{GP}(m(x),\ k(x,x')) \tag{2.122}$$

The Gaussian process is fully specified by the mean m(x) and covariance or kernel $k(x,x')$ functions:

$$m(x) = \mathbb{E}[f(x)] \tag{2.123}$$

$$k(x,x') = \mathbb{E}[(f(x) - m(x))(f(x') - m(x'))] \tag{2.124}$$

The kernel models the joint variability of random variables. The kernel sets prior information about the distribution and affects the convergence of the process. It usually assumes more similarity between close points and less between distant ones. A commonly

used kernel for smooth and stationary functions is the radial basis function (RBF) kernel with hyper parameters in the form of variance of the noise signal σ_f^2 and length-scale l [64].

$$k(x, x') = \sigma_f^2 \exp\left(-\frac{\| x - x' \|^2}{2l^2}\right) \tag{2.125}$$

The posterior predictions from GP are calculated using Baye's theory.

$$\text{posterior} = \frac{\text{prior} * \text{likelihood}}{\text{marginal likelihood}} \tag{2.126}$$

The posterior distribution is denoted as:

$$\begin{aligned} f_* | X_t, y_t, X_* \approx \mathcal{GP}\,(K(X_*, X_t)[K(X_t, X_t) + \sigma_\epsilon^2 I]^{-1} y_t, \\ K(X_*, X_t) - K(X_*, X_t)[K(X_t, X_t) + \sigma_\epsilon^2 I]^{-1} K(X_t, X_*) \end{aligned} \tag{2.127}$$

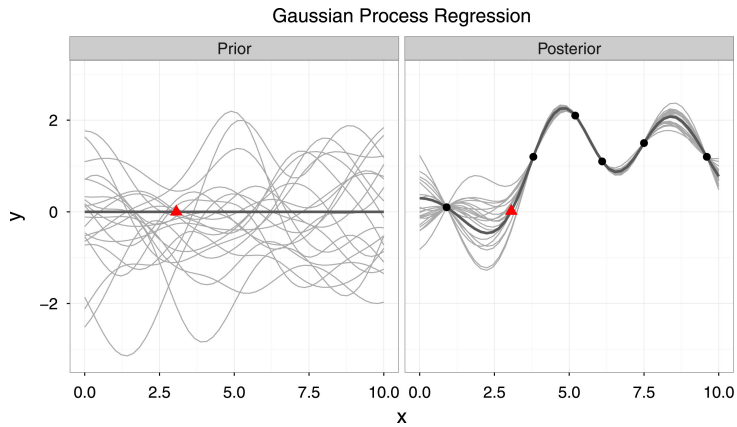

Figure 2.21: Samples from a Gaussian process prior and posterior. Grey lines indicate samples from the GP. Black dots mark empirical observations. The dark grey line marks the current mean of the GP. The red triangle shows the prediction for the new input point. [64]

The left side of the figure presents an initial belief about expected functions as a probability distribution. The average of functions presented in the figure is zero due to a lack of additional information. If it becomes available, the knowledge about functions and, therefore, the probability is updated. When new points become known, the prior probability function is combined with the likelihood, and a posterior distribution is obtained for which the functions pass through the known points.

2.8.2. BAYESIAN OPTIMIZATION

Bayesian optimization has become a common way of finding the optimal solutions in cases such as hyperparameter tuning for machine learning applications or constrained experiment design, for example, in the world of Materials Science. Typical global optimizers usually reach the minimum of the given function at the expense of multiple function evaluations. Bayesian optimization is applicable in situations where the cost of probing the values repeatedly is prohibitive, and one desires to reach the optimum quickly and at low expense [65].

The Bayesian approach towards optimization evaluates the black-box functions sequentially, meaning that data is evaluated and sampling continues until a satisfying result is obtained without a necessary predetermination of exact sample size. One may want to utilize the Gaussian Process (GP) surrogate model with an unknown function that is expensive to probe.

Bayesian optimization solves a problem by minimizing the objective function *f(x)*. The Gaussian process updates the prior belief about the function to pick the best location x^* for the next sample. The function is evaluated at the point x^*, and the posterior belief about it is updated with the Gaussian process. The next-point choice described is taken based on an acquisition function. An acquisition function which balances exploration and exploitation is the expected improvement. This expected improvement (EI) method tries to maximize the gain in the objective function. The expected improvement is defined by [66]

$$EI(x) = (\mu(x) - f(x^*) - \xi)\psi\left(\frac{\mu(x) - f(x^*) - \xi}{\sigma(x)}\right) + \sigma(x)\,\phi\left(\frac{\mu(x) - f(x^*) - \xi}{\sigma(x)}\right) \tag{2.128}$$

where $\mu(x)$ and $\sigma(x)$ are the mean and variance of the regressor at x, f is the function to be optimized with estimated maximum at x^*, ξ is a parameter controlling the degree of exploration and $\psi(z)$, $\phi(z)$ denotes the cumulative distribution function and density function of a standard Gaussian distribution [66].

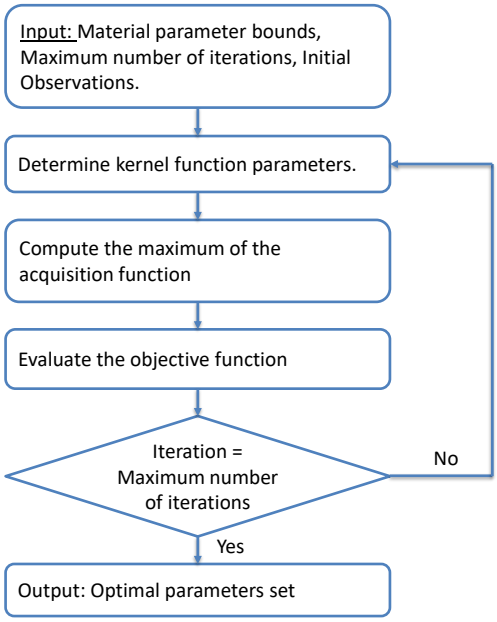

Figure 2.22: Bayesian optimization flow chart

3

THERMO VISCOPLASTIC ANALYSIS OF PCR-PP

In the current chapter, the mechanical response of PCR-PP was examined under tensile tests. The present investigation is particularly focused on the implementation robustness of the original three finite strain Thermo elasto-viscoplastic constitutive models [1], [2], [3] through its application to tensile tests. The Bayesian optimization approach presented here is used to determine an optimal set of parameters. It is especially suitable for complex models with a large number of parameters. The proposed approach also helps develop a comprehensive understanding of the relative influence of the different constitutive parameters and their interactions. With the optimal set of parameters obtained, the stress-strain response of PCR-PP is predicted for three different temperatures and strain rates. The results obtained are compared with the experimental results.

3.1. EXPERIMENTAL RESULTS

In this study, uniaxial tension tests were performed at three temperatures (T = 273 K, T = 296 K and T = 319 K) and three different cross-head velocities (v = 2 mm/min, v = 20 mm / min, and v = 200 mm/min). Assuming that all deformation happens over the parallel section of the tensile specimen, these cross-head velocities correspond to initial nominal strain rates ($\dot{\epsilon} = 1.667 * 10^{-3}\ s^{-1}$, $\dot{\epsilon} = 1.667 * 10^{-2}\ s^{-1}$ and $\dot{\epsilon} = 0.1667\ s^{-1}$).

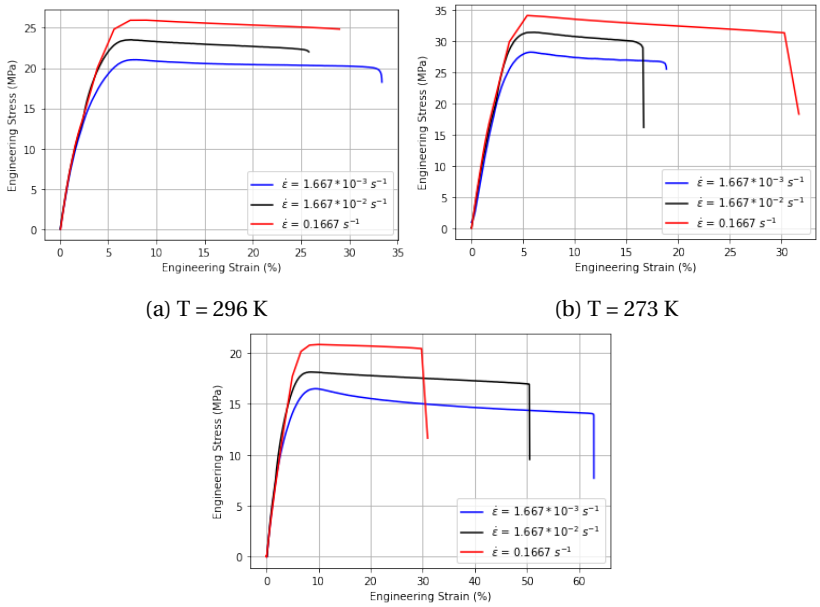

(a) T = 296 K (b) T = 273 K

(c) T = 319 K

Figure 3.1: Uniaxial tensile test results of PCR-PP

The stress-strain behaviour of PCR-PP (QCP 300) reported in figure 3.1. The experimental results show that an increase in temperature has a similar impact on young's modulus and the flow stress as a decrease in strain rate. The increase of temperature results in decrease of yield stress and young's modulus. The increase of strain rate results in the increase of yield stress, as the time required to slide over another will be less at the higher strain rates. The probability of forming knots increases. The higher strain rates, the higher the dissipation of energy, which in turn increases the temperature of the polymers, thereby reducing the stress value at large strains. It is observed that the strain hardening region also depends on the strain rate and temperature.

3.2. FINITE ELEMENT MODEL

The tensile test simulations were made in commercial finite element software program ABAQUS/standard, with the constitutive model implemented through the user material(UMAT) subroutine [67]. Due to the symmetry of the tensile specimen, symmetric boundary conditions were used to save computation time, as indicated in figure 3.2. Eight three-dimensional node elements with reduced integration and one thermal degree of freedom (C3D8RT) were used in all the simulations with an element size of 0.5 mm. The velocity of the testing machine is applied as the velocity boundary condition. In addition to the mechanical boundary conditions, a surface film with a heat transfer constant is applied on the free surface of the tensile specimen. The surface film simulates the convection of plastic dissipation energy to the environment. To analyze the

behavior of the material at different temperatures. The temperature is defined as a predefined field in ABAQUS, as the Johnsen and Anand models consider the self-heating of the material, the temperature rise is added to the previous step.

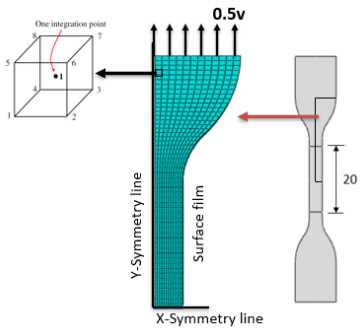

Figure 3.2: Finite Element Model with mesh (5A specimen)

3.3. CALIBRATION OF MATERIAL MODEL

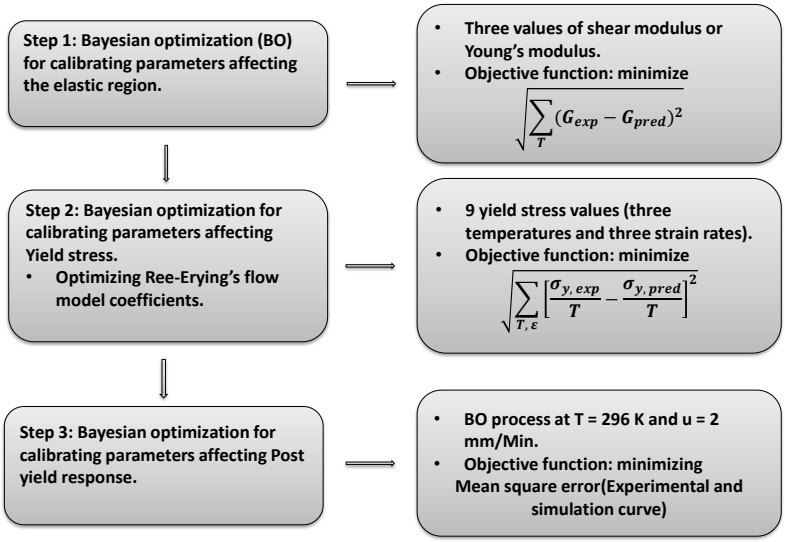

Figure 3.3: Procedure followed to calibrate material properties for the three models

The values of the material parameters of different constitutive models are calibrated from the experimental tensile test results using Bayesian optimization (BO). A brief overview of the calibration procedure is given in this section. The first step in the optimization is to determine the optimized temperature sensitivity parameters of the shear modulus. Finally, we optimize the material parameters that affect the yield stress in the second step using the viscoplastic flow stress equations. In the third step, the optimized parameters that affect the post-yield response are determined by coupling the BO tool (GPyOpt) and FEM software (ABAQUS) [68].

3.3.1. ELASTIC MATERIAL PROPERTIES

The values of shear modulus at different temperatures are estimated from the experimental data. As shown in figure 3.4, the experimental results clearly show that the shear modulus (G) is dependent on the strain rate and temperature. However, the strain rate dependence is not incorporated into the analysis, while the temperature dependence is considered in the three models. The objective function used to determine the temperature sensitivity parameters is the distance (d) between the experimentally determined shear modulus and the predicted shear modulus at three different temperatures. The shear modulus values are predicted using equations (3.3 - 3.5) for three temperature values.

$$\mathrm{d} = \sqrt{\sum_T (G_{\mathrm{exp}}(T,\dot{\epsilon}) - G_{\mathrm{pred}}(T,\dot{\epsilon}))^2} \tag{3.1}$$

or

$$\mathrm{d} = \sqrt{\sum_T (E_{\mathrm{exp}}(T,\dot{\epsilon}) - E_{\mathrm{pred}}(T,\dot{\epsilon}))^2} \tag{3.2}$$

To capture the temperature-dependent shear modulus (G), Johnsen et al. [1] considered an exponential relation developed by Arruda et al. [36]. The relation is shown in Equation 3.3.

$$G(T) = G_{ref} \exp[-a_A(T - T_{ref})] \tag{3.3}$$

where a_A is the temperature sensitivity factor.

Mirkhalf et al, [2] incorporated a temperature dependence relation developed by Melick et al. [69] assuming the ratio of Young's modulus at certain temperature to Young's modulus at reference temperature has the linear dependence on temperature.

$$E(T) = E_{ref}(\mathrm{a}T + \mathrm{b}) \tag{3.4}$$

Ames et al. [3] suggested that the approximate change of the shear modulus has a linear dependence on temperature.

$$G(T) = G_{ref} - \mathrm{M}(T - T_g) \tag{3.5}$$

The reference material properties are considered at room temperature (T_{ref} = 296 K) and the strain rate $\dot{\epsilon}$ = 0.001667 s^{-1}. The Poisson's ratio is assumed to be constant for all temperatures and strain rates.

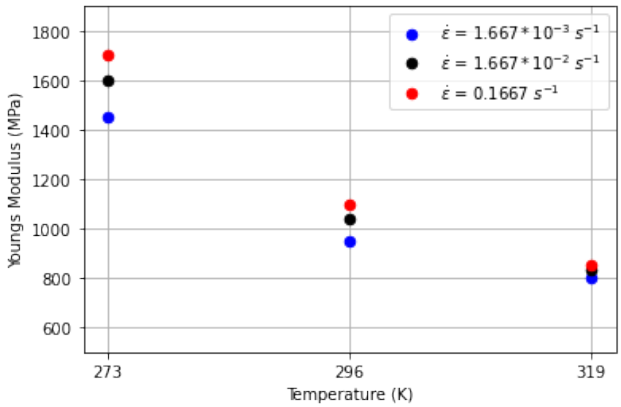

Figure 3.4: Temperature and strain rate dependence on the Young's modulus of the material.

The bounds of material parameters and the optimized temperature sensitivity parameters are mentioned in table 4.1.

Table 3.1: Temperature sensitivity parameters of Elastic properties after calibration

Material model	Properties	Units	Bounds of parameters	Values
Johnsen model	a_A	K^{-1}	[-5, 5]	0.015
Mirkhalaf model	a	(-)	[-1, 0]	-0.01365
	b	K^{-1}	[1, 6]	5.144
Anand model	M	K^{-1}	[2, 8]	5.023

3.3.2. FLOW STRESS

The coefficients in the Eyring flow model were estimated using the yield stress value obtained from the tensile stress-strain data for nine different configurations (three temperatures and three strain rates). Material properties affecting the peak yield stress are estimated by minimizing the error function

$$d = \sqrt{\sum_{T,\dot{\epsilon}} \left(\frac{\sigma_{y,exp}}{T} - \frac{\sigma_{y,pred}}{T} \right)^2} \tag{3.6}$$

The prediction of yield stress ($\sigma_{y,pred}$) is made using the viscoplastic flow rule. The flow rules considered in the three models are mentioned in this section.

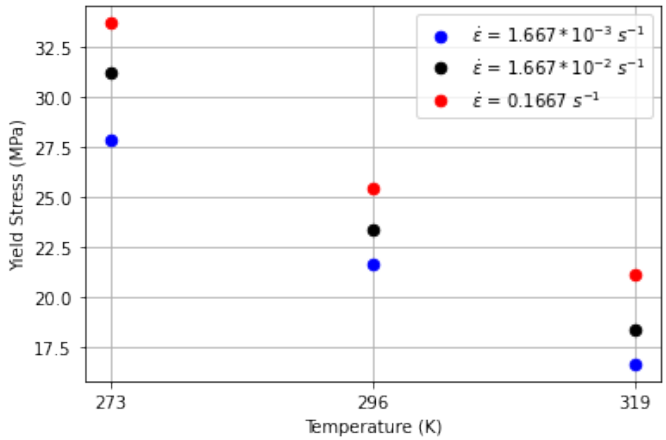

Figure 3.5: Temperature and strain rate dependence on the yield stress of the material PCR-PP.

The Johnsen rheological model considers two Eyring's dashpots representing both α and β relaxations. The flow stress contribution from each dashpot is considered to be additive. Thus, flow stress equation becomes

$$\frac{\sigma_y(\dot{p},T)}{T} = \sum_{x=\alpha,\beta} \frac{K_B}{V_x} \operatorname{arcsinh}\left(\frac{\dot{p}}{\dot{p}_{0,x}} \exp\left[\frac{\Delta H_x}{RT}\right]\right) \tag{3.7}$$

At the yield point, it is assumed that the plastic strain rate ($\dot{p}$) is equal to the total strain rate ($\dot{\epsilon}$).

The flow rule described by Mirkhalaf et al. [2], is mentioned in Equation (2.93). At yield, the plastic logarithmic strain rate can be made approximately equal to the total nominal strain rate. Since the beginning of plastic flow, no intrinsic softening has developed. During the uniaxial tensile test, the hydrostatic pressure is given by (p $= -\frac{1}{3}\sigma_y$). The incorporation of these considerations into equation (2.93), flow rule, leads to

$$\frac{\sigma_y(T,\dot{\epsilon})}{T} = \frac{3R}{\sqrt{3}V+\Omega}\left(\ln\left[A_0\dot{\epsilon}\right] + \frac{\Delta H}{RT} - \ln\left[\frac{\sqrt{3}}{6}\right]\right) \tag{3.8}$$

where V is the shear activation volume and Ω is the pressure activation volume. The pressure coefficient (μ) and characteristic stress (τ_0) are defined as

$$\tau_0 = \frac{RT}{V} \tag{3.9}$$

$$\mu = \frac{\Omega}{V} \tag{3.10}$$

The flow function considered in the model developed by Ames et al. [3] to capture yield stress is a modified Eyring's flow rule, developed by assuming probability of a successful cooperative event involving the simultaneous occurrence of m transitions which means that the yield point is reached when m segments of polymers move simultaneously [70], [71], that is in a cooperative way. The flow rule given in equation (2.112) denotes a net shear stress for thermally activated flow. The shear stress equation is converted to tensile assuming ($\tau = \frac{\sigma}{\sqrt{3}}$) as yield stress values pf PCR-PP and PCR-PE are estimated using tensile tests. Similarly to the Mirkhlaf model, the contribution of internal variables S_a and S_b associated with the strain softening behavior is neglected. Substituting equation (2.113) in (2.112) and performing simple algebraic manipulations, the flow stress equation becomes

$$\frac{\sigma_y(T,\dot{\epsilon})}{T} = \frac{2K_b}{V}\left(1-\frac{\alpha_p}{3}\right)^{-1} \operatorname{arsinh}\left[\left(\frac{\dot{\epsilon}}{\dot{\epsilon}_0}\right)^m\right] \tag{3.11}$$

where V is the shear activation volume, Q is the activation, α_p is the pressure coefficient and $\dot{\epsilon}_0$ is the reference plastic strain.

3.3.3. POST YIELD RESPONSE

The post-yield response of polymers includes strain softening and orientational hardening. The experimental results in the figure 3.1 show that PCR-PP has no strain-softening effect. So, material parameters that affect the softening have little impact on the optimization process. Bayesian optimization was implemented with the GPyOpt module [72] due to its simplicity and ease of connection with the FEM simulation software. Based on the review of the acquisition function summarized earlier, the Expected Improvement function was chosen for its trade-off in exploration and exploitation. The bounds of the material parameters of the three models that affect the post-yield response of PCR-PP are mentioned in Tables 3.2 - 3.4. The stress-strain curves of each model are calculated for values of material parameters at the maximum of the acquisition function and the objective function is evaluated. The process is repeated until the number of iterations is equal to the maximum number of iterations. The maximum number of iterations considered in the analysis 125. The value of a maximum number of iterations is selected based on the convergence of the respective models. Convergence is defined as the value of the objective function (MSE) at which it is not affected by the number of iterations. Optimization of these parameters is performed at room temperature (T = 296 K) and low strain rate ($\dot{\epsilon} = 0.001667 s^{-1}$), where isothermal conditions were met, resulting in an increase in low temperature rise due to plastic dissipation.

$$MSE = \frac{1}{n}\sum_{i=1}^{n}(\sigma_{exp,i} - \sigma_{sim,i})^2 \tag{3.12}$$

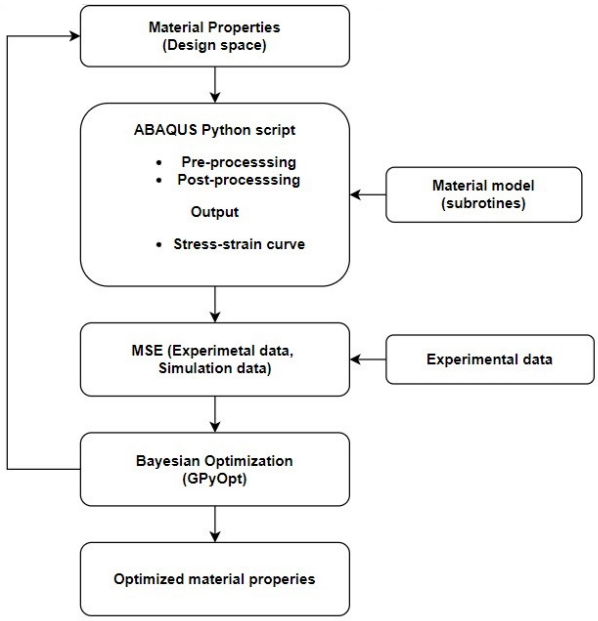

Figure 3.6: Bayesian optimization procedure for materials parameters affecting post yield response

After optimization, the material parameters of PCR-PP used in the subsequent simulations are presented in Tables 3.2 - 3.4.

Table 3.2: Material Properties of PCR-PP after calibration of Johnsen model

	Properties	Units	Bounds of parameters	PCR-PP
Elastic	G	MPa	(-)	380
	a_A	K^{-1}	[-5, 5]	0.015
Yield stress	ΔH_α	KJ/mol	[180, 230]	226.368
	V_α	nm^3	[3, 7]	4.27
	$\dot{p}_{0,\alpha}$	s^{-1}	$[1*10^{27}, 3*10^{27}]$	$2.238*10^{27}$
	ΔH_β	KJ/mol	[190, 240]	218.34
	V_β	nm^3	[3, 7]	3.35
	$\dot{p}_{0,\beta}$	s^{-1}	$[5*10^{38}, 6*10^{38}]$	$5.65*10^{38}$
Hardening	b_α	(-)	[6, 10]	10
	b_β	(-)	[11.5, 15]	12
	$\mu_{B,ref}$	MPa	[2,5]	2
	κ_B	MPa	[1400, 1550]	1423.72
	λ_{lock}	(-)	[3.5, 5]	3.75

Table 3.3: Material Properties of PCR-PP after calibration of Mirkhalaf model

	Properties	Units	Bounds of parameters	PCR-PP
Elastic	E	MPa	(-)	950
	ν	(-)	(-)	0.45
Yield stress	ΔH	J/mol	$[1*10^5, 4*10^5]$	212501.6
	A_0	s^{-1}	$[1*10^{29}, 1*10^{25}]$	$1.46*10^{-26}$
	V	m^3/mol	$[1*10^{-4}, 1*10^{-2}]$	0.00354
	Ω	m^3/mol	$[1*10^{-5}, 1*10^{-3}]$	0.000961
Softening	h	(-)	[120, 150]	149.91
	$D_{\infty,0}$	(-)	[0.1,0.8]	0.66
Hardening	H	MPa	[-5, -0.01]	-3.91

Table 3.4: Material Properties of PCR-PP after calibration of Anand model

	Properties	Units	Bounds of parameters	PCR-PP
Elastic	T_g	K	(-)	260
	ρ	Kg/m^3	(-)	900
	α	K^{-1}	(-)	$7*10^{-5}$
	G_0	MPa	(-)	570
	M	$MPa\ K^{-1}$	(-)	5.02
	ν_{poi}	(-)	(-)	0.43
Back stress	X	$MPa\ K^{-1}$	(-)	0
	γ	(-)	(-)	0
Yield stress	α_p	(-)	[0.3, 0.75]	0.326
	ν_0	s^{-1}	$[1*10^{17}, 1*10^{20}]$	$1.273*10^{19}$
	m	(-)	[0.3, 0.5]	0.32
	Q	J	$[1*10^{-21}, 1*10^{-18}]$	$2.799*10^{-19}$
	V	m^3	$[1*10^{-27}, 1*10^{-25}]$	$3.65*10^{-27}$
Softening	h_1	(-)	(-)	0
	b	MPa	(-)	0
	g_1	(-)	(-)	0
	g_2	K^{-1}	(-)	0
	ϕ_r	(-)	(-)	0
	k	K	(-)	-0.16
	r	(-)	(-)	0
	s	(-)	(-)	0
	ν_r	s^{-1}	(-)	0
	n	(-)	(-)	0
	h_2	(-)	(-)	0
	l_1	MPa	(-)	0
	l_2	$MPa\ K^{-1}$	(-)	0
Hardening	μ_0	MPa	[2, 5]	4.438
	N	$MPa\ K^{-1}$	(-)	0
	I_m	(-)	[25, 60]	44.5326
thermal	c_0	$J\ Kg^{-1}\ K^{-1}$	(-)	2120
	c_1	$J\ Kg^{-1}\ K^{-2}$	(-)	8
	κ_0	$Watt\ m^{-1}\ K^{-1}$	(-)	0.467
	κ_1	(-)	(-)	0.46
	ω	(-)	(-)	0.8

3.4. RESULTS

3.4.1. TENSILE TESTS

The comparison of the numerical and experimental results of PCR-PP are presented in this section. All the numerical and experimental results are obtained from the uniaxial tension tests shown in the figures 3.7, 3.8 and 3.9. Nine different configurations of temperature and strain rates were investigated in total: three temperatures 296 K, 273 K and

319 K for each temperature three nominal strain rates of $1.667 * 10^{-3}\ s^{-1}$, $1.667 * 10^{-2}\ s^{-1}$ and $0.1667\ s^{-1}$.

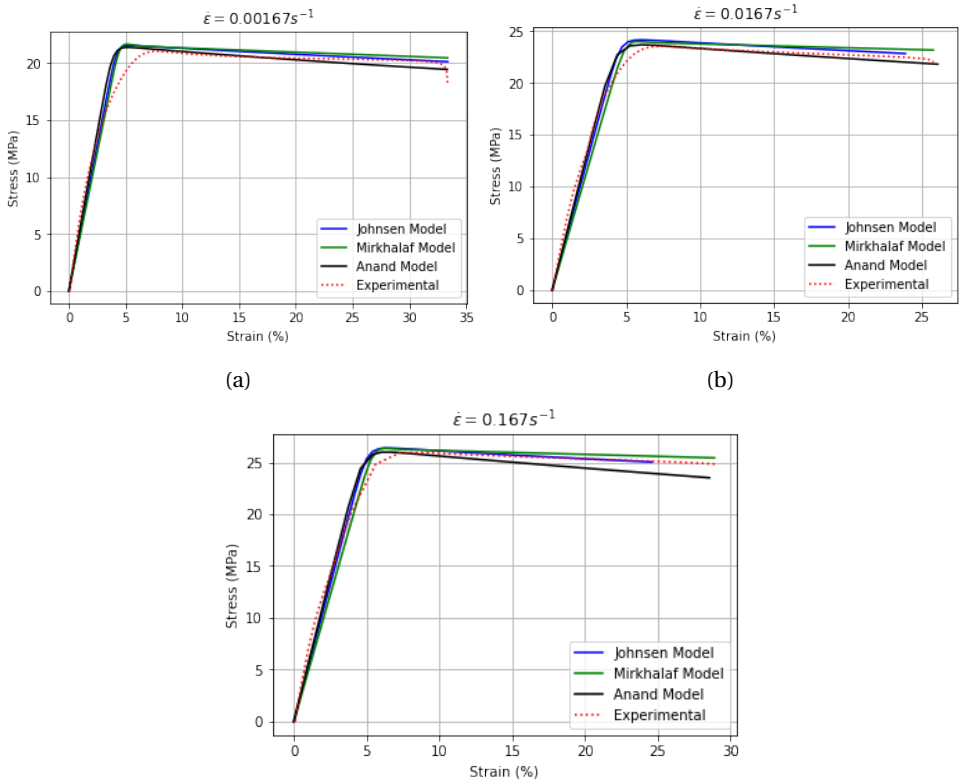

(a) (b)

(c)

Figure 3.7: Comparison of the experimental and simulation results of PCR-PP at T = 296 K. Curves at $\dot{\epsilon} = 0.00167\ s^{-1}$ are used for calibration.

Table 3.5: Mean square errors of PCR-PP at T = 296 K

Model	$\dot{\epsilon} = 1.667 * 10^{-3}\ s^{-1}$	$\dot{\epsilon} = 1.667 * 10^{-2}\ s^{-1}$	$\dot{\epsilon} = 0.1667\ s^{-1}$
Johnsen Model	0.58	0.69	1.12
Mirkhalaf Model	0.612	1.16	1.47
Anand Model	0.606	0.31	2.05

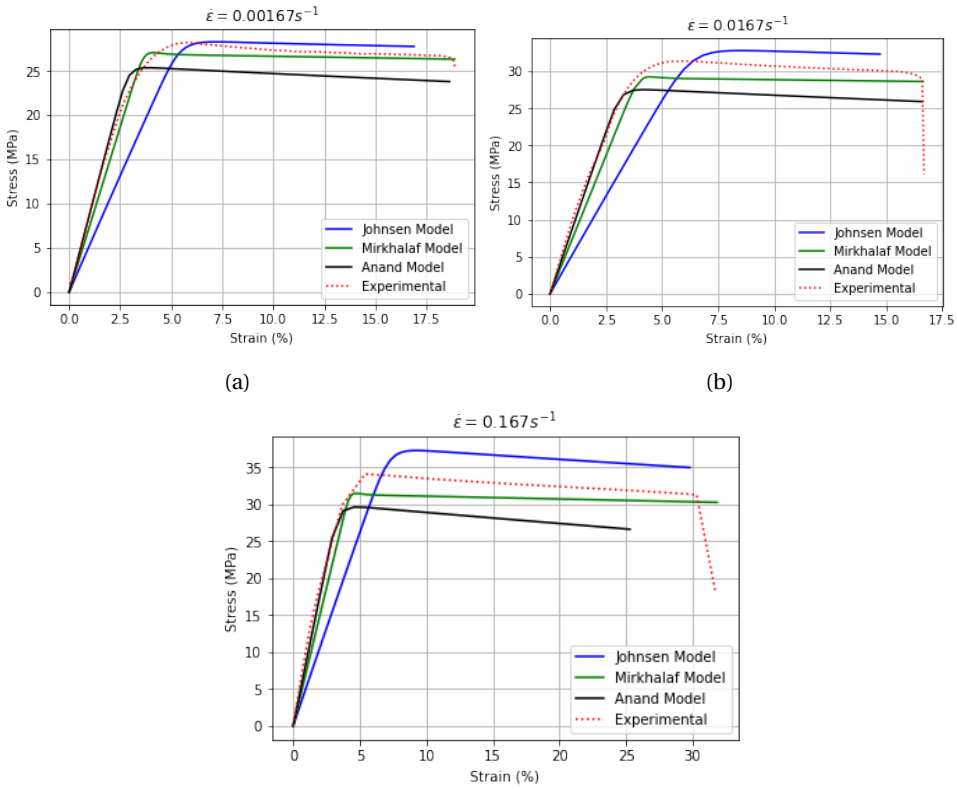

Figure 3.8: Comparison of Experimental and simulation results of PCR-PP at T = 273 K

Table 3.6: Mean square errors of PCR-PP at T = 273 K

Model	$\dot{\epsilon} = 1.667 * 10^{-3}\ s^{-1}$	$\dot{\epsilon} = 1.667 * 10^{-2}\ s^{-1}$	$\dot{\epsilon} = 0.1667\ s^{-1}$
Johnsen Model	7.905	16.77	18.84
Mirkhalaf Model	2.36	9.76	10.76
Anand Model	5.11	3.54	15.89

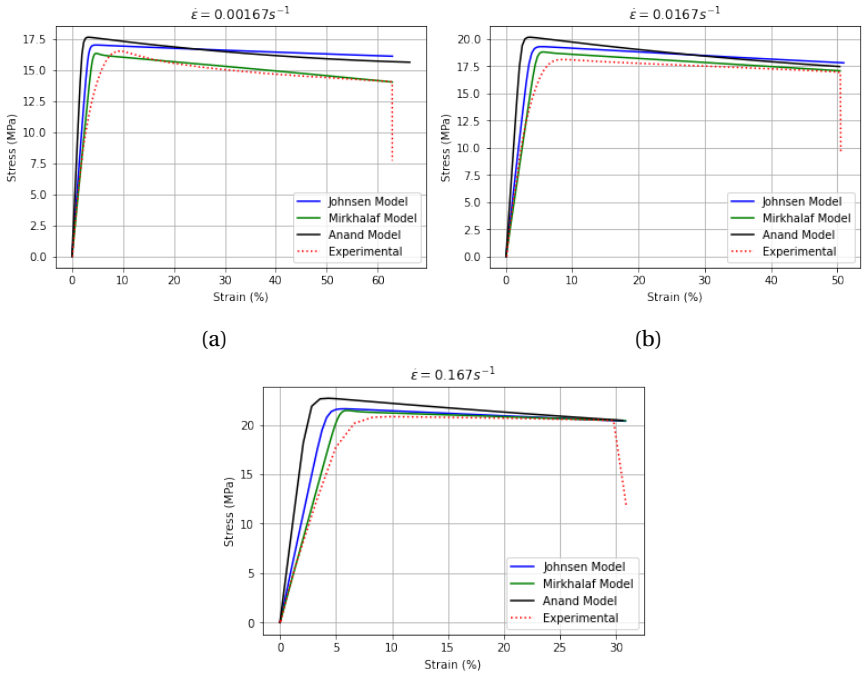

Figure 3.9: Comparison of experimental and simulation results of PCR-PP at T = 319 K

Table 3.7: Mean square errors of PCR-PP at T = 319 K

Model	$\dot{\epsilon} = 1.667 * 10^{-3}\ s^{-1}$	$\dot{\epsilon} = 1.667 * 10^{-2}\ s^{-1}$	$\dot{\epsilon} = 0.1667\ s^{-1}$
Johnsen Model	3.13	1.71	2.12
Mirkhalaf Model	0.32	0.34	1.94
Anand Model	4.38	4.88	3.96

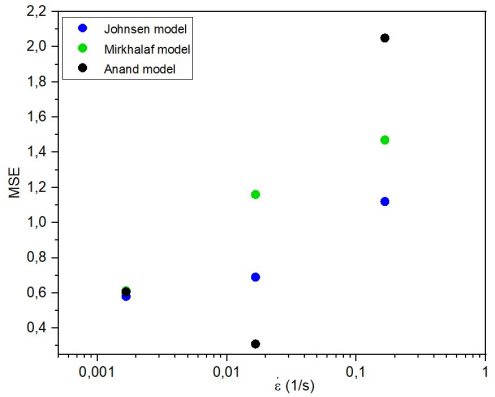

(a) T = 296 K

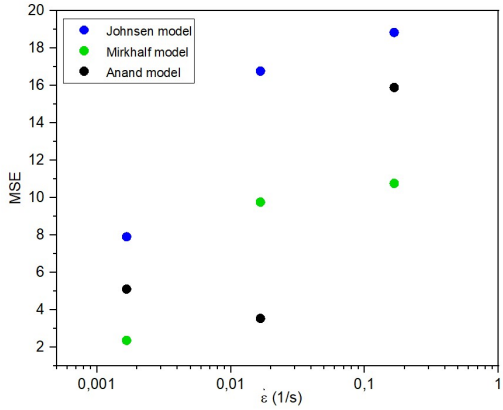

(b) T = 273 K

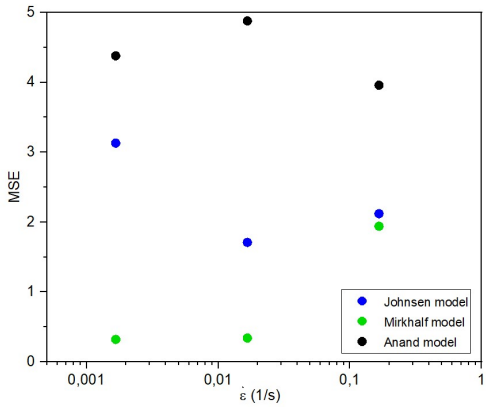

(c) T = 319 K

Figure 3.10: Comparison of Mean square error values of PCR-PP for different models

The uniaxial tensile test simulations are performed at strain rates $\dot{\epsilon} = 1.667 * 10^{-3}$, $1.667 * 10^{-2}$, 0.1667 at temperatures T = 273 K, 296 K and T = 319 K. The corresponding simulation results are presented in figures 3.7, 3.8 and 3.9 and the parameters employed in the simulations are shown in Table 5.1. From figure 3.7 it is observed that all three models accurately capture material behavior at room temperature (T = 296 K) at three strain rates. From figure 3.8 it is seen that the model's capability to capture the real material behavior diminishes when the temperature T = 273 K and at a high strain rate. The exponential relation of the shear modulus (G) considered by Johnsen et al. [1] cannot predict elastic behavior accurately. This inaccuracy is also observed by Johnsen et al. [1]. The slopes of strain hardening is accurately predicted over all temperatures and strain rates. At temperature T = 319 K, the models overestimated the yield stress, as the viscoelastic effects are ignored in the models. However, the model developed by Mirkhalaf et al. [2] captures the overall behavior accurately at T = 319 K. From the mean square error val-

ues, it is concluded that among the three models considered, the model developed by Mirkhalaf et al. [2] predicts the real material behavior of PCR-PP accurately.

CONCLUDING REMARKS

In this chapter, the mechanical response of PCR-PP is analyzed using the elasto-viscoplastic models developed by Johnsen et al. [1], Mirkhalaf et al. [2], and Anand et al. [3] through tensile tests. The Bayesian optimization technique is used to calibrate the material properties of PCR-PP. The simulation results show that Mirkhalaf model predicts the behavior accurately compared to other models. In comparison, the Mirkhalaf model takes less computational time. The Johnsen model takes large computational time as the Jacobian is calculated numerically. The numerical implementation of the stiffness matrix is discussed in appendix A.

4

THERMO VISCOPLASTIC ANALYSIS OF PCR-PE

In he current chapter, PCR-PE's mechanical response was examined under tensile tests. The present investigation is particularly focused on two finite strain thermo-elasto-viscoplastic constitutive models, [2] and [3]. The experimental results shown in figure 4.1, the PCR-PE exhibits strain softening behaviour and failure strain is 1100%. As the Johnsen model does not consider the effect of strain softening in the model, it is ignored. The Bayesian optimization approach presented in chapter 3 is used to calibrate the material parameters. With the optimal set of parameters obtained, the stress-strain response of PCR-PE is predicted for three different temperatures and strain rates. The results obtained are compared with the experimental results. To analyse the predictive capabilities of the model under different stress triaxiaties, the simulations are made for round notch specimens with different radius of curvature and results obtained are compared with the experimental results made by Hachour et al [73].

4.1. EXPERIMENTAL RESULTS

In this study, similar to PCR-PP uniaxial tension tests of PCR-PE were performed at three temperatures (T = 273 K, T = 296 K and T = 319 K) and three different cross-head velocities (v = 2 mm/min, v = 20 mm/min and v = 200 mm/min).

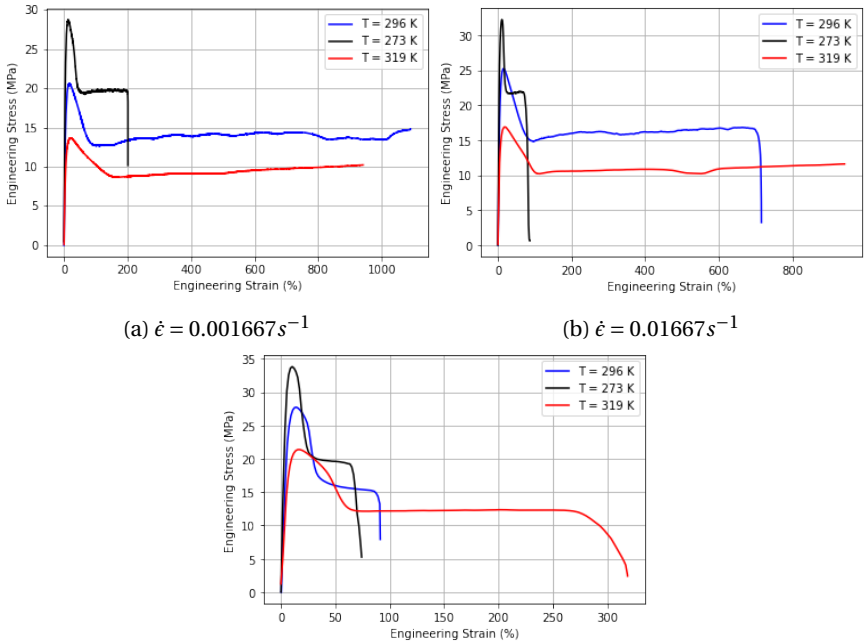

(a) $\dot{\epsilon} = 0.001667 s^{-1}$ (b) $\dot{\epsilon} = 0.01667 s^{-1}$

(c) $\dot{\epsilon} = 0.1667 s^{-1}$

Figure 4.1: Uni-axial tensile test results of PCR-PE

The stress-strain behaviour of PCR-PE (QCP 5603) reported in 4.1. The experimental results shows that an increase in temperature has a similar impact on Young's modulus and the flow stress as a decrease in strain rate. The increase of temperature results in decrease of yield stress and young's modulus. Unlike to PCR-PP, the PCR-PE exhibits the strain softening (necking) behaviour after yield stress. The reduction in stress value is different for different temperatures and strain rates. The consequence of necking is that necking region tends to elongate, and value of engineering stress is constant.

4.2. Modification of Anand model: update of Orientational Hardening of Polymers

Boyce et al. [24], Gissen et al. [74], Anand et al. [75], Johnsen et al. [1], and many other models assumed that to model the stress rise due to locking and stretching of polymers at high strains, polymers behave like rubber and used entropic-network models. In the Anand model, a Gent theory [76] has been employed to capture stress increase at large strains. On analyzing the PCR-PE stress-strain behavior using the Anand model, it is found that the model works for the strain up to 700 %. Later the model exhibits convergence issues. From the experimental results, it is observed that PCR-PE has a failure strain greater than 1100 %. The Gent theory employed in the Anand model-derived the strain energy equation assuming that each molecule segment between successive points

of cross-linkage is considered as Gaussian chain. The commonly used Arruda Boyce hardening model makes a different assumption as shown in figure 4.2. At large strains, Arruda Boyce model considers that each molecule segment between successive points of crosslinking is a non-Gaussian chain. The free energy is derived from the non-Gaussian probability distribution.

Therefore, the orientational hardening of the material due to the alignment of the polymer chains is captured by the eight chain model [25].

$$\rho\Psi = \frac{\kappa}{2}(\ln(J))^2 - 3\kappa\alpha_T \ln(J)(T - T_0) + \mu_B(T)\lambda_{lock}^2\left[\left(\frac{\lambda}{\lambda_{lock}}\right)\xi + \ln\left(\frac{\xi}{\sinh\xi}\right)\right] \tag{4.1}$$

where

$$\mu_B = \mu_{B,ref}\frac{T}{T_{ref}} \tag{4.2}$$

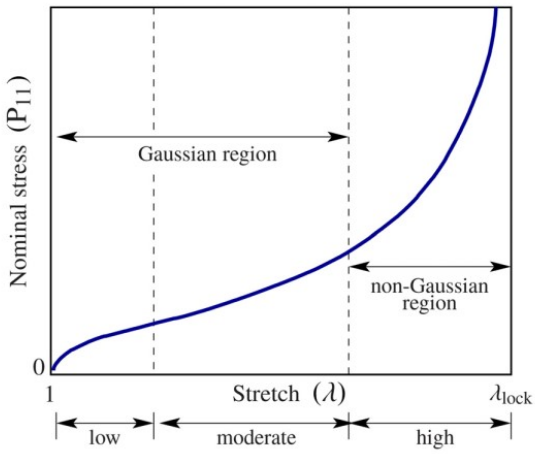

Figure 4.2: Typical stress–stretch relationship for an elastomer [77]

To implement Arruda Boyce eight chain model, the $\sigma^{(2)}$ term in the equation (2.109) is replaced as

$$\sigma^{(2)} = \frac{1}{J}\left[\frac{\mu_B(T)\lambda_{lock}}{3\overline{\lambda}_{c,n+1}}L^{-1}\left(\frac{\overline{\lambda}_{c,n+1}}{\lambda_{lock}}\right)B_{D,n+1} - \kappa_B \ln(J_{n+1}I - 3\kappa_B\alpha(T_n - T_0)I\right] \tag{4.3}$$

The simulation results of the modified Anand model with Arruda-Boyce eight-chain hardening law in comparison with the experimental results are shown in the next sections.

4.3. CALIBRATION OF MATERIAL MODEL

The same procedure mentioned in the previous chapter is used to calibrate the material properties of PCR-PE. The shear modulus temperature sentivity parameters and Eyring's flow stress parameters are calibrated using equations 3.1 and 3.6 respectively. The temperature dependence of Young's modulus and yield stress are shown in figure 4.3.The material properties of PCR-PE after calibration are mentioned in table 4.2 and 4.3.

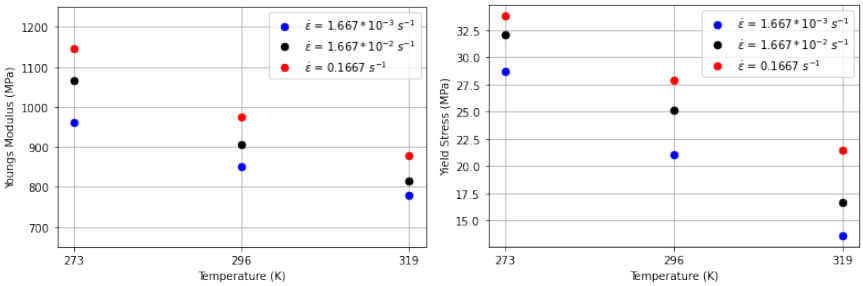

(a) Young's Modulus (b) Yield stress

Figure 4.3: Temperature and strain rate dependence of Young's modulus and Yield stress PCR-PE

Table 4.1: Temperature sensitivity parameters of Elastic properties after optimization

Material model	Properties	Units	Bounds of parameters	Values
Mirkhalaf model	a	(-)	[-1, 0]	-0,00462
	b	K^{-1}	[1, 6]	2.3823
Anand model	M	K^{-1}	[1, 5]	1.363

Table 4.2: Material Properties of PCR-PE after calibration of Mirkhalaf model

	Properties	Units	Bounds of parameters	PCR-PE
Elastic	E	MPa	(-)	950
	ν	(-)	(-)	0.43
Yield stress	ΔH	J/mol	$[10^5,\ 4 * 10^5]$	191817
	A_0	s^{-1}	$[10^{-29},\ 10^{-25}]$	$5.19 * 10^{-26}$
	V	m^3/mol	$[10^{-4},\ 10^{-2}]$	0.00248
	ω	m^3/mol	$[10^{-5},\ 10^{-3}]$	0.00062
Softening	h	(-)	[50, 150]	52.18
	$D_{\infty,0}$	(-)	[3, 7]	5.387
Hardening	H	MPa	[0.0001, 0.0008]	0.0001

Table 4.3: Material Properties of PCR-PE considered for Anand Model with Arruda Boyce Orientational Hardening after optimization

	Properties	Units	Bounds of parameters	PCR-PE
Elastic	T_g	K	(-)	173
	ρ	Kg/m^3	(-)	930
	α	K^{-1}	(-)	$7*10^{-5}$
	G_0	MPa	(-)	469
	M	$MPa\,K^{-1}$	(-)	1.363
	ν_{poi}	(-)	(-)	0.42
Back stress	X	$MPa\,K^{-1}$	(-)	0.0017
	γ	(-)	(-)	6.92
Yield stress	α_p	(-)	[0.2, 0.8]	0.534
	ν_0	s^{-1}	$[10^{15}, 10^{20}]$	$5.27*10^{17}$
	m	(-)	[0.1, 0.5]	0.32207
	Q	J	$[10^{-23}, 10^{-18}]$	$2.186*10^{-19}$
	V	m^3	$[10^{-33}, 10^{-25}]$	$1.936*10^{-27}$
Softening	h_1	(-)	[13, 17]	15.1
	b	MPa	[650, 800]	690.41
	g_1	(-)	[0.4, 1]	0.504
	g_2	K^{-1}	(-)	0
	ϕ_r	(-)	(-)	0.00072
	k	K	[-0.5, -0.3]	-0.45
	r	(-)	[0.25, 0.45]	0.256
	s	(-)	(-)	0.03
	ν_r	s^{-1}	(-)	0.00288
	n	(-)	(-)	1.6
	h_2	(-)	(-)	0.39
	l_1	MPa	[300, 400]	325.39
	l_2	$MPa\,K^{-1}$	[0.5, 1.1]	0.869
Hardening	$\mu_{B,ref}$	MPa	[0.1, 0.3]	0.11
	κ_B	MPa	[8000, 9000]	8532
	λ_{lock}	(-)	[7, 10]	9.14
thermal	c_0	$J\,Kg^{-1}\,K^{-1}$	(-)	3546
	c_1	$J\,Kg^{-1}\,K^{-2}$	(-)	0
	κ_0	$Watt\,m^{-1}\,K^{-1}$	(-)	0.46
	κ_1	(-)	(-)	0
	ω	(-)	(-)	0.8

4.4. RESULTS

4.4.1. TENSILE TESTS

The comparison of the numerical and experimental results are presented in the following section. Similar to PCR-PP, nine different configurations of temperature and strain rates were investigated in total: three temperatures 296 K, 273 K and 319 K and for each

temperature three nominal strain rates of $1.667 * 10^{-3}\ s^{-1}$, $1.667 * 10^{-2}\ s^{-1}$ and 0.1667 s^{-1}. From the work of Mirkhalaf et al. [2] it is observed that D_∞ is highly dependent on temperature. The temperature dependence relation of D_∞ is calculated and the relation is $D_\infty = D_{\infty,0}(0.01699T + 5.9771)$.

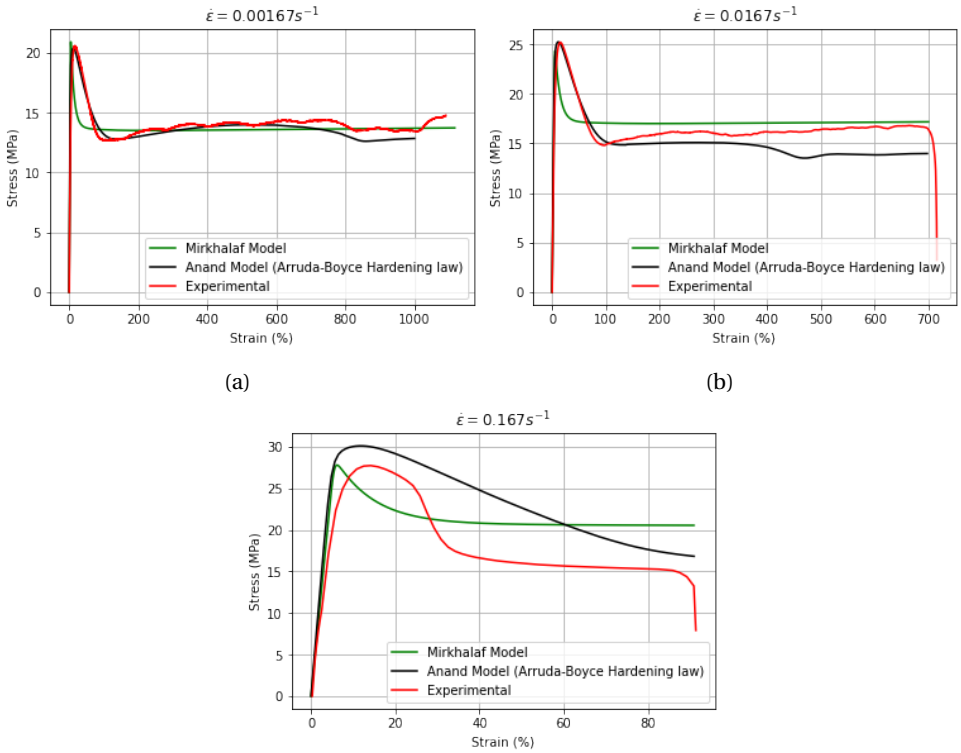

Figure 4.4: Comparison of Experimental and simulation results of PCR-PE at T = 296 K. Curves at $\dot{\epsilon} = 0.00167\ s^{-1}$ are used for calibration.

Table 4.4: Mean square error values of PCR-PE at T = 296 K

Model	$\dot{\epsilon} = 1.667 * 10^{-3}\ s^{-1}$	$\dot{\epsilon} = 1.667 * 10^{-2}\ s^{-1}$	$\dot{\epsilon} = 0.1667\ s^{-1}$
Mirkhalaf Model	5.25	5.38	11.1
Anand Model(Arruda -Boyce Hardening Model)	0.4	3.41	14.26

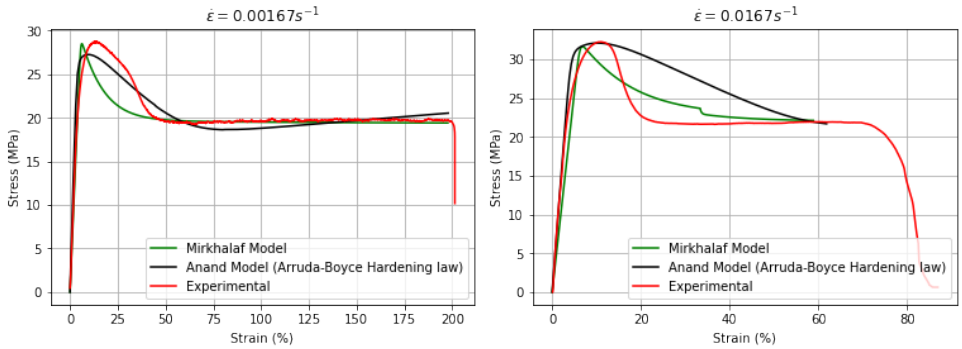

(a)

(b)

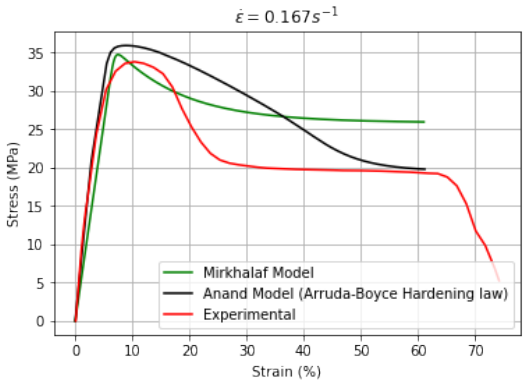

(c)

Figure 4.5: Comparison of Experimental and simulation results of PCR-PE at T = 273 K

Table 4.5: Mean square error values of PCR-PE at T = 273 K

Model	$\dot{\epsilon} = 1.667 * 10^{-3}\ s^{-1}$	$\dot{\epsilon} = 1.667 * 10^{-2}\ s^{-1}$	$\dot{\epsilon} = 0.1667\ s^{-1}$
Mirkhalaf Model	4.95	4.44	17.37
Anand Model(Arruda -Boyce Hardening Model)	0.83	17.679	18.21

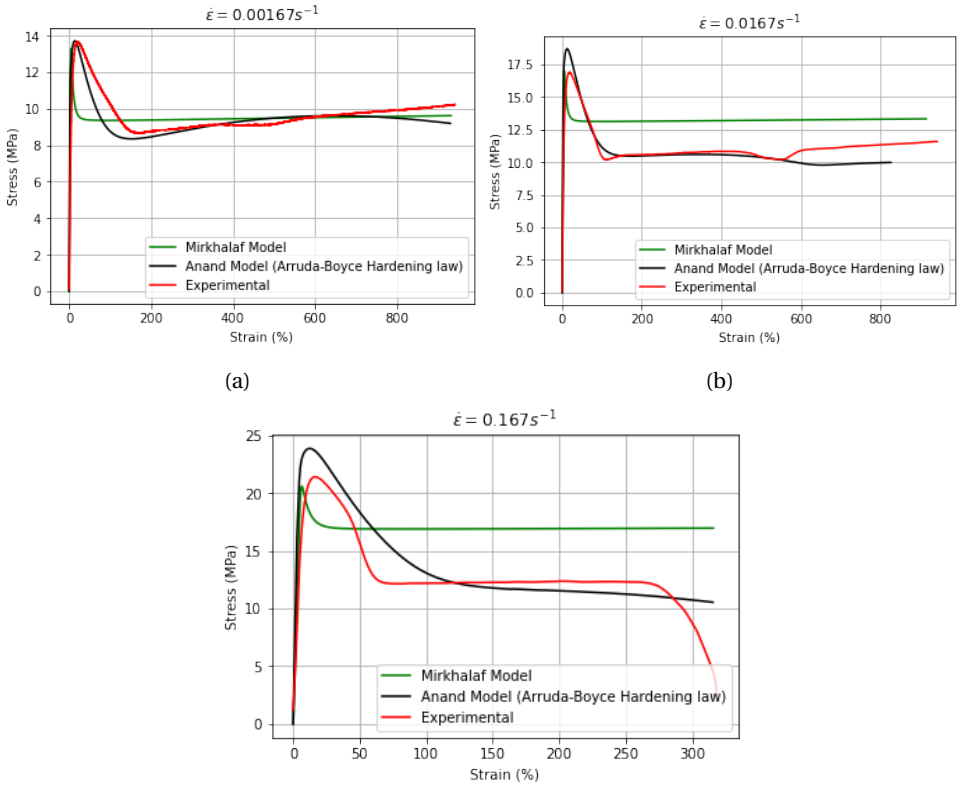

Figure 4.6: Comparison of Experimental and simulation results of PCR-PE at T = 319 K

Table 4.6: Mean square error values of PCR-PE at T = 319 K

Model	$\dot{\epsilon} = 1.667 * 10^{-3}\ s^{-1}$	$\dot{\epsilon} = 1.667 * 10^{-2}\ s^{-1}$	$\dot{\epsilon} = 0.1667\ s^{-1}$
Mirkhalaf Model	1.347	5.8	9.45
Anand Model(Arruda -Boyce Hardening Model)	0.82	1.2	3.2

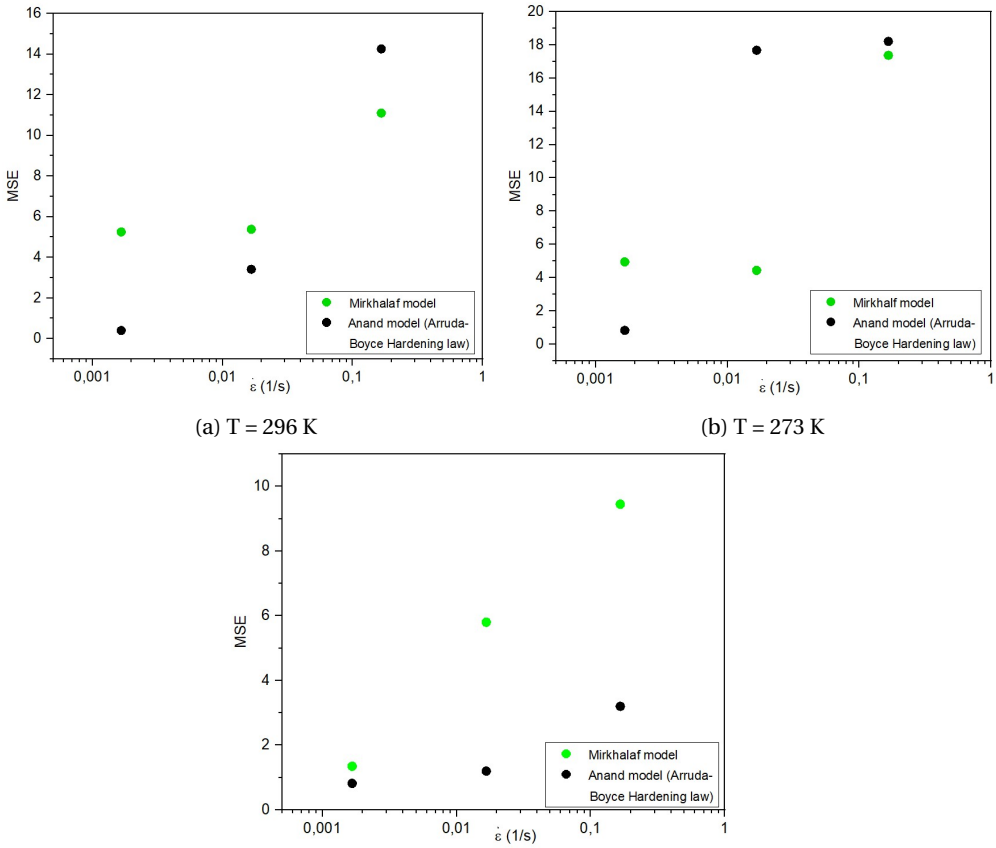

(a) T = 296 K

(b) T = 273 K

(c) T = 319 K

Figure 4.7: Comparison of Mean square error values of PCR-PE for different models

Similar to PCR-PP, the uniaxial tensile test simulations of PCR-PE are conducted at strain rates $\dot{\epsilon} = 1.667 * 10^{-3}$, $1.667 * 10^{-2}$, 0.1667 at the temperatures T = 273 K, 296K and T = 319 K. The corresponding simulation results are presented in figures 4.4, 4.5 and 4.6 and the parameters employed in the simulations are shown in Table 4.2 and 4.3. The simulation shows that the capability of two models to capture the stress-strain behavior diminishes when the strain rate is increased. The simulation results from the Mirkhalaf model show that the stress drop takes place abruptly. Note that the saturation value of the softening parameter (D_∞) that captures the stress drop only depends on temperature in the model. However, from the experimental results it can be observed that D_∞ is also strain rate dependent, which explains the stress drop is not captured properly. The simulation results obtained from the Anand model capture the post yield response of the material accurately at low strain rates for different temperatures. Though the Anand model accurately captures the stress drop and strain hardening behavior at high strain rates, the

model fails to capture softening region accurately for those conditions. Overall the comparison of simulation and experimental results shows that the Anand model captures the real material behavior of PCR-PE accurately compared to the Mirkhalaf model.

4.4.2. TRIAXIALITY TESTS

In the previous section, the convention mechanical loading experiment such as tensile test results are investigated using both experiments and simulations. It is also very important to analyse the predictive capabilities of the model under different numerical examples such as round notch specimens, when the multiaxial stress state is observed. The multiaxial stress state is quantified using stress triaxiality ratio (T) defined as ratio of hydrostatic stress (σ_h) and von-mises equivalent stress (σ_{eq}).

$$T = \frac{\sigma_h}{\sigma_{eq}} \tag{4.4}$$

where σ_h and σ_{eq} defined in terms of principal stresses are

$$\sigma_h = \frac{1}{3}(\sigma_1 + \sigma_2 + \sigma_3) \tag{4.5}$$

$$\sigma_{eq} = \frac{1}{2}\left((\sigma_1 - \sigma_2)^2 + (\sigma_1 - \sigma_3)^2 + (\sigma_3 - \sigma_2)^2\right)^{\frac{1}{2}} \tag{4.6}$$

At the center of the median cross-section the stress triaxiality ratio T was determined using the Bridgman formula [78]:

$$T = \frac{1}{3} + \ln\left(1 + \frac{D}{4R_c}\right) \tag{4.7}$$

where D is diameter and R_c is radius of curvature. Experimental results for HDPE under four different radius of curvatures R80, R10, R4 and R2 are taken from Hachour et al [43]. The dimensions of the round notch specimens used in the simulations are shown in the figure 4.8.

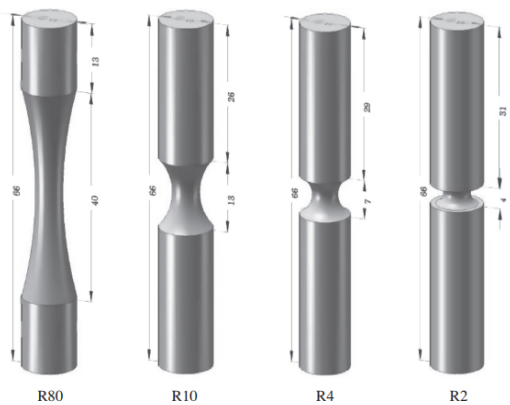

Figure 4.8: Dimensions of notched round specimens [43]

The stress triaxiality ratio values for four different curvatures calculated using the Bridgman formula are shown in table 4.7.

Table 4.7: Stress triaxiality ratio

radius of curvature (mm)	Stress triaxilty ratio
80	0.33
10	0.44
4	0.6
2	0.8

The calibration of the material properties of the notch specimens is performed using the procedure mentioned in chapter 3 for the test case of R80 specimen and the stress strain curves of the remaining triaxiality cases are predicted. The properties of calibrated materials are shown in Table 4.8 - 4.10.

Table 4.8: Material Properties of HDPE after calibration of Johnsen model

	Properties	Units	Bounds of parameters	HDPE
Elastic	G	MPa	(-)	320
	a_A	K^{-1}	(-)	0
Yield stress	ΔH_α	KJ/mol	[180, 230]	221.0683
	V_α	nm^3	[3, 7]	4.38
	$\dot{p}_{0,\alpha}$	s^{-1}	$[1*10^{27}, 3*10^{27}]$	$1.51*10^{27}$
	ΔH_β	KJ/mol	[190, 240]	201.351
	V_β	nm^3	[3, 7]	3.747
	$\dot{p}_{0,\beta}$	s^{-1}	$[5*10^{38}, 6*10^{38}]$	$5.05*10^{38}$
Hardening	b_α	(-)	[6, 10]	9.912
	b_β	(-)	[11.5, 15]	11.898
	$\mu_{B,ref}$	MPa	[0.1,1]	0.311
	κ_B	MPa	[2200, 2750]	2492.78
	λ_{lock}	(-)	[3, 5]	3.403

Table 4.9: Material Properties of HDPE after calibration of Mirkhalaf model

	Properties	Units	Bounds of parameters	HDPE
Elastic	E	MPa	(-)	910
	ν	(-)	(-)	0.43
Yield stress	ΔH	J/mol	$[10^5,\ 4*10^5]$	195554.7
	A_0	s^{-1}	$[10^{-29},\ 10^{-25}]$	$3.88*10^{-26}$
	V	m^3/mol	$[10^{-4},\ 10^{-2}]$	0.00248
	ω	m^3/mol	$[10^{-5},\ 10^{-3}]$	0.00062
Softening	h	(-)	[50, 150]	80.11
	$D_{\infty,0}$	(-)	[0.1, 1.5]	0.41
Hardening	H	MPa	[8, 16]	12.85

Table 4.10: Material Properties of HDPE after calibration of Anand model

	Properties	Units	Bounds of parameters	PCR-PP
Elastic	T_g	K	(-)	173
	ρ	Kg/m^3	(-)	1000
	α	K^{-1}	(-)	$7*10^{-5}$
	G_0	MPa	(-)	320
	M	$MPa\,K^{-1}$	(-)	0
	ν_{poi}	(-)	(-)	0.43
Back stress	X	$MPa\,K^{-1}$	(-)	0
	γ	(-)	(-)	0
Yield stress	α_p	(-)	[0.3, 0.75]	0.228
	ν_0	s^{-1}	$[1*10^{17}, 1*10^{21}]$	$5.67*10^{19}$
	m	(-)	[0.3, 0.5]	0.458
	Q	J	$[1*10^{-21}, 1*10^{-18}]$	$7.24*10^{-19}$
	V	m^3	$[1*10^{-27}, 1*10^{-25}]$	$3.702*10^{-27}$
Softening	h_1	(-)	(-)	0
	b	MPa	(-)	0
	g_1	(-)	(-)	0
	g_2	K^{-1}	(-)	0
	ϕ_r	(-)	(-)	0
	k	K	(-)	-0.16
	r	(-)	(-)	0
	s	(-)	(-)	0
	ν_r	s^{-1}	(-)	0
	n	(-)	(-)	0
	h_2	(-)	(-)	0
	l_1	MPa	(-)	0
	l_2	$MPa\,K^{-1}$	(-)	0
Hardening	$\mu_{B,ref}$	MPa	[0.5, 2.5]	1.15
	κ_B	$MPa\,K^{-1}$	[2000, 3000]	2498.3
	λ_{Lock}	(-)	[2, 65]	3.05
Thermal	c_0	$J\,Kg^{-1}\,K^{-1}$	(-)	3546
	c_1	$J\,Kg^{-1}\,K^{-2}$	(-)	0
	κ_0	$Watt\,m^{-1}\,K^{-1}$	(-)	0.19
	κ_1	(-)	(-)	0
	ω	(-)	(-)	0.8

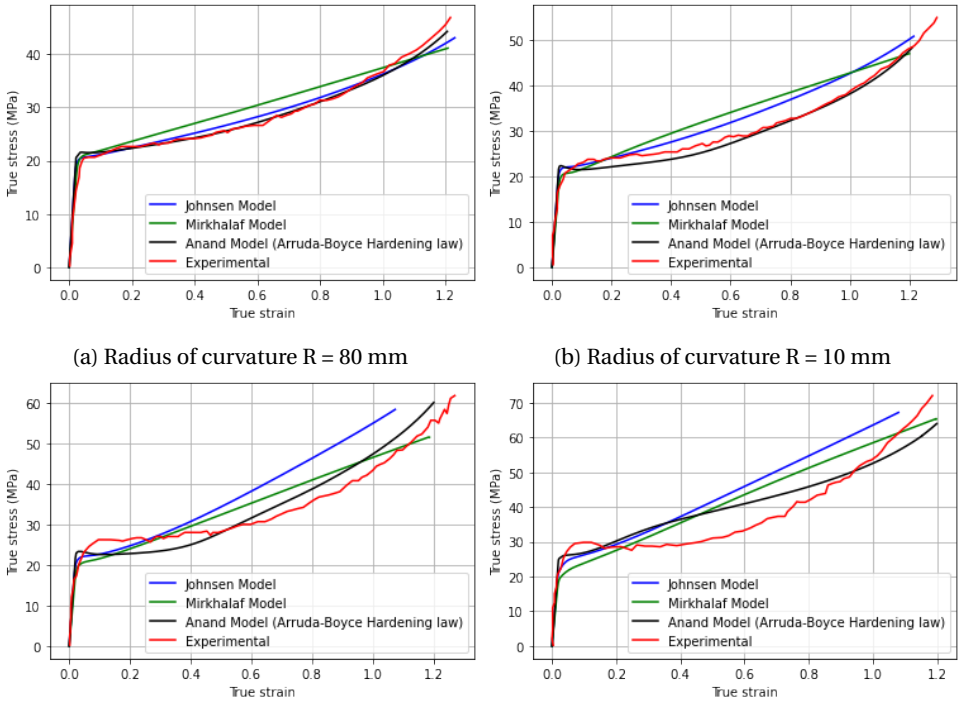

(a) Radius of curvature R = 80 mm

(b) Radius of curvature R = 10 mm

(c) Radius of curvature R = 4 mm

(d) Radius of curvature R = 2 mm

Figure 4.9: Comparison of Experimental and simulation results of round notch specimens. Curves at R = 80 mm are considered for calibration.

The experimental results show that the yield stress and strain hardening slope increases as the specimens' radius decreases. The comparison of experimental and simulation results shows that the accuracy of the models diminishes as the stress triaxiality ratio increases. The model Mirkhalaf et al. [2] developed cannot accurately capture the strain hardening region, as linear hardening law is considered to capture the hardening behavior. The Johnsen model over-predicted the stress values in the strain hardening region. Anand model can accurately capture HDPE's stress-strain behavior at low values of stress triaxilties. However, the deviations are large at high triaxility ratios.

5

Conclusion

THIS chapter summarises the achievements and limitations, and then provides suggestions on potential improvements.

5.1. Conclusion

The main objective of the present work is to understand the mechanical performance of the PCR-PP and PCR-PE. The tensile test results of PCR-PP and PCR-PE shows temperature and strain rate dependent yield stress followed by strain hardening. After reviewing the state of the art polymer constitutive models, three plasticity models developed by Johnsen et al. [1], Mirkhalaf et al. [2], and Anand et al. [3]) are identified and implemented to assess if they could capture the intrinsic features of the macroscopic stress–strain response of these polymers. The models were calibrated using the Bayesian optimization, and then finite element analysis of tensile tests under different loading conditions are performed aiming at assessing the predictive ability of three constitutive models.

PCR-PP's experimental and simulation results are in good agreement for different temperatures and strain rates, especially when considering the model developed by Mirkhalaf et al. [2] because it does not have a noticeable softening region after yielding.

However, tensile test results of PCR-PE shows formation of necking after yield stress. The models developed by Mirkhlaf et al. [2] and Anand et al. [3] are considered to predict the behaviour of PCR-PE. Anand model exhibited some convergence issues for large deformations greater than 700 % engineering strain. To overcome this limitation, the orientational hardening law was modified with Arruda Boyce eight chain model. The comparison of experimental and simulation results shows that both the models have limitations in accurately predicting the behavior. However, the modified Anand model is able to predict the behaviour accurately at small strain rates and high temperatures.

In addition, the predictive capabilities of the constitutive models under multi-axial load-

ing were also investigated. In order to investigate the behaviour and implementation robustness of the constitutive models, numerical results obtained from Johnsen et al. [1], Mirkhalaf et al. [2] and modified Anand model for different stress triaxilty ratios are compared with the experimental results obtained by Hachour et al. [73]. The simulation results obtained from Anand model with Arruda Boyce hardening law are in good agreement with experimental results for four tri-axility ratios.

Current work has following limitations:

1. The three models considered are developed to analyze the mechanical behaviour of pure thermoplastics, so they do not consider the effect of the number of recycling cycles on material properties.
2. The considered models do not account for viscoelastic behaviour of polymers.
3. The model developed by Johnsen et al. [1] does not consider the effect of pressure and strain softening of polymers.
4. The model developed by Mirkhalaf et al. [2] considers linear hardening law, which limits capturing the true stress-true strain curves accurately for different stress triaxiality ratios. The model also does not consider the effect of self-heating due to plastic dissipation.
5. Bayesian optimization is efficient in tuning few hyper-parameters but its efficiency degrades a lot when the search dimension increases.

5.2. FUTURE RESEARCH

Although the constitutive modeling goals defined in the present work are achieved, there are several relevant aspects that can be addressed in future research. These are stated below together with some brief comments:

1. **Effect of recycling.** The models can be extended considering the effects of recycling cycles and inclusions.
2. **Experimental validation.** critical comparison with the numerical results over different loading cases such as bi-axial loading with butterfly specimen would strengthen the assessment of models.
3. **Viscoelastic behaviour.** The models' accuracy can undoubtedly be enhanced by accounting for the viscoelastic behaviour characteristic of polymers, improving the prediction of the material behaviour prior to the yield point.

References

[1] J. Johnsen, A. H. Clausen, F. Grytten, A. Benallal, and O. S. Hopperstad, *A thermo-elasto-viscoplastic constitutive model for polymers,* Journal of the Mechanics and Physics of Solids **124**, 681 (2019).

[2] S. M. Mirkhalaf, F. M. A. Pires, and R. Simoes, *An elasto-viscoplastic constitutive model for polymers at finite strains: Formulation and computational aspects,* Computers and Structures **166**, 60 (2016).

[3] N. M. Ames, V. Srivastava, S. A. Chester, and L. Anand, *A thermo-mechanically coupled theory for large deformations of amorphous polymers. part ii: Applications,* International Journal of Plasticity **25**, 1495 (2009).

[4] J. M. Eagan, J. Xu, R. Di Girolamo, C. M. Thurber, C. W. Macosko, A. M. LaPointe, F. S. Bates, and G. W. Coates, *Combining polyethylene and polypropylene: Enhanced performance with pe/i pp multiblock polymers,* Science **355**, 814 (2017).

[5] A. K. V. D. Vegt, *From polymers to plastics,* (2002).

[6] M. Rubinstein and R. Colby, *Polymer Physics* (Oxford University Press, 2003).

[7] *Structure of polymers,* in *Mechanical Properties of Solid Polymers* (John Wiley Sons, Ltd, 2012) Chap. 1, pp. 1–18, https://onlinelibrary.wiley.com/doi/pdf/10.1002/9781119967125.ch1 .

[8] P. Hiemenz and T. Lodge, *Polymer Chemistry, Second Edition* (Taylor & Francis, 2007).

[9] W. Callister and D. Rethwisch, *Materials Science and Engineering* (Wiley, 2014).

[10] O. A. Hasan and M. C. Boyce, *Energy storage during inelastic deformation of glassy polymers,* .

[11] M. B. Joachim Roesler, Harald Harders, *Mechanical Behaviour of Engineering Materials* (Springer, Berlin, Heidelberg, 2007).

[12] *Relaxation transitions: Experimental behaviour and molecular interpretation,* in *Mechanical Properties of Solid Polymers* (John Wiley Sons, Ltd, 2012) Chap. 10, pp. 261–284, https://onlinelibrary.wiley.com/doi/pdf/10.1002/9781119967125.ch10 .

[13] *Yielding and instability in polymers,* in *Mechanical Properties of Solid Polymers* (John Wiley Sons, Ltd, 2012) Chap. 12, pp. 319–378, https://onlinelibrary.wiley.com/doi/pdf/10.1002/9781119967125.ch12 .

[14] R. Ilyas, S. Sapuan, and E. Bayraktar, *Recycling of Plastics, Metals, and Their Composites*, Emerging Materials and Technologies (CRC Press, 2021).

[15] J. Aurrekoetxea, M. Sarrionandia, I. Urrutibeascoa, and M. L. Maspoch, *Effects of recycling on the microstructure and the mechanical properties of isotactic polypropylene,* Journal of materials science **36**, 2607 (2001).

[16] H. M. da Costa, V. D. Ramos, and M. C. Rocha, *Rheological properties of polypropylene during multiple extrusion,* Polymer Testing **24**, 86 (2005).

[17] N. Bahlouli, D. Pessey, C. Raveyre, J. Guillet, S. Ahzi, A. Dahoun, and J. M. Hiver, *Recycling effects on the rheological and thermomechanical properties of polypropylene-based composites,* Materials & Design **33**, 451 (2012).

[18] E. A. De, S. Neto, P. Peri´c, D. Owen, and A. J. Wiley, *Computational methods for plasticity theory and applications,* .

[19] E. de Souza Neto, D. Peric, and D. Owen, *Computational Methods for Plasticity: Theory and Applications* (Wiley, 2011).

[20] H. Eyring, *Viscosity, plasticity, and diffusion as examples of absolute reaction rates,* The Journal of chemical physics **4**, 283 (1936).

[21] A. Cross and R. N. Haward, *Orientation hardening of pvc,* (1978).

[22] A. Argon, *A theory for the low-temperature plastic deformation of glassy polymers,* Philosophical Magazine **28**, 839 (1973).

[23] A. S. A. Mary C. BOYCE, David M. PARKS, *1987, large inelastic deformation of glassy polymers. rate dependent constitutive model,* .

[24] M. C. Boyce, D. M. Parks, and A. S. Argon, *Large inelastic deformation of glassy polymers. part i: rate dependent constitutive model,* Mechanics of materials **7**, 15 (1988).

[25] E. M. Arruda and M. C. Boyce, *A three-dimensional constitutive model for the large stretch behavior of rubber elastic materials,* Journal of the Mechanics and Physics of Solids **41**, 389 (1993).

[26] A. I. Leonov, *Institute of mechanical problems,* (1976).

[27] E. P. T. Baaijens, *Calculation of residual stresses in injection molded products,* (1991).

[28] T. A. Tervoort, R. J. M. Smit, W. A. M. Brekelmans, and L. E. Govaert, *A constitutive equation for the elasto-viscoplastic deformation of glassy polymers,* (1998).

[29] P. Timmermans, *Evaluation of a constitutive model for solid polymeric materials : model selection and parameter quantification,* Ph.D. thesis, Mechanical Engineering (1997).

[30] L. Govaert, P. Timmermans, and W. Brekelmans, *The influence of intrinsic strain softening on strain localization in polycarbonate : modeling and experimental validation,* Journal of Engineering Materials and Technology : Transactions of the ASME **122**, 177 (2000).

[31] G. W. Adams and R. J. Farris, *Latent energy of deformation of bisphenol a polycarbonate,* .

[32] M. C. Boyce, E. L. Montagut, and A. S. Argon, *The effects of thermomechanical coupling on the cold drawing process of glassy polymers,* .

[33] S. Hillmansen, . S. Hobeika, R. N. Haward, and P. S. Leeversa, *The effect of strain rate, temperature, and molecular mass on the tensile deformation of polyethylene,* .

[34] S. Hillmansen and R. Haward, *Adiabatic failure in polyethylene,* Polymer **42**, 9301 (2001).

[35] J. Johnsen, F. Grytten, O. S. Hopperstad, and A. H. Clausen, *Influence of strain rate and temperature on the mechanical behaviour of rubber-modified polypropylene and cross-linked polyethylene,* Mechanics of Materials **114**, 40 (2017).

[36] E. M. Arruda, M. C. Boyce, and R. Jayachandran, *Effects of strain rate, temperature and thermomechanical coupling on the finite strain deformation of glassy polymers,* Mechanics of Materials **19**, 193 (1995).

[37] M. Boyce, E. Montagut, and A. Argon, *The effects of thermomechanical coupling on the cold drawing process of glassy polymers,* Polymer Engineering & Science **32**, 1073 (1992).

[38] J. Richeton, S. Ahzi, K. Vecchio, F. Jiang, and A. Makradi, *Modeling and validation of the large deformation inelastic response of amorphous polymers over a wide range of temperatures and strain rates,* International Journal of Solids and Structures **44**, 7938 (2007).

[39] L. Anand, N. M. Ames, V. Srivastava, and S. A. Chester, *A thermo-mechanically coupled theory for large deformations of amorphous polymers. part i: Formulation,* International Journal of Plasticity **25**, 1474 (2009).

[40] V. Srivastava, S. A. Chester, N. M. Ames, and L. Anand, *A thermo-mechanically-coupled large-deformation theory for amorphous polymers in a temperature range which spans their glass transition,* International Journal of Plasticity **26**, 1138 (2010).

[41] D. Garcia-Gonzalez, R. Zaera, and A. Arias, *A hyperelastic-thermoviscoplastic constitutive model for semi-crystalline polymers: Application to peek under dynamic loading conditions,* International Journal of Plasticity **88**, 27 (2017).

[42] M. Polanco-Loria, A. H. Clausen, T. Berstad, and O. S. Hopperstad, *Constitutive model for thermoplastics with structural applications,* International Journal of Impact Engineering **37**, 1207 (2010).

[43] K. Hachour, F. Zaïri, M. Naït-Abdelaziz, J.-M. Gloaguen, M. Aberkane, and J.-M. Lefebvre, *Experiments and modeling of high-crystalline polyethylene yielding under different stress states,* International journal of plasticity **54**, 1 (2014).

[44] C. Popa, R. Fleischhauer, K. Schneider, and M. Kaliske, *Formulation and implementation of a constitutive model for semicrystalline polymers,* International Journal of Plasticity **61**, 128 (2014).

[45] J. P. Manaia, F. A. Pires, A. M. de Jesus, and S. Wu, *Yield behaviour of high-density polyethylene: Experimental and numerical characterization,* Engineering Failure Analysis **97**, 331 (2019).

[46] J. Bergström, S. Kurtz, C. Rimnac, and A. Edidin, *Constitutive modeling of ultra-high molecular weight polyethylene under large-deformation and cyclic loading conditions,* Biomaterials **23**, 2329 (2002).

[47] E. M. Arruda and M. C. Boyce, *Evolution of plastic anisotropy in amorphous polymers during finite straining,* International Journal of Plasticity **9**, 697 (1993).

[48] O. Hasan and M. C. Boyce, *A constitutive model for the nonlinear viscoelastic viscoplastic behavior of glassy polymers,* Polymer Engineering & Science **35**, 331 (1995).

[49] D. J. Senden, S. Krop, J. van Dommelen, and L. Govaert, *Rate-and temperature-dependent strain hardening of polycarbonate,* Journal of Polymer Science Part B: Polymer Physics **50**, 1680 (2012).

[50] J. Reis, L. Pacheco, and H. da Costa Mattos, *Influence of the temperature and strain rate on the tensile behavior of post-consumer recycled high-density polyethylene,* Polymer Testing **32**, 1576 (2013).

[51] K. Wang, Y. Peng, R. Matadi Boumbimba, N. Bahlouli, D. Pessey, S. Ahzi, F. Addiego, and Y. Rémond, *Constitutive modeling of the tensile behavior of recycled polypropylene-based composites,* Materials **12**, 2419 (2019).

[52] B. P. Ferreira, *Accurate and efficient multi-scale analyses of nonlinear heterogeneous materials based on clustering-based reduced order models*, Ph.D. thesis, Computational Mechanics (2022).

[53] A. Hasan, M. C. Boyce, and S. Berko, *An investigation of the yield and postyield behavior and corresponding structure of poly (methyl methacrylate),* .

[54] S. A. Chester, *Mechanics of amorphous polymers and polymer gels signature redacted,* (2011).

[55] K. Sedighiani, M. Diehl, K. Traka, F. Roters, J. Sietsma, and D. Raabe, *An efficient and robust approach to determine material parameters of crystal plasticity constitutive laws from macro-scale stress–strain curves,* International Journal of Plasticity **134**, 102779 (2020).

[56] R. Mahnken and E. Stein, *A unified approach for parameter identification of inelastic material models in the frame of the finite element method,* Computer methods in applied mechanics and engineering **136**, 225 (1996).

[57] A. Saleeb, A. Gendy, and T. Wilt, *Parameter-estimation algorithms for characterizing a class of isotropic and anisotropic viscoplastic material models,* Mechanics of Time-Dependent Materials **6**, 323 (2002).

[58] Z. Yang and A. Elgamal, *Application of unconstrained optimization and sensitivity analysis to calibration of a soil constitutive model,* International journal for numerical and analytical methods in geomechanics **27**, 1277 (2003).

[59] A. Andrade-Campos, S. Thuillier, P. Pilvin, and F. Teixeira-Dias, *On the determination of material parameters for internal variable thermoelastic–viscoplastic constitutive models,* International journal of plasticity **23**, 1349 (2007).

[60] J. Qu, Q. Jin, and B. Xu, *Parameter identification for improved viscoplastic model considering dynamic recrystallization,* International journal of plasticity **21**, 1267 (2005).

[61] T. Furukawa, T. Sugata, S. Yoshimura, and M. Hoffman, *An automated system for simulation and parameter identification of inelastic constitutive models,* Computer methods in applied mechanics and engineering **191**, 2235 (2002).

[62] J. Kuhn, J. Spitz, P. Sonnweber-Ribic, M. Schneider, and T. Böhlke, *Identifying material parameters in crystal plasticity by bayesian optimization,* Optimization and Engineering (2021), 10.1007/s11081-021-09663-7.

[63] Z. Zhou, Y. S. Ong, P. B. Nair, A. J. Keane, and K. Y. Lum, *Combining global and local surrogate models to accelerate evolutionary optimization,* IEEE Transactions on Systems, Man, and Cybernetics, Part C (Applications and Reviews) **37**, 66 (2006).

[64] E. Schulz, M. Speekenbrink, and A. Krause, *A tutorial on gaussian process regression: Modelling, exploring, and exploiting functions,* Journal of Mathematical Psychology **85**, 1 (2018).

[65] J. R. Gardner, M. J. Kusner, Z. E. Xu, K. Q. Weinberger, and J. P. Cunningham, *Bayesian optimization with inequality constraints.* in *ICML*, Vol. 2014 (2014) pp. 937–945.

[66] T. Danka and P. Horvath, *modAL: A modular active learning framework for Python,* Available on arXiv at `https://arxiv.org/abs/1805.00979`.

[67] M. Smith, *ABAQUS/Standard User's Manual, Version 6.9* (Dassault Systèmes Simulia Corp, United States, 2009).

[68] D. Shin, A. Cupertino, M. H. de Jong, P. G. Steeneken, M. A. Bessa, and R. A. Norte, *Spiderweb nanomechanical resonators via bayesian optimization: Inspired by nature and guided by machine learning,* Advanced Materials **34** (2022), 10.1002/adma.202106248.

[69] H. Van Melick, L. Govaert, and H. Meijer, *Localisation phenomena in glassy polymers: influence of thermal and mechanical history,* Polymer **44**, 3579 (2003).

[70] F. Povolo and É. B. Hermida, *Phenomenological description of strain rate and temperature-dependent yield stress of pmma,* Journal of Applied Polymer Science **58**, 55 (1995).

[71] J. Richeton, S. Ahzi, L. Daridon, and Y. Rémond, *A formulation of the cooperative model for the yield stress of amorphous polymers for a wide range of strain rates and temperatures,* Polymer **46**, 6035 (2005).

[72] T. G. authors, *GPyOpt: A bayesian optimization framework in python,* http://github.com/SheffieldML/GPyOpt (2016).

[73] K. Hachour, F. Zaïri, M. Naït-Abdelaziz, J. M. Gloaguen, M. Aberkane, and J. M. Lefebvre, *Experiments and modeling of high-crystalline polyethylene yielding under different stress states,* International Journal of Plasticity **54**, 1 (2014).

[74] P. Wu and E. Van Der Giessen, *On improved network models for rubber elasticity and their applications to orientation hardening in glassy polymers,* Journal of the Mechanics and Physics of Solids **41**, 427 (1993).

[75] L. Anand and M. E. Gurtin, *A theory of amorphous solids undergoing large deformations, with application to polymeric glasses,* International Journal of Solids and structures **40**, 1465 (2003).

[76] A. N. Gent, *A new constitutive relation for rubber,* Rubber chemistry and technology **69**, 59 (1996).

[77] H. Dal, K. Açıkgöz, and Y. Badienia, *On the performance of isotropic hyperelastic constitutive models for rubber-like materials: a state of the art review,* Applied Mechanics Reviews **73** (2021).

[78] P. Bridgman, *The stress distribution at the neck of a tension specimen,* Trans. ASM **32**, 553 (1944).

A

STIFFNESS MATRIX

A.1. STIFFNESS MATRIX

The derivation stiffness matrix of Anand Model is shown in this section.

The stiffness matrix is derived as the following:

$$D = \frac{1}{J}\frac{\partial(M^e + M^h)}{\partial E^{e,trial}} \tag{A.1}$$

$$\frac{\partial M^e}{\partial E^{e,trial}} = \frac{\partial(M^{e,trial} - 2G\Delta t D^p_{n+1})}{\partial E^{e,trial}} \tag{A.2}$$

from the equation it is known that

$$M^{e,trial} = 2GE_d^{e,trial} + Ktr(E^{e,trial})I - 3K\alpha_T(T - T_0)I \tag{A.3}$$

$$\frac{\partial M^{e,trial}}{\partial E^{e,trial}} = 2G(I_s - I \otimes I) + KI \otimes I \tag{A.4}$$

From the equation it is known that

$$D^p_{n+1} = \frac{1}{\sqrt{2}} N^p_{n+1} \nu^p_{n+1} \tag{A.5}$$

and

$$N^p_{n+1} = N^{p,trial} \tag{A.6}$$

A

then the above equation can be rewritten as the

$$D^p_{n+1} = \frac{1}{\sqrt{2}} N^{p,trial} \nu^p_{n+1} \tag{A.7}$$

$$\frac{\partial D^p_{n+1}}{\partial E^{e,trial}} = \frac{1}{\sqrt{2}} \left[\nu^p_{n+1} \frac{\partial N^{p,trial}}{\partial E^{e,trial}} + N^{p,trial} \frac{\partial \nu^p_{trial}}{\partial E^{e,trial}} \right] \tag{A.8}$$

The non-residual equation defined in the equation

$$f = \bar{\tau}^{trial} - \Delta t G \nu^p_{n+1} - (S_1 + S_2 + \alpha_p \bar{p} + \tau_e) = 0 \tag{A.9}$$

on derivating the above equation with $E^{e,trial}$, and simple algebraic manipulations it can be written as

$$\frac{\partial \nu^p_{n+1}}{\partial E^{e,trial}} = \frac{\frac{\partial \bar{\tau}^{trial}}{\partial E^{e,trial}}}{\Delta t G + \frac{\partial (S_1 + S_2 + \alpha_p \bar{p} + \tau_e)}{\partial \nu^p_{n+1}}} \tag{A.10}$$

In the denominator of the above equation $[\Delta t G + \frac{\partial (S_1 + S_2 + \alpha_p \bar{p} + \tau_e)}{\partial \nu^p_{n+1}}]$, all the terms are scalar quantities, So the numerical derivation is the feasible and simple way.

$$\frac{\partial \bar{\tau}^{trial}}{\partial E^{e,trial}} = \sqrt{2} G N^{p,trial} \tag{A.11}$$

$$\frac{\partial N^{p,trial}}{\partial E^{e,trial}} = \frac{1}{\sqrt{2}} \left[\frac{1}{\bar{\tau}^{trail}} [I_s - I \otimes I] - \frac{2G}{\bar{\tau}^{trail}} N^{p,trial} \otimes N^{p,trial} \right] \tag{A.12}$$

on substituting the equations

$$\begin{aligned} \frac{\partial D^p_{n+1}}{\partial E^{e,trial}} = & \frac{\nu^p_{n+1}}{2\bar{\tau}^{trial}} [\frac{1}{\sqrt{2}} [\frac{1}{\bar{\tau}^{trail}} [I_s - I \otimes I] - \frac{2G}{\bar{\tau}^{trail}} N^{p,trial} \otimes N^{p,trial}]] \\ & + \frac{G N^{p,trial} \otimes N^{p,trial}}{\Delta t G + \frac{\partial (S_1 + S_2 + \alpha_p \bar{p} + \tau_e)}{\partial \nu^p_{n+1}}} \end{aligned} \tag{A.13}$$

On substituting the equation in the above

$$\begin{aligned} \frac{\partial M^e}{\partial E^{e,trial}} = & 2G(I_s - I \otimes I) + K I \otimes I - 2G \Delta t [\frac{\nu^p_{n+1}}{2\bar{\tau}^{trial}} [\frac{1}{\sqrt{2}} [\frac{1}{\bar{\tau}^{trail}} [I_s - I \otimes I] \\ & - \frac{2G}{\bar{\tau}^{trail}} N^{p,trial} \otimes N^{p,trial}]] + \frac{G N^{p,trial} \otimes N^{p,trial}}{\Delta t G + \frac{\partial (S_1 + S_2 + \alpha_p \bar{p} + \tau_e)}{\partial \nu^p_{n+1}}}] \end{aligned} \tag{A.14}$$

The stiffness matrix of the orientational hardening part is:

$$\frac{\partial M^h}{\partial E^{e,trial}} = \frac{\partial M^h}{\partial C} : \frac{\partial C}{\partial E_{n+1}} : \frac{\partial E_{n+1}}{\partial E^{e,trial}} \tag{A.15}$$

where

$$C = F^T F \tag{A.16}$$

from the equation above

$$\frac{\partial M^h}{\partial C} = \mu_R[(1 - \frac{I_1 - 3}{I_m})^{-1}](C_{dis})_0 \tag{A.17}$$

where

$$C_{dis} = J^{\frac{-2}{3}} C \tag{A.18}$$

and $(C_{dis})_0$ is the deviotoric part of C_{dis}.

On devrivating and making the few algebraic manipulations the

$$\begin{aligned}\frac{\partial M^h}{\partial C} = \mu_R J^{\frac{-2}{3}} [((1 - \tfrac{I_1-3}{I_m})^{-1})[I_s - \tfrac{1}{3}(C^{-1})^T \otimes C - \tfrac{1}{3} I \otimes I + \tfrac{1}{9} tr(C)(C^{-1})^T \otimes I] \\ + \frac{1}{I_m}(1 - \frac{I_1 - 3}{I_m})^{-2}[I \otimes (C_{dis})_0 - tr(C) C^{-T} \otimes (C_{dis})_0]]\end{aligned} \tag{A.19}$$

on substituting in the above equation

$$\frac{\partial M^h}{\partial E^{e,trial}} = \frac{\partial M^h}{\partial C} : \frac{\partial exp(2E_{n+1})}{\partial En + 1} : I_s \tag{A.20}$$

The derivative of the exponential of the matrix is evaluated using the procedure mentioned in the suzo neto book.

So the total stiffness matrix is calculated as:

$$D = \frac{1}{J} \frac{\partial (M^e + M^h)}{\partial E^{e,trial}} \tag{A.21}$$

A.2. NUMERICAL CONSISTENT TANGENT OPERATOR

Consistent tangent operator, C_t, is found by numerical differentiation. The deformation gradient is perturbed in such a way that only one of the six unique components of the rate-of-deformation tensor is changed at the time, i.e.,

$$F_{\pm}^{kl} = \pm \frac{\epsilon}{2}[(e_k \otimes e_l)F + (e_l \otimes e_k)F] \tag{A.22}$$

where ϵ is the perturbation coefficient set equal to 10^{-8} and e_k for k = 1, 2, 3 are the Cartesian base vectors. The perturbed deformation gradient, $F^{(kl)}$, is then obtained as

$$F_{\pm}^{kl} = F \pm \Delta F \tag{A.23}$$

For each of the twelve deformation gradients thus obtained, the Cauchy stress tensor $\sigma(F^{kl})$ is calculated. Using a central difference scheme, the consistent tangent operator C_t is estimated as

$$C^t_{ij(kl)} = \frac{\sigma(F_+^{kl}) - \sigma(F_-^{kl})}{2\epsilon} \tag{A.24}$$

In Voigt notation this means that for each plus-minus perturbation of the deformation gradient, we obtain column (kl) in the 6×6 tangent operator C_t with row indices i j = 11, 22, 33, 12, 13, 23.

A.3. NUMERICAL INTEGRATION SCHEME OF JOHNSEN MODEL

In the constitutive time integration scheme, it is known that

$$dt, F_n, F_{n+1}, F_n^p, T_n, T_{n+1}, \sigma_n \tag{A.25}$$

at time t_n. To compute

$$\sigma_{n+1}, F_{n+1}^p, \dot{p} \tag{A.26}$$

at t_{n+1}. The evolution equation to calculate the plastic gradient tensor considered here is

$$\dot{F}_{n+1}^p = D_{n+1}^p F_{n+1}^p \tag{A.27}$$

$$F_{n+1}^p = F_n^p + \Delta t D_{n+1}^p F_{n+1}^p \tag{A.28}$$

By substituting the D^p from the equation 2.62 as $D_{n+1}^p = \frac{\Delta p}{\Delta t} * N$ in the above equation A.28 leads to

$$F_{n+1}^p = F_n^p + \Delta p N F_{n+1}^p \tag{A.29}$$

By making the trivial algebraic calculations, the inverse of plastic deformation gradient tensor is calculated as

$$(F_{n+1}^p)^{-1} = (1 - \Delta p_{n+1}(F_{n+1})^{-1} N_n F_{n+1})(F_n^p)^{-1} \tag{A.30}$$

where N_n can be calculated from the equation 2.63. The elastic deformation gradient tensor can be calculated as

$$F_{n+1}^e = F_{n+1}(F_{n+1}^p)^{-1} \tag{A.31}$$

Using the elastic deformation gradient and its polar decomposition the von Mises equivalent stress can be calculated using the equations 2.61. The constitutive relations for the two dashpots gives the residual equation as the function of the plastic strain rate as shown below

$$f(\dot{p}_{n+1}) = f_{n+1} = \sigma_{D,n+1}^{vm} - \sigma_{v,n+1} \tag{A.32}$$

where $\sigma_{v,n+1}$ is the viscous stress calculated using the Eyrings equation (5.16). The updated value of the equivalent plastic strain rate is estimated using the secant numerical method.

$$\dot{p}^{i+1}_{n+1} = \dot{p}^{i}_{n+1} - f^{i}_{n+1}\frac{\dot{p}^{i}_{n+1} - \dot{p}^{i-1}_{n+1}}{f^{i}_{n+1} - f^{i+1}_{n+1}} \tag{A.33}$$

The numerical iteration procedure continues until the criteria of convergence is fulfilled. So the value of stress ($\sigma^{e}_{A,n+1}$) contribution from part A is

$$\sigma^{e}_{A,n+1} = \frac{2}{J}\mu_A(T)\ln(V^e) \tag{A.34}$$

The value of the stress ($\sigma_{B,n+1}$ in part B is explicitly dependent on the deformation gradient F_{n+1} and T_n and is estimated as

$$\sigma_{B,n+1} = \frac{1}{J}(\frac{\mu_B(T)\lambda_{lock}}{3\overline{\lambda}_{c,n+1}}L^{-1}(\frac{\overline{\lambda}_{c,n+1}}{\lambda_{lock}})B_{D,n+1} - \kappa_B\ln(J_{n+1}I - 3\kappa_B\alpha(T_n - T_0)I) \tag{A.35}$$

So the total stress

$$\sigma_{n+1} = \sigma^{e}_{A,n+1} + \sigma_{B,n+1} \tag{A.36}$$

A.4. NUMERICAL INTEGRATION ALGORITHM OF MIRKHALAF MODEL

In the constitutive time integration scheme, it is known that

$$dt, F_n, F_{n+1}, \varepsilon^p_n, \overline{\varepsilon}^p_n \sigma_n \tag{A.37}$$

at time t_n. To compute

$$\sigma_{n+1}, \varepsilon^p_{n+1}, \overline{\varepsilon}^p_{n+1} \tag{A.38}$$

at t_{n+1}. The evolution equation to calculate the accumulated plastic strain considered here is

$$\dot{\overline{\varepsilon}}^p = \frac{1}{\sqrt{3}}\dot{\gamma} \tag{A.39}$$

The incremental accumulated plastic strain is obtained as

$$\overline{\varepsilon}^p_{n+1} = \overline{\varepsilon}^p_n + \frac{\Delta t}{\sqrt{3}}\Delta\gamma \tag{A.40}$$

From the viscoplastic flow rule, the plastic strain rate is obtained from the equation 2.86.

$$\dot{\varepsilon}^p = \frac{\tau_d}{2\eta} \tag{A.41}$$

It is considered that the viscoplastic flow rule is purely deviotoric and the incremental plastic strain obtained from the above equation as

$$\varepsilon^p_{d,n+1} = \varepsilon^p_{d,n} + \frac{\Delta t}{2\eta_{n+1}}\tau_{d,n+1} \tag{A.42}$$

A

From the equation 2.78 and 2.79 the plastic multiplier can be written as

$$\dot{\gamma} = \sqrt{2d^p : d^p} \tag{A.43}$$

By replacing d^p with the equation 2.86 yields

$$\dot{\gamma} = \frac{1}{2\eta}\sqrt{2\tau_d : \tau_d} \tag{A.44}$$

On substituting the equation A.45 in equation A.41 the accumulated plastic strain is obtained as

$$\bar{\varepsilon}^p_{n+1} = \bar{\varepsilon}^p_n + \frac{\sqrt{3}\Delta t}{3\eta_{n+1}}\tau^{eq}_{n+1} \tag{A.45}$$

where viscosity is

$$\eta_{n+1} = A_0 exp[\frac{\Delta H}{RT} + \frac{\mu P_{n+1}}{\tau_0} - D_\infty + D_\infty exp(\frac{-h\sqrt{3}\bar{\varepsilon}^p_{n+1}}{\sqrt{2D_\infty}})][\frac{\tau^{eq}_{n+1}}{sinh(\frac{\tau^{eq}_{n+1}}{\tau_0})}] \tag{A.46}$$

As the explained in the chapter 3, the trial strain is obtained as

$$\varepsilon^{trial}_{n+1} = \varepsilon_{n+1} - \varepsilon^p_n \tag{A.47}$$

The deviotoric stress tensor can be expressed as

$$\tau_{d,n+1} = 2G\varepsilon^e_{d.n+1} = 2G(\varepsilon_{d.n+1} - \varepsilon^p_{d.n+1}) \tag{A.48}$$

on substituting the equation (6.41) in the above equation, and by straightforward algebraic manipulations

$$\tau_{d,n+1} = \frac{\eta_{n+1}}{\eta_{n+1} + \Delta t G}\tau^{trial}_{d,n+1} \tag{A.49}$$

where

$$\tau^{trial}_{d,n+1} = 2G\varepsilon^{trial}_{n+1} \tag{A.50}$$

The equivalent deviotoric stress can be written in terms of trial stress as

$$\tau^{eq}_{n+1} = \sqrt{\frac{1}{2}\tau_{d,n+1} : \tau_{d,n+1}} = \sqrt{\frac{1}{2}}\frac{\eta_{n+1}}{\eta_{n+1} + \Delta t G}||\tau^{trial}_{d,n+1}|| \tag{A.51}$$

The accumulated plastic strain and plastic are rewritten in terms of the trial stress as

$$\bar{\varepsilon}^p_{n+1} = \bar{\varepsilon}^p_n + \frac{1}{\sqrt{6}}\frac{\Delta t}{(\eta_{n+1} + \Delta t)}||\tau^{trial}_{d,n+1}|| \tag{A.52}$$

$$\varepsilon^p_{n+1} = \varepsilon^p_n + \frac{\Delta t}{2(\eta_{n+1} + \Delta t)}\tau^{trial}_{d,n+1} \tag{A.53}$$

On substituting the equations A.52 and A.53 in the equation A.47 and reduced to a single scalar non-linear residual equation as

$$R = \eta_{n+1} - C_1\frac{C_2}{C_3} \tag{A.54}$$

where

$$C_1 = A_0 exp[\frac{\Delta H}{R*T} + \frac{\mu P_{n+1}}{\tau_0} - D_\infty + D_\infty exp[-\sqrt{\frac{3}{2}}\frac{h}{D_\infty}C_4]] \tag{A.55}$$

$$C_2 = \sqrt{\frac{1}{2}}(\frac{\eta_{n+1}}{\eta_{n+1}+\Delta t G})||\tau^{trial}_{d,n+1}|| \tag{A.56}$$

$$C_3 = \sinh\frac{1}{\tau_0}\sqrt{\frac{1}{2}}(\frac{\eta_{n+1}}{\eta_{n+1}+\Delta t G})||\tau^{trial}_{d,n+1}|| \tag{A.57}$$

$$C_4 = \bar{\varepsilon}^p_n + \frac{1}{3}\sqrt{\frac{3}{2}}\frac{\Delta t}{\eta_{n+1}+\Delta t G}||\tau^{trial}_{d,n+1}|| \tag{A.58}$$

The $\eta n+1$ solved using the Newton-Raphson method.

$$\eta^k_{n+1} = \eta^{k-1}_{n+1} - \frac{R^{k-1}}{\frac{\partial R^{k-1}}{\partial \eta^{k-1}_{n+1}}} \tag{A.59}$$

The derivative of residual is trivial and given as

$$\frac{\partial R}{\partial \eta} = 1 - \frac{C_2}{C_3}\frac{\partial C_1}{\partial \eta} - \frac{C_1}{C_3}\frac{\partial C_2}{\partial \eta} + \frac{\partial C_3}{\partial \eta}\frac{C_1 C_2}{C_3^2} \tag{A.60}$$

After the estimation of the viscosity the accumulated plastic strain, plastic strain tensor and Cauchy stress are calculated using the equations mentioned above.

CONSISTENT TANGENT OPERATOR

The spatial tangent modulus is estimated as

$$a_{ijkl} = \frac{1}{2J}[D:L:\mathbf{B}]_{ijkl} - \sigma_{il}\delta_{jk} \tag{A.61}$$

where D is the elastic-viscoplastic consistent tangent operator. The fourth order tensor L is estimated as

$$L = \frac{\partial \ln[B^{e,trial}_{n+1}]}{\partial [B^{e,trial}_{n+1}]} \tag{A.62}$$

and the fourth order tensor **B** is defined as

$$\mathbf{B}_{ijkl} = \delta_{ik}[B^{e,trial}_{n+1}]_{jl} + \delta_{jk}[B^{e,trial}_{n+1}]_{il} \tag{A.63}$$

The closed form of the elasto-viscoplastic consistent tangent operator D is defined as

$$D^{evp} = [\frac{\Delta t G}{(\eta_{n+1})^2}(\frac{\partial R}{\partial \eta_{n+1}})^{-1}F_1(1-F_2-F_3)\tau_{d,n+1}\otimes\tau_{d,n+1} - \frac{\Delta t G}{\eta_{n+1}(\eta_{n+1}+\Delta t G)}$$

$$(\frac{\partial R}{\partial \eta_{n+1}})^{-1}C_1\frac{C_2}{C_3}\frac{\mu K}{\tau_0}\tau_{d,n+1}\otimes I + \frac{\eta_{n+1}}{\eta_{n+1}+\Delta t G}2GI_D + KI\otimes I + HI_D] \tag{A.64}$$

A

A.5. NUMERICAL INTEGRATION ALGORITHM OF ANAND MODEL

In the constitutive time integration scheme, it is known that

$$dt, F_n, F_{n+1}, F_n^p, S_{a,n}, S_{b,n}, v_n^p, \sigma_n \tag{A.65}$$

at time t_n. To compute

$$\sigma_{n+1}, F_{n+1}^p, S_{a,n}, S_{b,n}, v_n^p \tag{A.66}$$

at t_{n+1}. The evolution equation to determine the plastic deformation gradient tensor using the exponential map is

$$F_{n+1}^p = exp(\Delta t D_{n+1}^p) F_n^p \tag{A.67}$$

The trial deformation gradient is calculated using the equation

$$F_{n+1}^{tr} = F_{n+1}(F_n^p)^{-1} \tag{A.68}$$

From the multiplicative split of deformation gradient tensor, the elastic gradient can be written as

$$F_{n+1}^e = F_{n+1}(F_{n+1}^p)^{-1} \tag{A.69}$$

on substituting the plastic deformation gradient evolution equation in the above equation the relation between the trial deformation gradient and elastic deformation gradient is obtained as

$$F_{n+1}^e = F^{tr} exp[-\Delta t D_{n+1}^p] \tag{A.70}$$

$$R_n^e + 1 = R^{tr} \tag{A.71}$$

$$U_n^e + 1 = U^{tr} exp[-\Delta t D_{n+1}^p] \tag{A.72}$$

On applying the logarithm on both sides, the relation between the trial strain and elastic strain is obtained as

$$E_{n+1}^e = E^{tr} - \Delta t D_{n+1}^p \tag{A.73}$$

since D_{n+1}^p is deviotoric all the time, the above equation can be written as

$$E_{d,n+1}^e = E_d^{tr} - \Delta t D_{n+1}^p \tag{A.74}$$

On multiplying with 2G the above equation can be rewritten as

$$M_{d,n+1}^e = M_d^{tr} - 2G\Delta t D_{n+1}^p \tag{A.75}$$

Since the effective stress is the driving flow for the plasticity, the deviotoric effective stress is defined as

$$(M_{d,n+1}^e)_{eff} = (M_d^{tr})_{eff} - (M_{back})_n - 2G\Delta t D_{n+1}^p \tag{A.76}$$

then defining the rate of deformation gradient tensor

$$D_{n+1}^p = \frac{1}{\sqrt{2}} v_{n+1}^p N_{n+1}^p \tag{A.77}$$

$$N^p_{n+1} = \frac{(M^e_{d,n+1})_{eff}}{\sqrt{2}\overline{\tau}_{n+1}} \tag{A.78}$$

$$\overline{\tau}_{n+1} = \frac{||(M^e_{d,n+1})_{eff}||}{\sqrt{2}} \tag{A.79}$$

The effective trial stress is defined as

$$(M^{tr}_d)_{eff} = (M^{tr}_d) - (M_{back})_n \tag{A.80}$$

$$(N^p)^{tr} = \frac{(M^{tr}_d)_{eff}}{\sqrt{2}\overline{\tau}^{tr}} \tag{A.81}$$

It is assumed that

$$(N^p)^{tr} = N^p_{n+1} \tag{A.82}$$

as the direction of plastic flow is equal.

$$\sqrt{2}N^p_{n+1}\overline{\tau}_{n+1} = \sqrt{2}(N^p)^{tr}\overline{\tau}^{tr} - \sqrt{2}\Delta t G v^p_{n+1} N^p_{n+1} \tag{A.83}$$

This leads to the important relation as

$$\overline{\tau}_{n+1} = \overline{\tau}^{tr} - \Delta t G v^p_{n+1} \tag{A.84}$$

EVOLUTION EQUATION FOR INTERNAL VARIABLES

The value of the deformation resistance is estimated as

$$S_{a,n+1} = \frac{S_{a,n} + h_a b \Delta t v^p_{n+1}(\varphi^*_{n+1} - \varphi_{n+1})}{1 + \Delta t h_a v^p_{n+1}} \tag{A.85}$$

where

$$\varphi_{n+1} = \frac{\varphi_n + \Delta t g v^p_{n+1}\varphi^*_{n+1}}{1 + \Delta t g v^p_{n+1}} \tag{A.86}$$

$$\varphi^*_{n+1} = \varphi_r[1 + (\frac{T_{c,n+1} - T_{n+1}}{k})^r](\frac{v^p_{n+1}}{v_r})^s \tag{A.87}$$

The value of deformation resistance S_b is estimated as

$$S_{b,n+1} = \frac{S_{b,n} + h_b \Delta t v^p_{n+1}(\overline{\lambda}_{n+1} - 1)}{1 + \Delta t h_b v^p_{n+1}(\overline{\lambda}_{n+1} - 1)} \tag{A.88}$$

The evolution equation for the internal variable A is defined as

$$A_{n+1} = A_n + \Delta t(D^p_{n+1}A_n + A_n D^p_{n+1} - \gamma A_n \ln A_n v^p_{n+1}) \tag{A.89}$$

A

SOLUTION OF IMPLICIT EQUATION ν^p_{n+1}

From the flow rule

$$\nu^p_{n+1} = \nu_0 \exp(-\frac{Q}{K_B T})[\sinh[\frac{(\tau_e)_{n+1} V}{2K_B T}]]^{\frac{1}{m}} \tag{A.90}$$

on rearranging the above term the shear stress is calculated as

$$\tau_e = \frac{2K_B T_{n+1}}{V} sinh^{-1}[(\frac{\nu^p_{n+1}}{\nu^*})^m] \tag{A.91}$$

where

$$\nu^* = \nu_0 \exp(-\frac{Q}{K_B T}) \tag{A.92}$$

The non-linear residual function in terms of plastic multiplier is developed from shear yielding theory is

$$F = \overline{\tau}_{n+1} - S_{a,n+1} - S_{b,n+1} - \alpha_p \overline{p} - \tau_{e,n+1} \tag{A.93}$$

The ν^p_{n+1} is solved using the newton raphson method. On substituting the equations 2.104 and 2.109 The total stress is calculated using the equation

$$\sigma = \sigma^{(1)} + \sigma^{(2)} \tag{A.94}$$

B

Material Parameter Calibration

In the present chapter the parametric study of the three models developed by Johnsen et al. [1], Mirkhalaf et al. [2] and Anand et al. [3] is made. The study is important to select the bounds of the material parameters in the Bayesian Optimization.

B.1. Role of Material Properties in Johnsen Model

The implemented finite strain elasto-viscoplastic constitutive model accounts for a total of 9 material properties. For the purpose of understanding the influence of each material property on the predicted elasto-viscoplastic behaviour, a systematic parametric study on the tensile test at $T = 298$ K, $\dot{\varepsilon} = 10^{-3}\ s^{-1}$ has made.

In the following parametric studies, the properties of Low density polyethylene mentioned in the table B.1 are taken as reference [1]. Each material property is then changed in turn, while keeping the remaining constant, in order to ascertain its effect on the predicted material behaviour. From the results obtained in the clearly show that the material properties can be classified in three categories as:

- Properties affecting the Elastic behaviour: G
- Properties affecting the Yield point: ΔH_α, ΔH_β, V_α, V_β, $\dot{p}_{0,\alpha}$ and $\dot{p}_{0,\beta}$
- Properties affecting the post yield behaviour: b_α, b_β, $\mu_{B,ref}$, κ_B and λ_{lock}

B

Table B.1: Material Properties considered for parametric study of Johnsen Model [1]

Properties	LDPE
$\mu_{A,ref}$	46 MPa
a_A	0.028 K^{-1}
ΔH_α	179.5 KJ/mol
V_α	4.72 nm^3
$\dot{p}_{0,\alpha}$	$2.36 * 10^{25}$ s^{-1}
b_α	3 (-)
ΔH_β	196.1 KJ/mol
V_β	3.19 nm^3
$\dot{p}_{0,\beta}$	$6.13 * 10^{36}$ s^{-1}
b_β	10 (-)
$\mu_{B,ref}$	2 MPa
κ_B	1500 MPa
λ_{lock}	5.2 (-)

B.1.1. ELASTIC BEHAVIOUR

Concerning the elastic behaviour, it is only verified the influence of the shear modulus, G. In Figure B.1, the true stress - true strain and force - displacement curves are shown for four different values of the shear modulus. As expected, an increase of G leads to a corresponding increase of the slope in the elastic domain, consistent with an increase of the material stiffness.

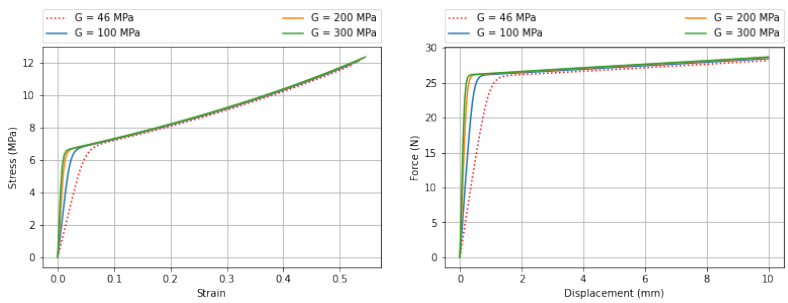

(a) (b)

Figure B.1: Variation of G: (a) True stress-true strain curves (b) Force-displacement curves

B.1.2. YIELD POINT

Concerning the yield point, the material properties such as activation energy of α relaxation (ΔH_α) and of β relaxation(ΔH_β) both similarly affects the yield point. As the the value of activation energy increases the value yield strength of the material also increases. As the material property activation volume of α relaxation (V_α) increases the

yield strength of the material decreases. It also been observed that the activation volume of β relaxation does not affect the yield point significantly. The reference plastic strain rates of the both α relaxation($\dot{p}_{0,\alpha}$) and β relaxation ($\dot{p}_{0,\beta}$) affects the yield strength similarly. As the value of reference plastic strain rate value increases, the yield strength of the material decreases. The parametric study of the material properties affecting the yield strength are clearly shown in the figures B.2 to B.7.

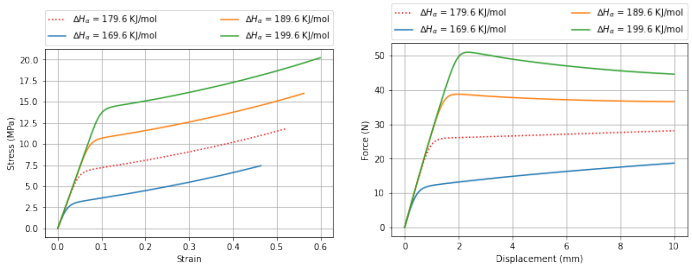

(a) (b)

Figure B.2: Variation of ΔH_α: (a) True stress-true strain curves (b) Force-displacement curves

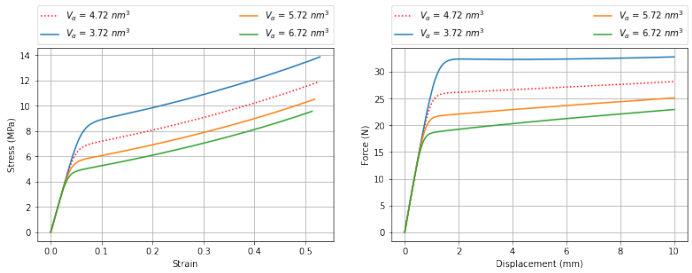

(a) (b)

Figure B.3: Variation of V_α: (a) True stress-true strain curves (b) Force-displacement curves

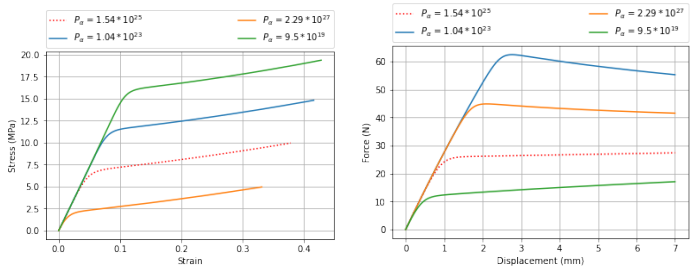

(a) (b)

Figure B.4: Variation of $\dot{p}_{0,\alpha}$: (a) True stress-true strain curves (b) Force-displacement curves

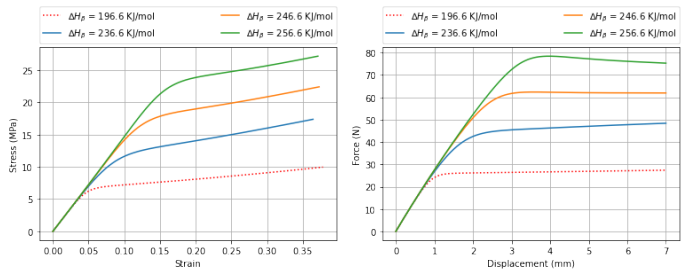

(a) (b)

Figure B.5: Variation of ΔH_β: (a) True stress-true strain curves (b) Force-displacement curves

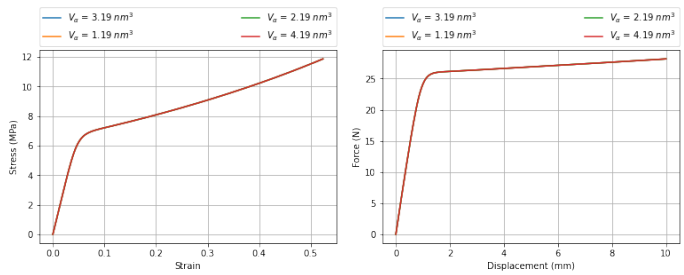

(a) (b)

Figure B.6: Variation of V_β: (a) True stress-true strain curves (b) Force-displacement curves

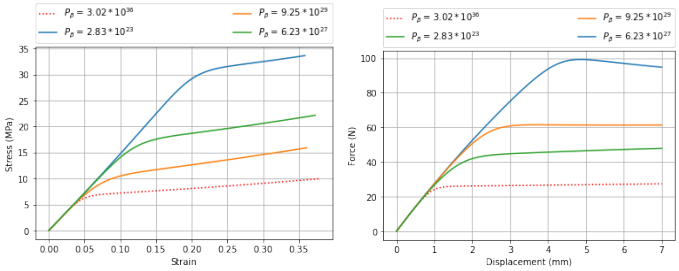

(a) (b)

Figure B.7: Variation of $\dot{p}_{0,\beta}$: (a) True stress-true strain curves (b) Force-displacement curves

B.1.3. POST YIELD BEHAVIOUR

Concerning the post-yield behaviour, As the value of b_α, Bulk modulus(κ_B) and locking stretch (λ_{lock}) increases, both the true stress and force values increases as shown in the figures B.8 to B.10

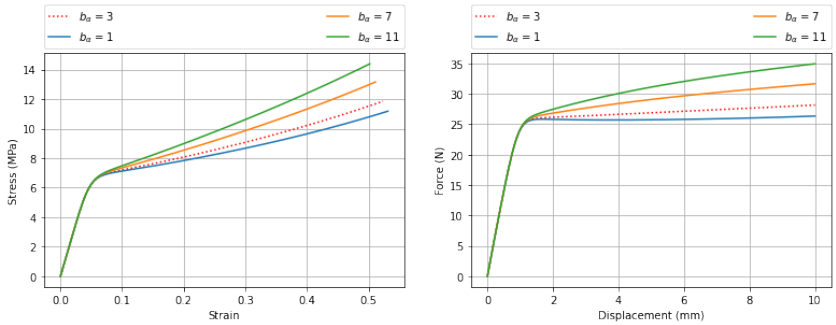

(a) (b)

Figure B.8: Variation of b_α: (a) True stress-true strain curves (b) Force-displacement curves

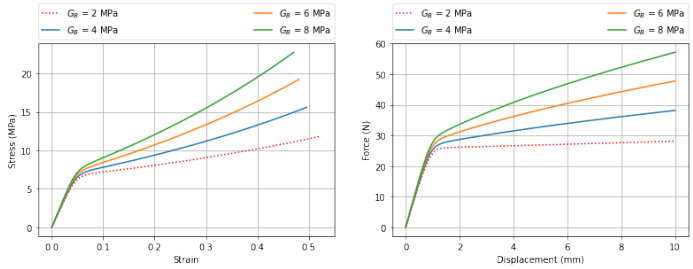

(a) (b)

Figure B.9: Variation of $\mu_{B,ref}$: (a) True stress-true strain curves (b) Force-displacement curves

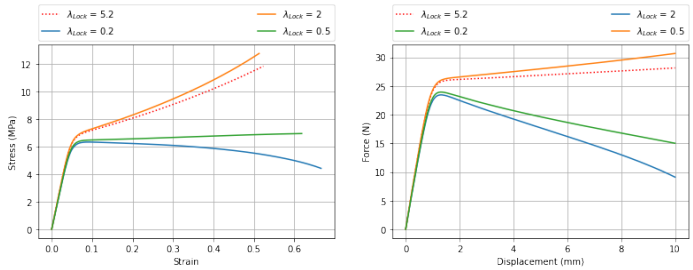

(a) (b)

Figure B.10: Variation of λ_{lock}: (a) True stress-true strain curves (b) Force-displacement curves

B.2. ROLE OF MODEL MATERIAL PROPERTIES IN MIRKHALAF MODEL

The implemented finite strain elasto-viscoplastic constitutive model accounts for a total of 9 material properties. For the purpose of understanding the influence of each material property on the predicted elasto-viscoplastic behaviour, a systematic parametric study on the tensile test at $T = 293K$, $\dot{\varepsilon} = 10^{-3}s^{-1}$ and atmospheric pressure $p = 10^5 Pa$.The dimensions of the tensile test specimen are shown in the figure 3.2. The specimen is discretized in 2544 C3D8R elements as shown in the figure 3.2.

In the following parametric studies, the properties of PS are taken as reference **??**. Each material property is then changed in turn, while keeping the remaining constant, in order to ascertain its effect on the predicted material behaviour. The results obtained clearly show that the material properties can be classified in three categories as:

- Properties affecting the Elastic behaviour: E and ν
- Properties affecting the Yield point: ΔH, A_0, τ^* and μ.

- Properties affecting the post yield behaviour: h, D_∞ and H

B.2.1. ELASTIC BEHAVIOUR

Concerning the elastic behaviour, it is only verified the influence of the Young modulus, E. In Figure the true stress - true strain and force - displacement curves are shown for four different values of the Young modulus. As expected, an increase of E leads to a corresponding increase of the slope in the elastic domain, consistent with an increase of the material stiffness.

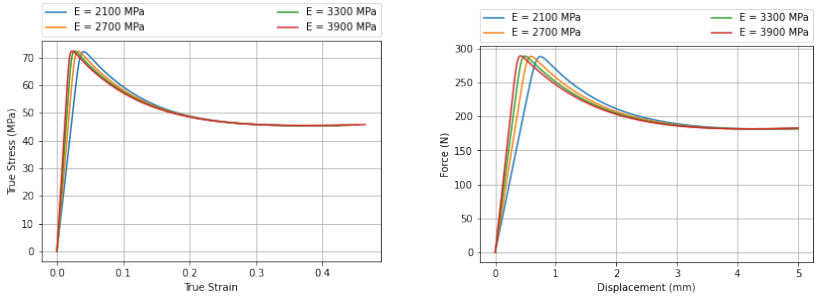

(a) (b)

Figure B.11: Variation of E (a) True stress-true strain behaviour (b) Force-displacement curves

B.2.2. YIELD POINT

Concerning the yield point, all four material properties (activation energy, ΔH, fundamental vibration temperature factor, A_0, characteristic stress τ_0, and pressure coefficient, μ) seem to have a similar effect on the material behaviour, as can be clearly seen in Figures. An increase of any of these properties results in a upward translation of both true stress - true strain and force - displacement curves, keeping the elastic and post yield behaviours essentially unchanged.

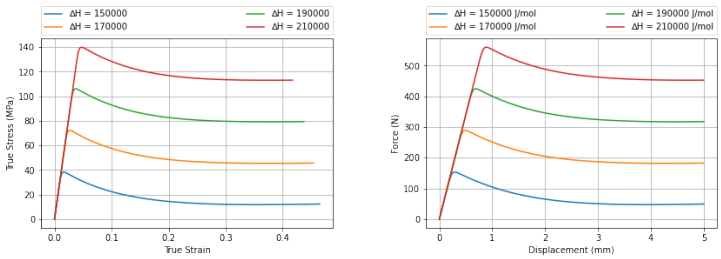

(a) (b)

Figure B.12: Variation of ΔH (a) True stress-true strain behaviour (b) Force-displacement curves

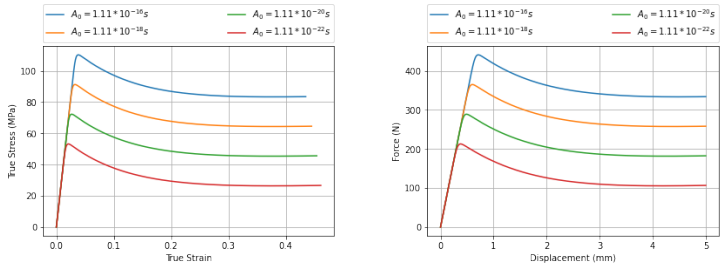

(a) (b)

Figure B.13: Variation of A_0 (a) True stress-true strain behaviour (b) Force-displacement curves

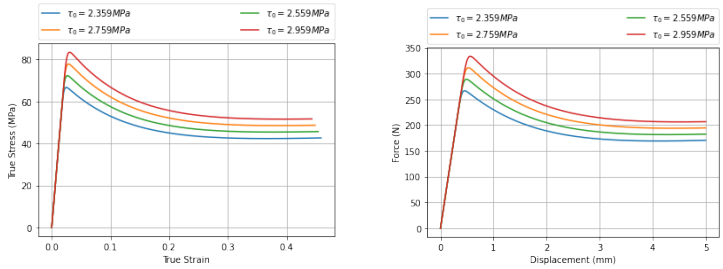

(a) (b)

Figure B.14: Variation of τ_0 (a) True stress-true strain behaviour (b) Force-displacement curves

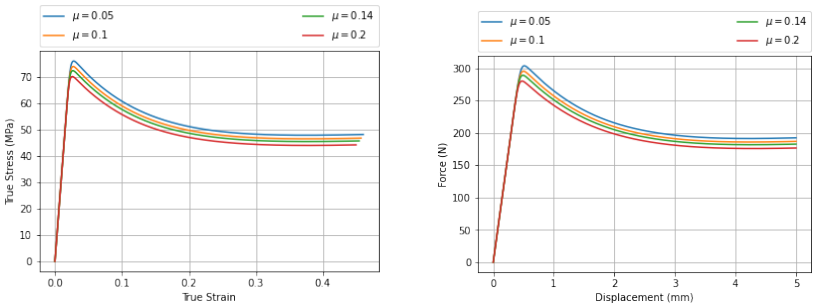

(a) (b)

Figure B.15: Variation of μ (a) True stress-true strain behaviour (b) Force-displacement curves

B.2.3. POST YIELD BEHAVIOUR

Regarding the post yield behaviour, the two material properties related with the strain softening phenomenon (softening slope, h, and softening saturation, D_∞) have the expected influence from the physical point of view. Observation of figure B.16 shows that the softening slope parameter, h, essentially affects the stress drop region resultant from the strain softening, after which the curves tend to converge as the strain hardening evolves. An increase of h leads to an increase of the curve concavity and a more pronounced stress drop. In turn, Figure shows that an increase of the softening saturation parameter, D_∞ also leads to a more pronounced stress drop by increasing the material susceptibility to strain softening. However, the curves no longer tend to converge as the strain hardening evolves, exhibiting a translational pattern instead. In what concerns the hardening modulus, H, the influence is evident and physically consistent. An increase of H leads to an increase of the material strain hardening and the associated increase of the tangent modulus on the hardening region, as shown in figure B.12.

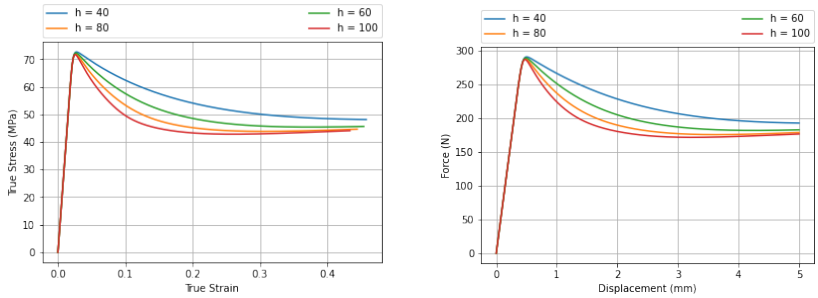

(a) (b)

Figure B.16: Variation of h (a) True stress-true strain behaviour (b) Force-displacement curves

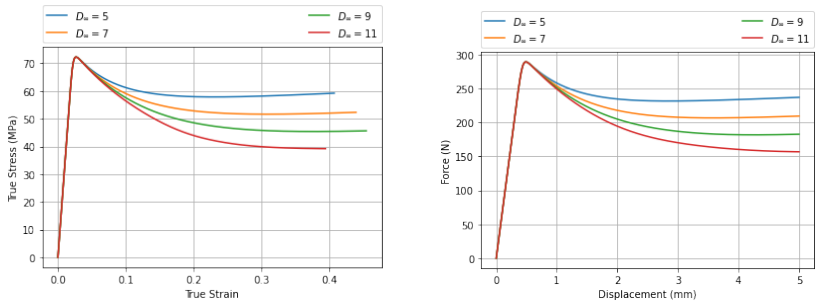

(a) (b)

Figure B.17: Variation of D_∞ (a) True stress-true strain behaviour (b) Force-displacement curves

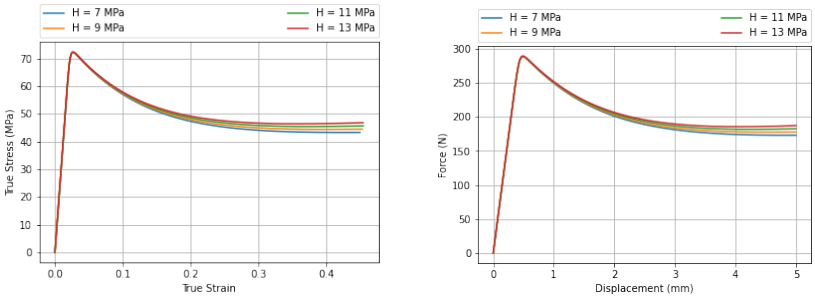

(a) (b)

Figure B.18: Variation of H (a) True stress-true strain behaviour (b) Force-displacement curves

B.3. ROLE OF MODEL MATERIAL PROPERTIES IN ANAND MODEL

The implemented finite strain elasto-viscoplastic constitutive model accounts for a total of 9 material properties. For the purpose of understanding the influence of each material property on the predicted elasto-viscoplastic behaviour, a systematic parametric study on the tensile test at $T = 298K$, $\dot{\varepsilon} = 3 * 10^{-4} s^{-1}$.The dimensions of the tensile test specimen are shown in the figure previous chapter. The specimen is discretized in 2544 C3D8RT elements as shown in the figure 3.2.

In the following parametric studies, the properties of zenox 690R are taken as reference [3]. Each material property is then changed in turn, while keeping the remaining constant, in order to ascertain its effect on the predicted material behaviour. The results obtained clearly show that the material properties can be classified in three categories as:

- Properties affecting the Elastic behaviour: **G** and ν
- Properties affecting the Yield point: Q, m, V, α_p and ν
- Properties affecting the post yield behaviour: h, b, g_1, ϕ_r, k and X

B.3.1. ELASTIC BEHAVIOUR

Concerning the elastic behaviour, it is only verified the influence of the Shear modulus, G. In Figure the true stress - true strain and force - displacement curves are shown for four different values of the shear modulus. As expected, an increase of G leads to a corresponding increase of the slope in the elastic domain, consistent with an increase of the material stiffness as shown in the figure B.1

B.3.2. YIELD POINT

Concerning the yield point, sensitivity study of all five material properties (activation energy, Q, pre-exponential factor, ν_0, pressure sensitivity factor α_p, activation volume V and strain sensitivity parameter, m) is made. It seems that an increase in the activa-

tion energy and strain sensitivity parameter leads the results to translate in the upward direction of both true stress - true strain and Force - displacement curves and increase of parameters such as activation volume, pre exponential factor and pressure sensitivity factor leads to the downward translation, keeping the elastic and post yield behaviours essentially unchanged.

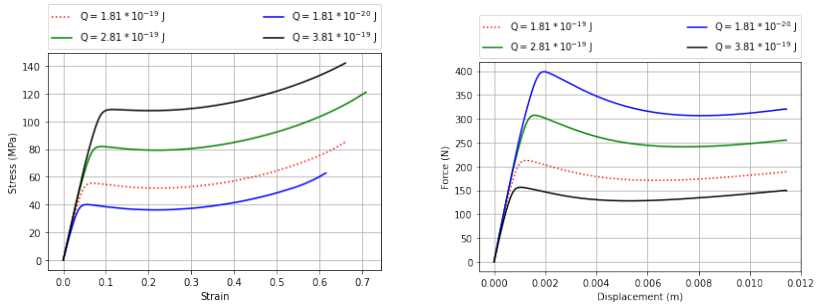

(a) (b)

Figure B.19: Variation of Q: (a) True stress-true strain behaviour (b) Force-displacement curves

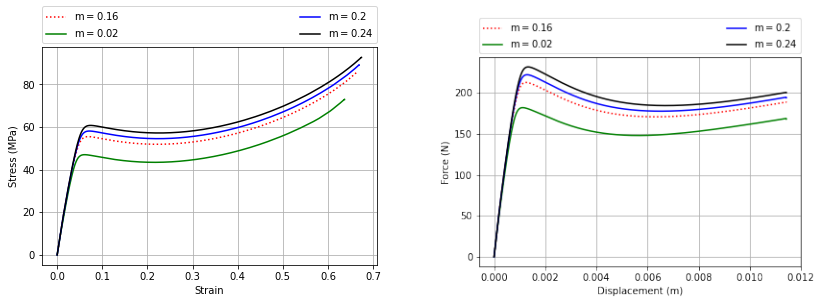

(a) (b)

Figure B.20: Variation of m: (a) True stress-true strain behaviour (b) Force-displacement curves

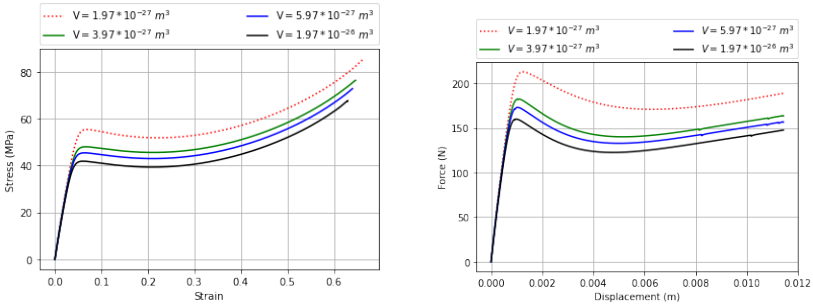

(a) (b)

Figure B.21: Variation of V: (a) True stress-true strain behaviour (b) Force-displacement curves

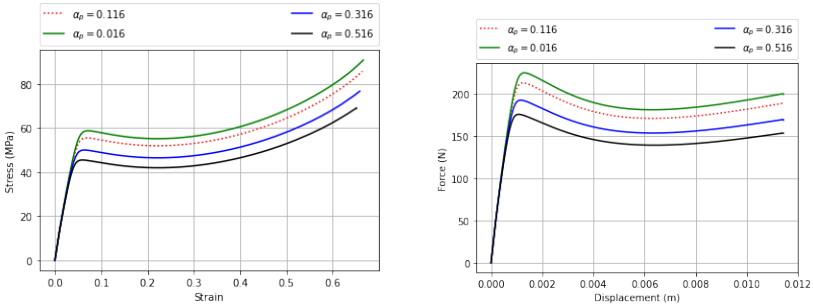

(a) (b)

Figure B.22: Variation of α_p: (a) True stress-true strain behaviour (b) Force-displacement curves

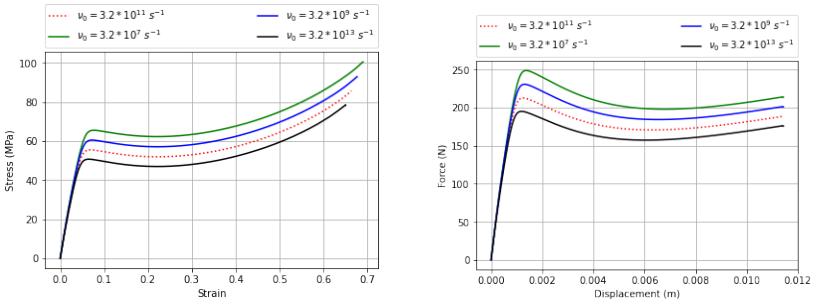

(a) (b)

Figure B.23: Variation of ν_0: (a) True stress-true strain behaviour (b) Force-displacement curves

B.3.3. POST-YIELD RESPONSE

Concerning the post-yield response, sensitivity study of all six material properties (b, h, ϕ_r, g_1, k, Back stress (X)) is made. It is observed that increase of b, h, ϕ_r and Back stress leads the results to translate in the upward direction of both true stress - true strain and Force - displacement curves and increase of parameters such as G_1 and k leads to the downward translation, keeping the elastic and post yield behaviours essentially unchanged.

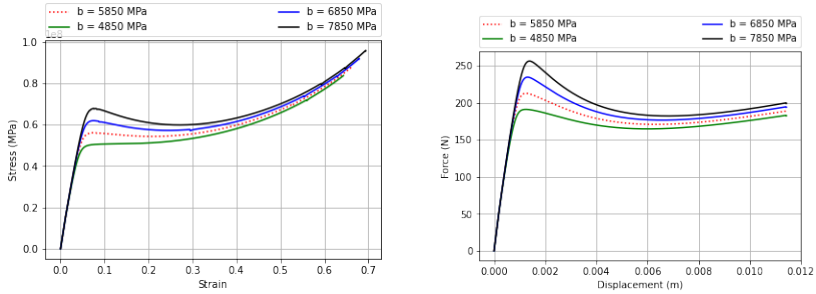

(a) (b)

Figure B.24: Variation of b: (a) True stress-true strain behaviour (b) Force-displacement curves

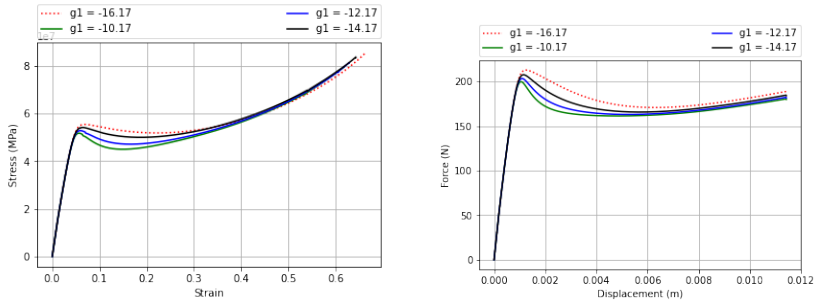

(a) (b)

Figure B.25: Variation of g_1: (a) True stress-true strain behaviour (b) Force-displacement curves

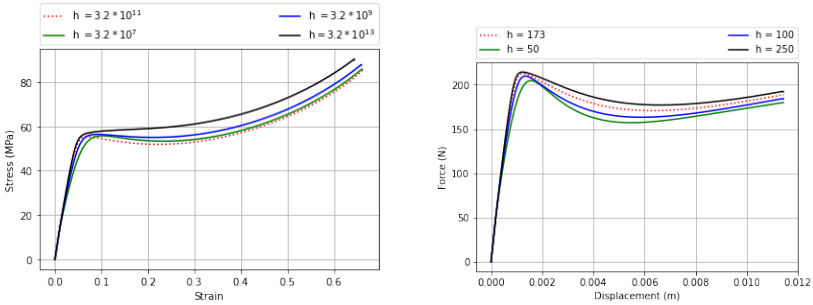

(a) (b)

Figure B.26: Variation of h: (a) True stress-true strain behaviour (b) Force-displacement curves

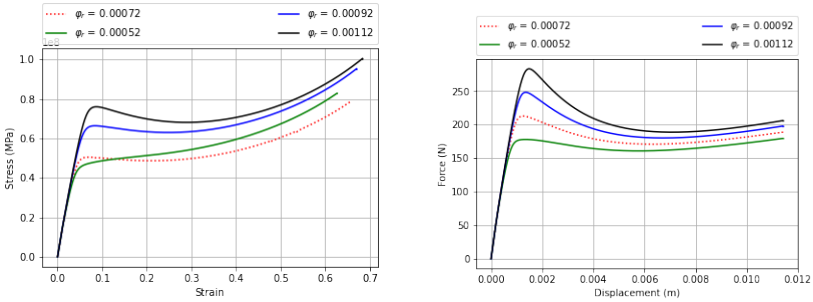

(a) (b)

Figure B.27: Variation of ϕ_r: (a) True stress-true strain behaviour (b) Force-displacement curves

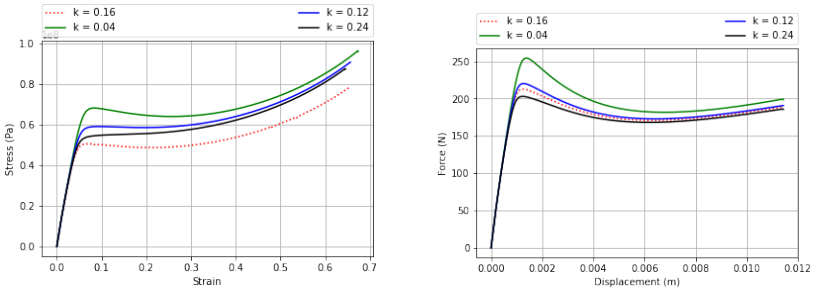

(a) (b)

Figure B.28: Variation of k: (a) True stress-true strain behaviour (b) Force-displacement curves

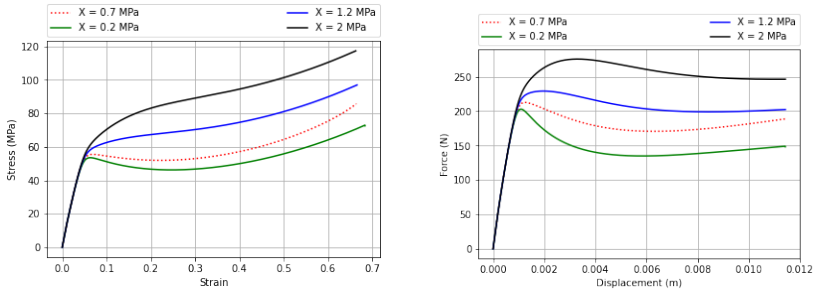

(a) (b)

Figure B.29: Variation of Back stress (X) : (a) True stress-true strain behaviour (b) Force-displacement curves